



Università degli studi ROMA TRE

PhD School of Engineering

Civil Engineering Section

XXIV Ciclo

Doctoral Thesis

**Multiscale analysis of masonry structures
using homogenization**

Student: Alberto Mauro

Tutors: Prof. Gianmarco de Felice

Prof. Paulo B. Lourenço

Ph.D. Coordinator: Prof. Leopoldo Franco

Rome, February 2012

The work reported in the present thesis was carried out at the Department of Structures of the University Roma Tre, Italy, and at the Civil Engineering Department of the University of Minho, Portugal, in accordance with the agreement for a joint research doctoral thesis signed by the two Institutions on 23 November 2009, Rep. N° 25, Prot. N° 37690.

Sommario

La valutazione della vulnerabilità sismica degli edifici in muratura secondo una prassi consolidata, affronta separatamente i meccanismi di collasso fuori dal piano delle pareti murarie ed il comportamento resistente dei setti murari rispetto alle azioni nel loro piano. I primi sono governati dalla dinamica dei corpi rigidi, i secondi dalla meccanica dei continui anisotropi non lineari.

In questa tesi si vuole fornire un contributo alla comprensione e alla modellazione di ambedue questi meccanismi resistenti.

Il comportamento fuori dal piano è affrontato nella prima parte della tesi (Capitolo 3) dove sono presentati i risultati di una campagna di prove su tavola vibrante condotta su una parete in muratura di tufo in scala reale, semplicemente accostata ai muri trasversali, e sollecitata fuori dal piano attraverso accelerogrammi naturali opportunamente selezionati e scalati. Le prove permettono di valutare la risposta dinamica della parete e le principali grandezze che ne influenzano il comportamento, gli effetti dovuti alla presenza dei giunti di malta e alle imperfezioni della struttura, la dipendenza dall'input, i meccanismi di dissipazione dell'energia. Successivamente viene presentata una strategia di modellazione basata sul metodo degli elementi distinti e validata attraverso il confronto con le prove sperimentali sia in termini di risposta massima sia in termini di storia temporale del moto. Infine, l'attendibilità delle procedure statiche equivalenti recentemente proposte dalle norme tecniche per la verifica sismica delle pareti rispetto ai meccanismi locali sono discusse in maniera critica sulla base dei risultati sperimentali e delle simulazioni numeriche effettuate.

La seconda parte della tesi (Capitoli 4 e 5) affronta la modellazione delle pareti sollecitate nel piano attraverso l'impiego della teoria dell'omogeneizzazione di mezzi periodici. In prima battuta viene formulata una procedura per l'identificazione in campo elastico della muratura come continuo di Cauchy. Tale procedura consente di ricavare delle formulazioni analitiche che esprimono le costanti elastiche della muratura in funzione delle proprietà geometriche e meccaniche delle componenti, tenendo conto sia dell'anisotropia indotta dalla tessitura muraria sia degli "effetti Poisson" derivanti dalla differente rigidezza della malta e del blocco. L'accuratezza di tali formulazioni è verificata attraverso un confronto con analisi ad elementi finiti e dati sperimentali di letteratura su un'ampia statistica di tessiture murarie regolari. Infine, il dominio limite elastico della muratura ottenuto attraverso la procedura

proposta è messo a confronto con i dati sperimentali disponibili in letteratura sia in termini di resistenza del materiale sia in termini di modalità di collasso.

Successivamente viene trattata l'estensione al campo non lineare della teoria dell'omogeneizzazione nel contesto più generale degli approcci multi-scala. Il problema viene formulato con riferimento ad un modello micro meccanico semplice in cui l'apparecchio murario è schematizzato come un insieme di blocchi elastici connessi da interfacce a comportamento elastoplastico secondo un criterio alla Mohr-Coulomb con flusso non associato. Attraverso l'ipotesi di moto affine dei blocchi, il problema viene definito rigorosamente nell'ambito della teoria dell'omogeneizzazione in funzione di un numero ridotto di parametri e risolto efficacemente a livello locale attraverso uno schema iterativo alla Newton-Raphson. L'algoritmo multi-scala è quindi implementato nel codice agli elementi finiti Abaqus e impiegato per lo studio del comportamento di pannelli murari caricati nel piano. I risultati ottenuti sono convalidati attraverso un confronto con modelli analitici basati sulla teoria dell'analisi limite e con prove di letteratura condotte su pareti in muratura a secco. Vengono quindi analizzati in maniera critica i limiti e le potenzialità del metodo proposto attraverso l'applicazione ad alcuni casi di studio reali.

Parole chiave: *Pareti in muratura, Meccanismi di collasso fuori dal piano, Prove tavola vibrante, Metodo degli Elementi Distinti, Meccanismi di collasso nel piano, Teoria dell'Omogeneizzazione, Approcci Multi-scala*

Resumo

Na avaliação da vulnerabilidade sísmica de edifícios de alvenaria é prática habitual abordar separadamente os mecanismos de colapso fora do plano e no plano das paredes estruturais. No primeiro caso, o mecanismo é descrito pela dinâmica dos corpos rígidos, enquanto que no segundo, é a mecânica dos meios contínuos anisotrópicos que rege o fenómeno.

A presente tese pretende fornecer um contributo para a compreensão e a modelação de ambos os mecanismos de colapso.

O comportamento das paredes de alvenaria solicitadas fora do plano é abordado na primeira parte da tese (Capítulo 3), onde se apresentam os resultados de um conjunto de ensaios realizados em plataforma sísmica em paredes de alvenaria de tufo, dispostas em forma de U, i.e., fachada adjacente às paredes transversais, tendo-se adoptado acelerogramas naturais adequadamente escalados para analisar o comportamento sísmico da fachada. Os ensaios permitem destacar os principais factores que influenciam o comportamento dinâmico da parede, os efeitos resultantes da presença de juntas de argamassa e de imperfeições da estrutura, a dependência dos parâmetros de *input* e os mecanismos de dissipação de energia. É apresentada uma estratégia de modelação baseada no Método dos Elementos Discretos que reproduz o comportamento experimental da estrutura em termos de rotação máxima e de história temporal do movimento. Finalmente, os resultados dos ensaios experimentais e das simulações efectuadas são comparados com o disposto nas normas Italianas de verificação sísmica.

A segunda parte da tese (Capítulos 4 e 5) é dedicada à modelação das paredes de alvenaria solicitadas no plano através da teoria da homogeneização aplicada a meios periódicos. No âmbito da teoria de homogeneização, desenvolve-se um modelo para a alvenaria como contínuo de Cauchy, de onde resultam expressões analíticas para as constantes elásticas, tendo em consideração os efeitos de Poisson devidos à diferença de rigidez entre o bloco e a argamassa e a anisotropia resultante da disposição dos blocos. Os resultados são validados para um amplo domínio das propriedades geométricas e mecânicas dos constituintes através de uma análise por elementos finitos e de resultados experimentais. Finalmente é obtido um limite para o domínio elástico, que é comparado com os resultados de ensaios experimentais disponíveis na literatura, em termos de resistência macroscópica e correspondente modo de colapso.

A extensão ao domínio não linear das técnicas de homogeneização é então abordada no contexto geral de métodos multi-escala. O problema é formulado através de um modelo micromecânico simples no qual a alvenaria é esquematizada como um sistema de blocos elásticos ligados através de interfaces não lineares, obedecendo ao critério de Mohr-Coulomb com escoamento não associado. Na hipótese de movimento simplificado entre blocos, o problema de homogeneização não linear fica definido em função de um número reduzido de incógnitas e é resolvido localmente através de um esquema iterativo Newton-Raphson. O método multi-escala é implementado no código de elementos finitos ABAQUS e adoptado no estudo do comportamento de painéis de alvenaria solicitados no plano. A aplicabilidade da metodologia proposta a problemas práticos de engenharia é analisada e discutida através da aplicação a casos de estudo reais.

Palavras-chave: *Paredes de alvenaria, Mecanismos de colapso fora do plano, Ensaio em plataforma sísmica, Método dos Elementos Discretos, Mecanismos de colapso no plano, Teoria de homogeneização, Métodos multi-escala*

Abstract

It is common practice when performing seismic vulnerability assessment of masonry buildings to tackle separately out-of-plane and in-plane failure mechanisms developed by load-bearing walls. The former are governed by the dynamics of rigid bodies while the latter is governed by the mechanics of anisotropic continuum media.

The present thesis intends to give a contribution to the understanding and modelling of both these failure mechanisms.

The behaviour of masonry walls under out-of-plane loads is addressed in the first part of the work (Chapter 3), where the results of a shake-table laboratory campaign on a tuff masonry U-shaped assemblage (façade adjacent to transverse walls) are presented. Scaled natural accelerograms have been adopted in order to analyse the seismic behaviour of the façade. The tests highlight the main factors affecting the dynamic behaviour of the wall, the effects related to the presence of mortar joints and of imperfections, the dependency of the response on the input and the mechanisms of energy dissipation. A modelling strategy based on the Discrete Element Method is then presented, which is shown to reproduce the experimental behaviour of the wall in terms of maximum rotation and time-history response. Finally, test results and numerical time-history simulations are compared to the Italian seismic code assessment procedures.

The second part of the thesis (Chapter 4 and 5) deals with modelling in-plane loaded masonry walls by resorting to the homogenization theory for periodic media. First, a Cauchy identification for masonry is developed within the framework of the homogenization theory, which provides analytical expressions for the elastic constants and take into account Poisson effects deriving from the mismatch of brick/joint stiffness and anisotropy deriving from brick interlocking. The results are validated with finite element analyses and experimental data over a wide range of geometrical and mechanical properties of the constituents. Finally, a homogenized limit elastic domain is derived and compared with the experimental tests available in literature, in terms of macroscopic strength and corresponding failure mode.

The extension to the non-linear range of homogenization techniques is then addressed within the framework of multi-scale methods. The problem is formulated by referring to a simple micro-mechanical model where masonry is

tackled as a system of elastic blocks connected by non-linear interfaces obeying to a Mohr-Coulomb criterion with non associative flow-rule. By introducing affine kinematics within the blocks, the non-linear homogenization problem is expressed in terms of few unknowns and is solved locally by means of an iterative Newton-Raphson scheme. The multi-scale procedure is implemented in the finite element code Abaqus and adopted for studying the in-plane behaviour of masonry panels. Finally, the main limits and the applicability of the proposed methodology to practical engineering problems are discussed by means of an application to real case studies.

Keywords: *Masonry walls, Out-of-plane failure mechanisms, Shake Table tests, Distinct Element Method, In-plane failure mechanisms, Homogenization theory, Multi-scale approaches*

Contents

LIST OF FIGURES.....	XII
LIST OF TABLES.....	XX
LIST OF SYMBOLS.....	XXII
1. INTRODUCTION.....	1
2. STATE OF THE ART.....	4
AN OVERVIEW ON THE EXPERIMENTAL CHARACTERIZATION OF MASONRY	4
<i>Mechanical behaviour of mortar and brick</i>	5
<i>Mechanical behaviour of in-plane loaded masonry</i>	6
<i>Mechanical behaviour of out-of-plane loaded masonry</i>	10
STRATEGIES FOR MODELLING MASONRY UNDER IN-PLANE LOADS.....	12
<i>Micro-modelling</i>	12
<i>Macro-modelling.....</i>	14
<i>Multi-scale approaches</i>	16
STRATEGIES FOR MODELLING MASONRY UNDER OUT-OF-PLANE LOADS	23
3. OUT-OF-PLANE LOADED MASONRY WALLS: EXPERIMENTAL TESTS AND DISTINCT ELEMENT MODELLING.....	29
TEST SUMMARY.....	31
<i>Selection of the records</i>	33
<i>Experimental results.....</i>	34
DYNAMIC MODELLING OF A MASONRY WALL ROCKING ON AN INCLINED FOUNDATION.....	38
COMPARISON BETWEEN EXPERIMENTAL AND NUMERICAL RESULTS	44
COMPARISON WITH CODE ASSESSMENT PROCEDURES	44
4. A HOMOGENIZATION APPROACH FOR THE IN-PLANE ANALYSIS OF MASONRY IN THE LINEAR ELASTIC RANGE....	50
FORMULATION OF THE LOCALIZATION PROBLEM.....	52
A SIMPLIFIED KINEMATICS FOR THE REPRESENTATIVE VOLUME ELEMENT ..	56
FROM TENSOR TO VOIGT NOTATION	61
A CLOSED FORM SOLUTION FOR THE LOCALIZATION PROBLEM.....	64
DISCUSSION AND VALIDATION OF THE RESULTS	67

	<i>Parametrical analysis</i>	68
	<i>Comparison with closed-form solutions given in the literature</i>	70
	<i>Comparison with finite element analysis</i>	74
	<i>Comparison with experimental data</i>	79
	ESTIMATE OF THE HOMOGENIZED LIMIT ELASTIC DOMAIN	81
	<i>Statement of the problem</i>	81
	<i>Description of the failure modes</i>	83
	<i>Comparison with experimental tests from literature</i>	85
5.	A MULTI-SCALE APPROACH FOR THE ANALYSIS OF MASONRY IN THE NON LINEAR RANGE.	88
	FORMULATION OF THE LOCALIZATION PROBLEM FOR THE ELASTO-PLASTIC INTERFACE MODEL	90
	A SIMPLIFIED KINEMATICS FOR THE REPRESENTATIVE VOLUME ELEMENT ..	94
	FROM TENSOR TO VOIGT NOTATION	96
	MULTI-SCALE ALGORITHM	98
	DERIVATION OF THE ELASTO-PLASTIC TANGENT MODULI	100
	DISCUSSION AND VALIDATION OF THE RESULTS	102
	<i>Response of the RVE under macroscopic loading conditions</i>	108
	NUMERICAL SIMULATIONS AND APPLICATIONS	113
	<i>Wall under vertical compression and horizontal traction</i>	113
	<i>Wall under gravity load and uniform horizontal acceleration</i>	118
	<i>Response of masonry arches under non uniform ground settlements</i>	127
6.	CONCLUSIONS	133
7.	REFERENCES.....	137

List of figures

Figure 2.1 Stress-strain curves of mortar (EM), brick (EB) and masonry (MU6H) specimens, Binda <i>et al.</i> 1996a-b.	7
Figure 2.2 Strength envelop of masonry derived by Page (1981,1983) for different angles (θ) between the in-plane load (σ_1 , σ_2) with respect to bed joint orientation: tension compression regime (a) and biaxial compression regime (b).	9
Figure 2.3 Shear peak strength of masonry joints as a function of the compressive stress applied, Van Der Pluijm (1993).	10
Figure 2.4 Examples of refined (a), Anthoine (1997) and simplified (b), Lourenço (1997a) micromodelling.	13
Figure 2.5 Empirical strength criteria proposed by Dhanasekar <i>et al.</i> (1985). ...	15
Figure 2.6 Combined strength criterion adopted for modelling in plane loaded masonry, Lourenço <i>et al.</i> (1998).	15
Figure 2.7 Strength domain of brick masonry as an homogenized material in space of macroscopic stresses, De Buhan and de Felice (1997).	18
Figure 2.8 Housner (1963) inverted pendulum.	23
Figure 2.9 Enrichments of Housner's model: (a) block resting on inclined foundation, Plaut <i>et al.</i> (1996), and (b) block constrained on one-side by transversal walls, and Sorrentino <i>et al.</i> (2008).	24
Figure 2.10 Three linear relation between the resorting force and the out-of-plane displacement of the block proposed by Doherty <i>et al.</i> (2002) and Sorrentino <i>et al.</i> (2008).	25
Figure 2.11 Model proposed by (a) Phycaris and Jennings (1984) and (b) Capecchi <i>et al.</i> (1996).	25
Figure 2.12 Rubble masonry walls out-of-plane loaded analyzed by means of the distinct element method, de Felice (2011).	26
Figure 2.13 Mechanisms analyzed by de Felice and Giannini (2001) by accounting for façade-transversal wall bond.	27

Figure 2.14 Out-of-plane limit analysis of masonry walls based on homogenization technique, Milani <i>et al.</i> (2006).	28
Figure 3.1. L'Aquila (Central Italy), after the April 6, 2009 earthquake. a) Church of San Pietro di Coppito; b) Oratory of San Giuseppe dei Minimi.	29
Figure 3.2 Test setup: each marker corresponds to an accelerometer and a displacement wire-transducer. All measurements are in meters.	31
Figure 3.3 View of the specimen with the anchor devices and the retaining structure: UPN 100 steel channel (dotted line) and steel heels (solid line)	32
Figure 3.4 Response spectra of signals imposed to the shake table and of accelerograms measured on the specimen's foundation.	34
Figure 3.5 Time histories recorded during tests 16, 27. (a) Relative displacement δu measured between wire transducers vertically aligned T6-T1 and T3-T1; b) Relative displacement measured between wire transducers horizontally aligned T6-T7 and T8-T7; c) Acceleration measured on the foundation by accelerometer A1. g = gravity acceleration.	36
Figure 3.6 Time histories recorded during tests 31 and 33. (a) Relative displacement δu measured between wire transducers T6-T1 and T3-T1; (b) Relative displacement measured between wire transducers T6-T7 and T8-T7; (c) Acceleration measured on concrete foundation by accelerometer A1. g = gravity acceleration.	37
Figure 3.7 View of the specimen at the beginning (a) and at the end (b) of test 34.	37
Figure 3.8 Distinct element model of masonry specimen. (a) Configuration before each test: initial out-of-plumb η and gap d related to mortar vertical joint. (b) Kinematic descriptors of the motion: out-of-plane rotation of the façade wall measured with respect to the vertical (θ) and to the tilted foundation (θ_r).	39
Figure 3.9 Normalized response curves in terms of restoring moment (M_R)-rotation (θ_r) relationships, varying: (a) number n of contacts, and (b) normal stiffness k_n . f_0 denotes the frequency of small amplitude rocking motion.	41
Figure 3.10 Comparison between experimental and numerical time histories. $d=4$ mm; $n=15$, $k_n=1.35$ GPa, $k_t=0.4 k_n$, $f_c=p/(2\pi)$	43

Figure 3.11 Parametric analysis with respect to the damping ratio (ξ) and the stiffness (k_n) of the bed joint: synthetic comparison between numerical and experimental time histories for test 27, in terms of RMS* and WME (Eqs.3.4 - 3.5).	43
Figure 3.12 Comparison between experimental and DEM numerical results in terms of normalized maximum rotation assuming $d = 4$ mm; $n = 15$, $k_n = 1.35$ GPa, $k_t = 0.4 k_n$, $f_c = p / (2 \pi)$	44
Figure 3.13 Rigid-block model adopted for evaluating the response according to code procedures, CSLPP (2009).	45
Figure 3.14 Comparison between experimental and code demand / capacity ratios. (a): strength-based, linear, and (b): displacement-based, nonlinear, code procedures, CSLPP (2009).	46
Figure 3.15 Comparison between non linear dynamic and code (CSLLPP 2009) demand / capacity ratios. (a): strength-based, and (b): displacement-based code procedures adopting the DEM model. Empty (solid) marker is referred to Negative (Positive) polarity; coloured (grayscale) marker is referred to natural (artificial) accelerograms.	48
Figure 3.16 Behaviour factor q versus the percentage of conservative cases evaluated by means of numerical analyses.	49
Figure 4.1 Domain of reference Ω (a) and corresponding representative volume element Ω_{RVE} (b).	52
Figure 4.2 Division of Ω_{RVE} in brick (Ω^i with $i=1,...,4$) and mortar (Ω^i with $i=5,...,11$) sub-domains, together with the respective centres g^i	54
Figure 4.3 Example of points p^i and p^j that correspond by periodicity, Eq. (4.18).	57
Figure 4.4 Example of points q^i and q^j that fulfil Eqs. (4.24)-(4.25).	59
Figure 4.5 Elastic moduli of masonry in horizontal (a) and vertical (b) directions versus the thickness of the joints t evaluated in plane stress (PS) and in generalised plane strain (GPS) conditions for different ratios of the Young moduli of brick and mortar, Y_b/Y_m	69

Figure 4.6 Shear modulus of masonry versus the thickness of the joints t evaluated in plane stress (PS) and in generalised plane strain (GPS) conditions for different ratios of the Young moduli of brick and mortar, Y_b/Y_m	69
Figure 4.7 Elastic moduli of masonry in horizontal (a) and vertical (b) directions versus the thickness of the joints t evaluated for different ratios of the Young moduli of brick and mortar Y_b/Y_m , referring to the generalized plain strain (GPS) condition, to the stratified model (SM) and to the cohesive interface model (IM).	72
Figure 4.8 Shear modulus of masonry versus the thickness of the joints t evaluated for different ratios of the Young moduli of brick and mortar Y_b/Y_m , referring to the generalized plain strain (GPS) condition, to the stratified model (SM) and to the cohesive interface model (IM).	73
Figure 4.9 Finite element mesh defined on one-eighth of the total volume of the RVE adopted for three-dimensional analysis (a); finite element mesh defined on a quarter of the total RVE adopted for plane stress analysis (b).	75
Figure 4.10 Error introduced by the proposed model in evaluating horizontal (a), vertical (b) , shear moduli (c) and Poisson coefficient (d) with respect to three-dimensional finite element analyses performed for different ratios between the height of the brick h_b and the thickness of the joints t , varying the ratio between the Young moduli of brick and mortar, Y_b/Y_m	76
Figure 4.11 Error introduced by the proposed model in evaluating horizontal (a), vertical (b) , shear moduli (c) and Poisson coefficient (d) with respect to plane stress finite element analyses performed for different ratios between the height of the brick h_b	77
Figure 4.12 Comparison between three dimensional finite element analysis and the simplified homogenization procedure proposed: component σ_{11} of the microscopic stress field for running bond masonry under uniaxial macroscopic compression $\Sigma_{22}=-1$ MPa.....	78
Figure 4.13 Comparison between the phase-averaged stresses evaluated from finite element analyses and the ones predicted by the model for a unitary macroscopic vertical stress Σ_{22}	79

Figure 4.14 Comparison between the elastic modulus in the vertical direction measured on masonry samples, $Y_{22,measured}$, and the respective modulus predicted by the proposed procedure, $Y_{22,predicted}$, referring to mortar and unit properties measured separately.	80
Figure 4.15 Limit elastic domain of masonry with iso-shear stress lines plotted in the space of the macroscopic stress Σ_{11} - Σ_{22} - Σ_{12} considering the head joint filled (a) and unfilled (b) together with abacus of the failure modes (c).	84
Figure 4.16 Homogenized limit elastic domain evaluated in plane stress (PS) and generalized plane strain (GPS) conditions versus the experimental data from Page (1981,1983). Angles between principal stresses Σ_{11} - Σ_{22} and bed joint orientations 0° (a), 22.5° (b) and 45° (c).	87
Figure 5.1 Geometrical transformation introduced at the microscopic level: (a) model of joints treated as continuum element and (b) model of joints treated as interfaces.	90
Figure 5.2 Identification of the sub-domains pertaining to the RVE adopted in the present work.	91
Figure 5.3 Jump of displacement (w^{ij}) and traction (σ^{ij}) acting on the interface.	92
Figure 5.4 Limit elastic domain of masonry in the macroscopic state of stress.	105
Figure 5.5 Comparison between the yield surface (thin line) by De Buahn and de Felice (1996) and the elastic limit surface (thick line) evaluated for $\xi = 0$ (a) and $\xi = +\infty$ (b).	107
Figure 5.6 Masonry under pure horizontal traction: comparison between the stress-strain relations and the ratios between horizontal and vertical strains obtained for $\psi=0.6$ and $\psi=0.0$	108
Figure 5.7 Masonry under pure horizontal traction: comparison between the deformed shapes of the RVE obtained for $\psi=0.6$ (a) and $\psi=0.0$ (b).	109
Figure 5.8 Masonry under pure horizontal traction: Comparison between the force acting within the unit and mortar joints, the curves are independent on the dilatancy assumed.	109

Figure 5.9 Masonry under pure shear: comparison between the stress-strain relations and the ratios between horizontal and vertical strains obtained for $\psi=0.6$ and $\psi=0.0$	110
Figure 5.10 Masonry under pure shear: comparison between the deformed shapes of the RVE obtained for $\psi=0.6$ (a) and $\psi=0.0$ (b).	110
Figure 5.11 Masonry under horizontal traction combined with shear: comparison between the stress strain curves obtained for $\psi=0.6$ and $\psi=0.0$. The markers delimit the phases of masonry behaviour.	111
Figure 5.12 Masonry under horizontal traction combined with shear: comparison between the deformed shapes of the RVE obtained for $\psi=0.6$ (a) and $\psi=0.0$ (b).	112
Figure 5.13 Masonry under shear combined with horizontal traction: Comparison between the stress-strain history recorded on the joints for $\psi=0.6$ and $\psi=0.0$	112
Figure 5.14 Masonry under shear combined with horizontal traction: Comparison between the equilibrium paths followed by the components and plotted in the space of microscopic stress together with the Mohr Coulomb yield surface.	113
Figure 5.15 Masonry wall subjected to gravity load, vertical pressure q and horizontal displacement u imposed at the later sides.	114
Figure 5.16 Stress state experienced by the unit located in correspondence of the course i of the wall.	114
Figure 5.17 Masonry wall under vertical load and horizontal traction: finite element mesh.	116
Figure 5.18 Comparison between the force-displacement curve obtained by the proposed approach and the analytical solution obtained by applying the yield design method.	117
Figure 5.19 Normal plastic jump of displacement of the head interface w_n^{13} (in <i>cm</i>) for a displacement imposed at the lateral edge of the wall equal to 2 cm.	117
Figure 5.20 Masonry textures investigated by Ceradini (1992).	118

Figure 5.21 Masonry walls under uniform vertical and horizontal accelerations:(a) view of the walls,(b) system of application of the load adopted by Ceradini (1992).	119
Figure 5.22 Rigid block failure mechanism assumed by De Buhan and de Felice (1997) for the homogenized wall undergoing uniform vertical and horizontal accelerations.	119
Figure 5.23 Horizontal load multiplier versus the displacement measured at the top of the wall ($H/L = 0.5$).	121
Figure 5.24 Wall having $H/L = 0.5$: Comparison between experimental test (a) and numerical outputs in terms of the deformed shape at collapse (b) and plastic slips of bed interfaces w_t^{23} (c), expressed in m	122
Figure 5.25 Horizontal load multiplier versus the displacement measure at the top of the wall ($H/L = 1.0$).	123
Figure 5.26 Collapse mechanisms of the wall having $H/L=1$ and amplified deformed mesh obtained by applying the multi-scale approach proposed.	123
Figure 5.27 Contour plot of (a) the plastic slip w_t^{23} developed within the bed interface, expressed in m ($H/L=1$).	124
Figure 5.28 Horizontal load multiplier versus the displacement measure at the top of the wall ($H/L = 2.0$).	124
Figure 5.29 Contour plot of (a) the plastic slip w_t^{23} and (b) normal displacement w_n^{23} of bed interfaces, expressed in m , and amplified deformed shape at collapse (c), ($H/L=2$).	125
Figure 5.30 Comparison between the horizontal load multiplier evaluated by mean of the analytical solution by De Buhan and de Felice (1997) and by finite element analyses against the experimental tests by Ceradini (1992).	126
Figure 5.31 View of the Felice aqueduct in the area of Lodi square. Low span arches are the original ones built with tuff masonry in XVI century while large span arches were built in 1930 with solid brick masonry, Sebastianelli (2011).	127
Figure 5.32 Details of brick (a) and tuff (b) masonry arches belonging to the Felice aqueduct, Sebastianelli (2011).	128

Figure 5.33 Finite element meshes adopted for modelling the arches of the Felice aqueduct: (a) low span arches, (b) large span arches.	129
Figure 5.34 Contour plot of (a) the plastic normal displacement w_n^{23} , (b) the plastic slip w_t^{23} developed within the bed interfaces, expressed in m , and (c) the deformed mesh of low span arches. The plastic displacements experienced by bed joint 12 prove specular to the one here reported.	130
Figure 5.35 Contour plot of (a) the plastic normal displacement w_n^{23} and (b) the plastic slip w_t^{23} developed within the bed interfaces, expressed in m , together with (c) the deformed mesh of large span arches. The plastic displacements experienced by bed joint 12 prove specular to the one here reported.	131
Figure 5.36 Comparison between the maximum jump of displacement recorded in the models versus the imposed settlement deflection, $\delta/2L$	132

List of tables

Table 3.1 Italian accelerograms selected to perform shake table tests. Data have been collected from SISMA database [http://151.100.4.92/].....	32
Table 3.2. Sequence of tests performed: main properties of the accelerogram recorded at the base of the wall and summary of the results. SF = Scale factor in terms of PGA with respect to the original earthquake (Table 3.1), I_A = Arias Intensity, VSI = Velocity Spectrum Intensity within the range of periods (0-4) s, MIV = Maximum Incremental Velocity, η = initial out-of-plumb recorded, θ = maximum values recorded for the rotation, α = internal angle of the wall (Figure 3.1), f = predominant frequency of the wall's free vibrations measured at the end of the test.....	34
Table 4.1 Geometrical and mechanical properties of the phases adopted in defining the limit elastic domain of masonry reported in Figure 4.15.....	82
Table 4.2 Properties of masonry constituents adopted for reproducing the experimental data from Page (1985).	85
Table 4.3 Comparison between the elastic constants measured on masonry panel Danasekar <i>et al.</i> (1982) and the elastic constants predicted introducing in the proposed model the properties of the constituents reported in Table 4.2....	85
Table 5.1 Geometrical and mechanical properties of the phases adopted in the numerical simulation.....	116
Table 5.2 Geometrical and mechanical properties of the masonries belonging to the Felice aqueduct.....	129

List of symbols

The following quantities have been introduced within the thesis:

- Scalars

$$x_i, H_{ij}, B_{ijk}, C_{ijkl} \in \mathbb{R}$$

- Vectors

$$\mathbf{x} \in \mathbb{R}^3 \quad \mathbf{x} = \sum_i x_i \mathbf{e}_i$$

- Second order tensors

$$\mathbf{H} \in \mathbb{R}^3 \otimes \mathbb{R}^3 \quad \mathbf{H} = \sum_{ij} H_{ij} \mathbf{e}_i \otimes \mathbf{e}_j$$

- Third order tensors

$$\mathbf{B} \in \mathbb{R}^3 \otimes \mathbb{R}^3 \otimes \mathbb{R}^3 \quad \mathbf{B} = \sum_{ijk} B_{ijk} \mathbf{e}_i \otimes \mathbf{e}_j \otimes \mathbf{e}_k$$

- Fourth order tensors

$$\mathbf{A}, \mathbf{C} \in \mathbb{R}^3 \otimes \mathbb{R}^3 \otimes \mathbb{R}^3 \otimes \mathbb{R}^3 \quad \mathbf{C} = \sum_{ijkl} C_{ijkl} \mathbf{e}_i \otimes \mathbf{e}_j \otimes \mathbf{e}_k \otimes \mathbf{e}_l$$
$$\mathbf{A} = \sum_{ijkl} A_{ijkl} \mathbf{e}_i \otimes \mathbf{e}_j \otimes \mathbf{e}_k \otimes \mathbf{e}_l$$

where indexes i, j, k, l vary from 1 to 3 and $\mathbf{e}_1, \mathbf{e}_2, \mathbf{e}_3$ constitute an orthonormal basis of the three dimensional Euclidean space, \mathbb{R}^3 . The simple contraction and the double contraction operators, which are well established in literature, are denoted as reported below.

- Simple contraction operator:

$$\mathbf{x} \cdot \mathbf{x} = \sum_i x_i x_i$$

$$\mathbf{H} \cdot \mathbf{x} = \sum_{ij} H_{ij} x_j \mathbf{e}_i$$

$$\mathbf{B} \cdot \mathbf{x} = \sum_{ijk} B_{ijk} x_k \mathbf{e}_i \otimes \mathbf{e}_j$$

- Double contraction operator:

$$\mathbf{H} : \mathbf{H} = \sum_{ij} H_{ij} H_{ij}$$

$$\mathbf{C} : \mathbf{H} = \sum_{ijkl} C_{ijkl} H_{kl} \mathbf{e}_i \otimes \mathbf{e}_j$$

$$\mathbf{H} : \mathbf{C} = \sum_{ijkl} H_{ij} C_{ijkl} \mathbf{e}_k \otimes \mathbf{e}_l$$

$$\mathbf{A} : \mathbf{C} = \sum_{ijklpq} A_{ijkl} C_{klpq} \mathbf{e}_i \otimes \mathbf{e}_j \otimes \mathbf{e}_p \otimes \mathbf{e}_q$$

where indexes i, j, k, l, p, q vary from 1 to 3. The main latin symbols used in the thesis are reported below:

a	<i>Height of the unit</i>
A^i / A_i	<i>Fourth order tensor/Second order tensor relating H^i to H</i>
b	<i>Length of the unit</i>
B^i	<i>Third order tensor representing the quadratic part of the displacement fields within cross joints ($i=10,11$)</i>
C^{hom}	<i>Second order elasticity tensors of masonry as an homogeneous material</i>
$C^b, C^m, C^h / C^b, C^m, C^h$	<i>Fourth order tensor/Second order elasticity tensors of brick, mortar bed and head joints</i>
D^i	<i>Second order tensor of strain localization defined on Ω^i ($i=1,...,11$)</i>
$\mathbf{e}_1, \mathbf{e}_2, \mathbf{e}_3$	<i>Orthonormal vector constituting the basis of three dimensional Euclidean space</i>

g^i	<i>Centre of sub-domain Ω^i ($i=1,..,11$)</i>
h_b	<i>Height of the brick</i>
H^i	<i>Second order tensor/Vector representing the linear part of the displacement fields within sub-domain Ω^i ($i=1,..,11$)</i>
H	<i>Second order tensor/Vector representing the linear part of the displacement fields within the brick sub-domain</i>
H^1	<i>Sobolev space over Ω_{RVE}</i>
K_n, K_t	<i>Normal and tangential stiffness of mortar joints when treated as interfaces</i>
i_1, i_2	<i>Directions of periodicity of the RVE</i>
l_b	<i>Length of the brick</i>
m	<i>Geometrical aspect ratio of the unit equal to $2a/b$</i>
M_s	<i>Tensor relating the gradient of displacement H^i to the respective deformation ϵ^i</i>
n	<i>Unitary normal vector of a generic surface</i>
S^i	<i>Second order tensor of stress localization on the sub-domain Ω^i ($i=1,..,11$)</i>
t	<i>Unitary tangential vector of a generic surface</i>
t_h	<i>Thickness of mortar head joint</i>
t_m	<i>Thickness of mortar bed joint</i>
T	<i>Thickness of the domain of reference in the direction e_3</i>
$u(x)$	<i>Displacement field over Ω_{RVE}</i>

$\hat{u}(\mathbf{x})$	<i>Fluctuating part of the displacement field over Ω_{RVE}</i>
$w^{ij}(\mathbf{x})$	<i>Jump of displacement across the interface $\partial\Omega^i \cap \partial\Omega^j$</i>
\mathbf{V}_{per}	<i>Space of periodic and fluctuating displacement fields over Ω_{RVE}</i>
Y_m, Y_m, Y^{hom}	<i>Young Modulus of mortar, brick and of the homogeneous material</i>

The main greek symbols used in the thesis are reported below:

δ	<i>Ground settlement</i>
$\varepsilon(\mathbf{x})$	<i>Microscopic strain field</i>
ε^i	<i>Strain displayed by sub-domain Ω^i ($i=1,...,11$)</i>
E	<i>Macroscopic strain</i>
γ^i	<i>Engineering shear strain displayed by sub-domain Ω^i ($i=1,...,11$)</i>
λ	<i>Collapse load multiplier</i>
λ^i	<i>First Lamé's constant of the material pertaining to sub-domain Ω^i ($i=1,...,11$)</i>
μ	<i>Coefficient of friction of the interface</i>
μ^i	<i>Second Lamé's constant, or Shear modulus, of the material pertaining to sub-domain Ω^i ($i=1,...,11$)</i>
ν^i	<i>Poisson's coefficient of the material pertaining to sub-domain Ω^i ($i=1,...,11$)</i>
$\sigma(\mathbf{x})$	<i>Microscopic stress field</i>

σ^i	<i>Stress acting within sub-domain Ω^i ($i=1,...,11$)</i>
$\sigma^{ij}(\mathbf{x})$	<i>Traction acting on the interface $\partial\Omega^i \cap \partial\Omega^j$</i>
Σ	<i>Macroscopic stress</i>
τ^i	<i>Microscopic shear stress acting within sub-domain Ω^i ($i=1,...,11$)</i>
Ω	<i>Domain of reference at the macroscopic scale</i>
Ω^i	<i>Generic Sub-domain pertaining to the Representative Volume Element</i>
Ω_{RVE}	<i>Representative Volume Element</i>
ψ	<i>Coefficient of dilatancy</i>

Other symbols:

$$\langle \bullet \rangle = \frac{1}{\Omega_{RVE}} \int_{\Omega_{RVE}} \bullet \, d\Omega \quad \text{Averaging operator for continuous fields}$$

$$\langle \bullet^i \rangle = \frac{1}{\Omega_{RVE}} \sum_i \bullet^i \Omega^i \quad \text{Averaging operator for piece-wise constant fields over } \Omega_{RVE}$$

1. Introduction

Typically, masonry is a composite material consisting of an assembly of units bonded with relatively thin mortar joints, which has been widely used over the past centuries as a building material. This means that the majority of building stock even in developed countries is made of masonry. Its use nowadays has been reduced due to the advent of new materials, but masonry may still constitute a valid economic and performance-based alternative to concrete and steel, for selected applications. Understanding the structural behaviour of masonry is thus a topic of great interest within the technical community, for the assessment of existing buildings and a more accurate design of new ones, and received a great attention in the last twenty years.

It is well established that the mechanisms developed by unreinforced masonry structures to withstand a combination of vertical and horizontal loads may be subdivided in two categories namely, in-plane and out-of-plane mechanisms. In real cases it is unlikely that load-bearing walls undergo only one of them since a combination of in-plane and out-of-plane actions actually takes place. Nevertheless, it is common practice to analyze these mechanisms separately assuming that failure is mainly driven by one of them. This assumption, which allows a simplification of the problem, derives somehow from the inherent difficulties of analyzing the complete three-dimensional behaviour of masonry walls. Moreover, when dealing with regular masonry, the mechanical phenomena governing the response under in-plane actions prove different from those governing the response out-of-plane. As a matter of fact, in-plane mechanisms are mostly related to the local strength of masonry assemblage and are usually characterized by small amplitude displacements. Conversely, out-of-plane mechanisms exhibit large displacement and, therefore, are strongly affected by second order effects while the influence of the local material strength proves negligible. These considerations hold true provided that the behaviour of the material in the out-of-plane direction may be regarded to as monolithic and disaggregation is unlikely to occur, which is reasonable for regular masonry walls.

In agreement with this methodology, in the present thesis in-plane and out-of-plane mechanisms of regular masonry walls are tackled separately.

Concerning the out-of-plane mechanisms, many experimental campaigns have been conducted in the last 20 years. Nevertheless, all these investigations have been performed on artificial brick or block masonry or on single-block stone elements. So far, no forced vibration tests have been performed on natural stone masonry, which is more frequent in existing masonry buildings, especially

in the Mediterranean area. Additionally, no such tests have considered a panel laterally restrained on one side by transverse walls, which is the rule more than the exception in masonry buildings. On the modelling side, some approaches have been developed in the literature which account for this aspect. Nevertheless, owing to the lack of experimental tests, their reliability and accuracy still need to be investigated.

The first part of the thesis intends to give a contribution in this direction. The results of a shake-table laboratory campaign on a tuff masonry U-shaped assemblage (façade adjacent to transverse walls) are presented. The tests, excited by scaled natural accelerograms, replicate the behaviour of external walls in existing masonry buildings undergoing out-of-plane rocking motion. A modelling approach based on the Discrete Element Method is then presented and its capability of reproducing the experimental tests investigated. Finally, experimental results and numerical time-history simulations are compared to the Italian seismic code assessment procedures.

In-plane mechanisms of masonry walls have been studied by means of several experimental campaigns which, starting from 1950, investigated a wide variety of masonry typologies. Accordingly, the phenomena governing such mechanisms are well established in the literature. Therefore, in the last years the technical community focused on the development of modelling strategies for reproducing the essential feature of masonry behaviour while able to perform structural analysis with acceptable computational costs. Among the different approaches proposed, the ones based on the multi-scale methods and on the homogenization technique proves particularly attractive. Within this ambit, the methodology proposed so far proves too complex and their feasibility for the analysis of real size structures still needs to be investigated. Therefore, there is a gap between the procedure available in the literature and the actual need for a tool able to provide, with relative low computational effort, valuable information for common engineering problems. The second part of the thesis intends to give a contribution in order to partially reduce this gap by providing simplified homogenization procedures for the analysis of in-plane loaded masonry structures both in the elastic and non-linear range.

In the linear elastic range a constitutive identification of the material is developed, which takes into account both Poisson effects deriving from the mismatch of brick/joint stiffness and anisotropy deriving from brick interlocking. The proposed formulation, based on simplifying assumptions concerning the kinematics of brick and joint phases, provides analytical expressions for the in-plane elastic constants of masonry seen as a Cauchy

homogeneous medium. The accuracy of the proposed scheme is investigated by means of a comparison with finite element analyses and experimental data. The homogenized limit elastic domain provided by the proposed approach is then compared with the experimental tests available in the literature.

In the non-linear range, a multi-scale procedure based on first-order homogenization is presented. Masonry is regarded as an assembly of elastic bricks separated by elasto-plastic interfaces obeying to a Mohr-Coulomb yield criterion with non-associative flow rule. In order to reduce the computational costs and to make the procedure suitable for the implementation into general purpose finite element programs, an affine kinematics is introduced over the representative volume element. Accordingly, the non linear homogenization problem is formulated in terms of a reduced number of unknowns and solved at the microscopic scale by means of a Newton-Raphson iterative scheme. The effectiveness of the proposed method is evaluated by performing numerical tests on the representative volume element undergoing different macroscopic stress conditions. The multi-scale procedure is implemented in the finite element code Abaqus and validated against experimental results on dry-stack masonry walls. Eventually, the proposed methodology is adopted for evaluating the response of masonry arches, belonging to the Felice aqueduct in Rome, under non uniform ground settlement.

2. State of the art

This chapter presents, in the first part, an overview on the mechanical characteristics of masonry wall derived by means of experimental tests. In the second part, a state of the art is reported, which deals with the different modelling strategies developed in the literature for simulating the behaviour of masonry structures under in-plane and out-of-plane actions.

An overview on the experimental characterization of masonry

Experimental investigations devoted to study the mechanical behaviour of masonry originated in Europe in the end of the XVIII century, when, with the advent of the industrial revolution, the modern society started to develop the need of optimizing the costs of building materials. Accordingly, structures became more and more slender and the level of mechanical stress sustained by load bearing elements remarkably increased. Additionally, the traditional methods and the rules-of-thumb, so far adopted for the design of masonry constructions, started to be replaced by newer procedures based on the theory of elasticity, according to which structural safety was related to the capability of the material to sustain the local stress produced by the external loads. These reasons drew the attention of the technical community on the determination of masonry strength through experimental tests.

The earliest experimental investigations are described in Cavalieri (1845) and date back to 1774 and 1818 when Gauthey and Rennie, respectively, performed the first compression tests on brick samples. Only in the middle of the XIX century masonry started to be seen as a composite material and test procedures, so far devoted to study only the behaviour of the strongest component, were extended to mortar samples. Curioni (1872) collected the results of experimental campaigns carried out on a wide variety of stones, bricks and mortars commonly adopted in Italy at that time. Only a few years later in Gabba and Caveglia (1876), Campanella (1926) and Donghi (1935), it is possible to find the earliest information concerning the compressive strength of masonry as a whole.

Since the advent of new construction materials, *i.e.* steel and reinforced concrete, the use of masonry remarkably reduced and, consequently, the attention of the technical community decreased. Starting from 1930 the investigation activity on brickwork was abandoned, with the exception of the United Kingdom and the United States where load bearing masonry structures were still very common. It is in the latter countries, around 1970, that the modern experimental activity on masonry developed with the purpose of defining reliable codes of practice and regulations for new constructions.

The pioneer work was by Hilsdorf (1968), followed by Francis *et al.* (1971), McNary and Abrams (1985), Schubert (1988) who investigated the compressive strength of masonry in direction perpendicular to the bed joints. In the following years the spread of numerical modelling gave the impulse for defining more sophisticated tests with the purpose of achieving a complete constitutive characterization of masonry. Therefore, experimental campaigns were conducted aiming at deriving the modulus of elasticity and the strength of masonry both under uni-axial compression, Plowman (1965), Lenczner (1978), Binda *et al.* (1988), and under multi-axial states of stress, Samarasinghe and Hendry (1980), Page (1981,1983), Dhanasekar *et al.* (1982). Thanks to the development of new testing apparatus designed for quasi-brittle material, in the last twenty years the technical community produced an increasing number of contributions investigating the complete stress-strain curve of masonry including either the post peak behaviour, Priestley and Elder (1983), Van der Pluijm (1993), Kaushik *et al.* (2007), Reyes *et al.* (2008), or loading-unloading cycles, Naraine and Sinha (1992), Oliveira *et al.* (2006).

In the meanwhile, increasing interest grew in Europe towards the preservation of the architectural heritage: either for assessment purpose or for defining strengthening techniques compatible with the existing materials, extensive laboratory and in situ tests were carried out for the mechanical characterization of ancient masonry, Binda *et al.* (1991, 2006), Valluzzi *et al.* (2002), De Felice and De Santis (2010).

Mechanical behaviour of mortar and brick

As a composite material, masonry exhibits a behaviour which strongly depends on the type of components adopted and the workmanship process. As a consequence, tests on masonry have always been accompanied by tests on mortar and brick/stone samples, since the beginning of the XIX century, Curioni (1872).

Most of the experimental investigations on masonry unit were carried out mainly on brick samples, being well-known, since the time of Cavalieri (1845), that crushing failure of the block is unlikely to occur in stonework. Nowadays, the mechanical characterization of the brick is made identifying strengths and elastic modules measured with respect to the bed and header faces by means of direct compressive tests, Rilem (1994). Tensile strength can be defined from different testing techniques, namely, flexural, splitting and direct tension tests, UNI 8942 (1986). As pointed out by experimental evidences, masonry brick usually shows a brittle response often accompanied by a marked orthotropic behaviour due to the manufacturing process and the volume of perforations, Van Der Pluijm (1992). Despite the fact that biaxial tests in the tension-compression regime have been performed by Khoo and Hendry (1973) and Atkinson *et al.* (1985), there is a lack of information regarding the complete strength envelop of masonry brick.

Mortar, in most cases, constitutes the weakest component of masonry assemblage. Standard compressive test, indirect tension and flexural tests are the most diffuse way to obtain a mechanical characterization of mortar samples. Experimental evidences outline a brittle behaviour characterized by a fracture energy which depends on the composition of the mixture adopted, Sahlin (1971). Khoo and Hendry (1973), Atkinson *et al.* (1985) and McNary and Abrams (1985) performed tri-axial compression tests showing that an increase of confining stress resulted in an increase in terms of material strength and ductility. The behaviour of mortar proved similar to the one of concrete, which has been widely investigate under multi-axial state of stress, Yurdas *et al.* (2004).

Mechanical behaviour of in-plane loaded masonry

Up to thirty years ago, the design of masonry structures was performed mainly with reference to vertical loads. So far, most of the interest of the scientific community was addressed to the determination of the compressive strength of masonry under uni-axial load normal to the bed joints. The experimental evidences show that brickwork behaviour is intermediate with respect to the behaviour of the constituents, and is characterized by a quasi-brittle failure, Figure 2.1. The curve deviates from the initial linear elastic branch when vertical cracks initiate in the brick. For increasing loads, the cracks propagate trough the entire brickwork involving the mortar joints. Once the compressive strength is reached the capacity of the material to sustain external load falls rapidly to zero.

Since the work of Hilsdorf (1968), the phenomena accompanying the failure of brickwork in compression are well recognized and are related to the different deformability of mortar and brick, being usually the former more deformable than the latter. Accordingly, when masonry is loaded in compression mortar joints above and below each brick tend to expand laterally more than the brick itself. Therefore, mortar undergoes tri-axial compression stresses while the latter undergoes vertical compression combined with lateral tension. This interaction between the components, also named Poisson effects, are responsible for the splitting cracks that develop in the brick and initiate failure of masonry in compression.

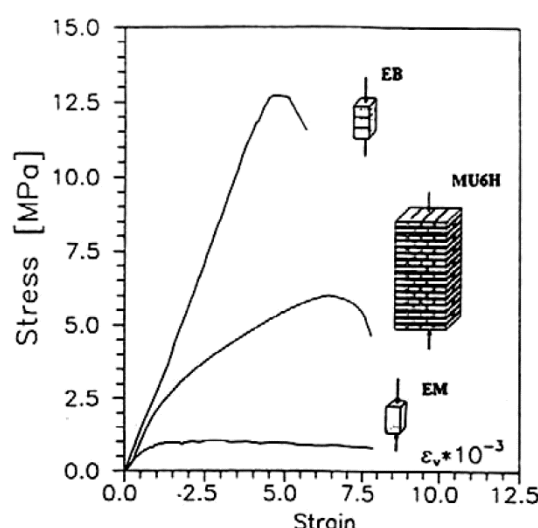


Figure 2.1 Stress-strain curves of mortar (EM), brick (EB) and masonry (MU6H) specimens, Binda *et al.* 1996a-b.

Many researches have followed, which investigated the main factors affecting the compressive strength of masonry such as thickness of mortar joint, type of brick and mortar: Francis *et al.* (1971), McNary and Abrams (1985), Schubert (1988), Plowman (1965), Lenczner (1978), Binda *et al.* (1988, 1996a-b), Oliveira *et al.* (2006), De Felice and De Santis (2010) among others.

In the following years, the behaviour of masonry under different combination of loads started to be investigated. The main purpose was to provide suitable design information for codes of practice to allow prediction of the capacity of walls acting either as a load bearing element or in conjunction with a reinforced concrete frame.

To this purpose, experimental tests were carried out on wall samples undergoing different combinations of vertical compression and shear acting along the middle plane of the panels. These loading conditions induce within the specimen non-uniform states of stress which aimed at representing the ones experienced by a masonry wall in a real structure when combinations of dead and live loads (wind or earthquake) are encountered. Several monotonic tests have been performed on a wide variety of walls built with different geometrical aspect ratios and masonry types. A comprehensive review of the experiments performed up to 1980 is reported in Page *et al.* (1982) and Mann and Muller (1982). Essentially three in-plane failure modes have been encountered:

1. Flexural/Rocking failure: as horizontal load increase, bed joints crack in tension, and shear is carried by the compressed masonry; final failure is obtained by crushing of the compressed corner or, for large displacement, for overturning of the wall.
2. Shear cracking: peak resistance is governed by the formation and development of inclined diagonal cracks, which may follow the path of bed- and head-joints or may go through the bricks, depending on the relative strength of mortar joints, brick-mortar interface, and bricks.
3. Sliding: due to the formation of tensile horizontal crack in the bed joints potential sliding planes can form along the cracked bed joints; this failure mode is possible for low levels of vertical load and/or low friction coefficients.

These results were confirmed by later researches which focused on the cyclical behaviour of the material. Within this ambit different testing techniques have been adopted in the literature, namely quasi-static cyclic tests, pseudo dynamic tests and dynamic shake table tests. According to Calvi *et al.* (1996), despite the latter tests simulate with accuracy the effects of earthquake on the structural elements, cyclic quasi-static tests enable more accurate measurements of forces and displacements on the specimen and therefore the record of the damage becomes easier. Different experimental researches followed both on brickwork Magenes and Calvi (1997), Anthoine *et al.* (1995), Bosiljkov *et al.* (2003) and on dry-stack stonework Ceradini (1992), Vasconcelos and Lourenço (2009).

In the meanwhile, a different approach started to develop in 1980, when, aiming at deriving a constitutive identification of masonry as an homogeneous medium for performing more efficient numerical analyses, experimental tests on masonry panel were conducted by inducing within the specimen uniform in-plane states of stress. Within this ambit, the most complete set of experimental

data on the in-plane behaviour of masonry are from Page (1981,1983) and Dhanasekar *et al.* (1982) who tested 102 half scale solid brick panels submitted to proportional biaxial loading, Figure 2.2. In the linear elastic range, no significant difference in stiffness in directions normal or parallel to the bed joint is found, Dhanasekar *et al.* (1982). On the other hand, in the non-linear range the material shows a remarkably anisotropic behaviour. In biaxial compression-tension regime, the failure modes encountered are dependent on the direction of the applied loads with respect to the orientation of mortar joints. Crack propagation along the joints is encountered, which in some cases is accompanied by cracking of the bricks.

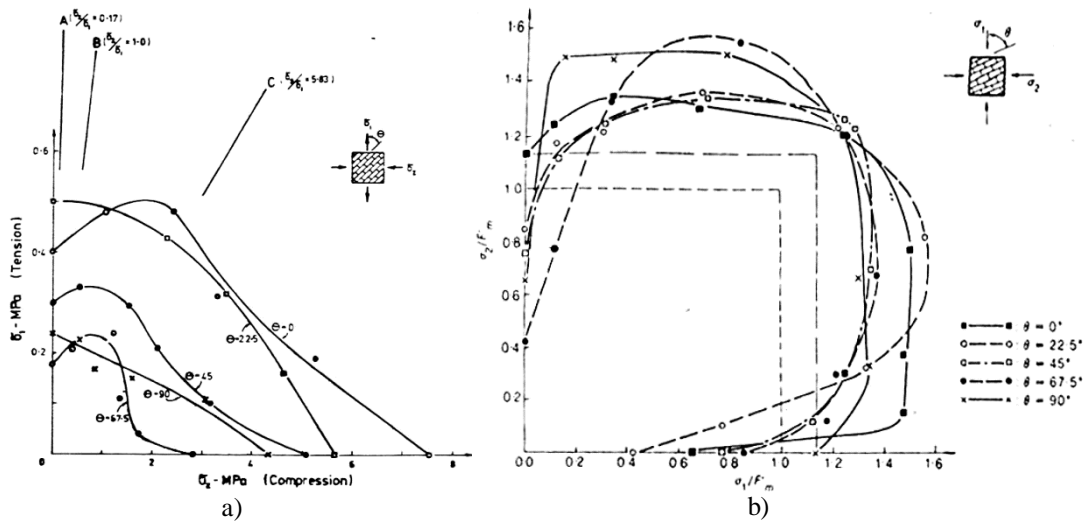


Figure 2.2 Strength envelop of masonry derived by Page (1981,1983) for different angles (θ) between the in-plane load (σ_1, σ_2) with respect to bed joint orientation: tension compression regime (a) and biaxial compression regime (b).

When masonry is loaded in biaxial compression, the bed joint orientation does not play a significant role for most stress combinations and failure typically occurs by splitting of the specimen at mid-thickness, in a plane parallel to its free surface. However, when one of the principal stress dominates failure occurs by cracking and sliding of the joints and cracking of the bricks. The strength envelope obtained by Page is of limited applicability for cases in which different components or different geometry is encountered. The biaxial strength of other types of masonry has been investigated by Ganz and Thürlimann (1982) for

hollow clay masonry, Guggisberg and Thürlimann (1987) for clay and calcium-silicate masonry and Lurati *et al.* (1990) for concrete masonry.

All the abovementioned experimental tests show that joints cracking tends to localize in correspondence of the interface between mortar and brick, which constitutes the weakest link of masonry. Aiming at studying the behaviour of such interface, tensile and shear tests were carried out in the literature on small assemblage of mortar and bricks, see Atkinson *et al.* (1989), Van Der Pluijm (1993) and Jukes and Riddinton (1997) for a detailed description. The results so far collected show that the non-linear behaviour of the joint is governed essentially by two phenomena, namely tensile cracking and shear slip, which are both characterized by low values of fracture energy. The relation between shear and compressive load was found to be linear with a friction angle of about 36° while a ratio between tensile strength and cohesion varying from 1.3 to 2.4 was recorded.

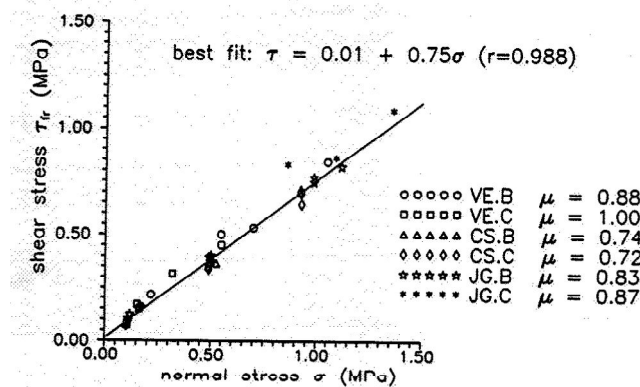


Figure 2.3 Shear peak strength of masonry joints as a function of the compressive stress applied, Van Der Pluijm (1993).

Mechanical behaviour of out-of-plane loaded masonry

Experimental tests on masonry walls undergoing out-of-plane actions are rather complex to perform. Within this ambit, static tests may be not representative of the phenomena that actually take place in real structures stroked by seismic shocks. Therefore the technical community in the last 20 years mainly investigated the dynamic response of masonry wall under out-of-plane inertial forces.

The first and probably the largest to date experimental campaign on walls dynamically tested out-of-plane is that performed by the Agbabian-Barnes-Kariotis, ABK (1981). 22 vertical spanning strip walls, whose height ranged between 3.05 m and 4.88 m, and whose height-to-thickness ratio varied between 14 and 25, have been subjected to both synchronous and non-synchronous accelerograms at the base and at the top. The authors have recognised the existence of a dynamic stability reserve, which explained why the walls, although cracked and rocked, did not collapse. Similarly, a vertical simply supported wall has been considered by Baggio and Masiani (1991), who tested out-of-plane small scale unreinforced masonry and unreinforced concrete walls, using harmonic excitations. Griffith *et al.* (2004) have considered harmonic, impulsive and earthquake ground motion while testing 14 vertical spanning strip walls, 1.5 m tall, having a height-to thickness ratio variable between 13 and 28 approximately. Simsir *et al.* (2004) have tested three single cell, single storey prototypes, with reinforced masonry walls acted in-plane and unreinforced masonry walls acted out-of-plane, connected by horizontal diaphragms of varying stiffness. The walls were approximately 1.9 m tall, with a 21 height-to-thickness ratio. The out-of-plane loaded wall cracked and rocked when the floor load has been reduced compared to the wall self-weight. Meisl *et al.* (2006) have performed tests on four simply supported walls. The unreinforced masonry consisted of three leafs brick ashlars, with header units every seven courses. The specimens were 4.25 m tall, and had a 12 height-to-thickness ratio. Two of the walls have been built without wetting the units before laying them on the mortar, in order to engender poor adhesion. Nonetheless, rocking mechanisms have been observed.

Wilhelm *et al.* (2007), as part of a campaign involving six vertical spanning strip walls built using hollow clay bricks, being 2.4 m tall and with height-to-thickness ratio varying between 12 and 19, have presented the results for the first specimen, laid with a very weak mortar. They observed the formation of a mechanism, whose hinge moved along the wall height.

Unreinforced brick masonry parapet walls have been tested by Bariola *et al.* (1990) and by Lam *et al.* (1995). Rigid body rocking and sensitivity to ground motion details has been observed in both cases. Block-like stone elements have been tested by Liberatore and Spera (2001) and by Peña *et al.* (2006). The former investigators, who tested 12 blocks 0.6-1.2 m tall and with height-to-thickness ratio varying between 6 and 10, have investigated impulsive energy damping and the relevance of other degree of freedoms. The latter investigators, who tested 4 blocks 0.46-1.0 m tall and with height-to-thickness

ratio varying between 4 and 6, have focused on the comparison between an analytic model and a distinct element model. Recently, El Gawady *et al.* (2011) presented an experimental campaign on block masonry walls undergoing dynamic excitation. Two types of masonry and different slender ratios have been investigated. Additionally, different materials have been adopted for building the interface at base of the wall. The results outlined the strong influence of such material on the overall response of the system and on the dissipation of energy: the softer is the interface the higher is the dissipation of energy. Moreover such dissipation proves continuous when soft material is adopted while tends to concentrate on impact when stiff material is adopted.

Strategies for modelling masonry under in-plane loads

The experimental campaigns conducted in the last 30 years reveal that masonry shows different mechanical properties depending on the direction of the applied load with respect to the orientation of mortar joints, which act as plane of weakness. The main issue related to modelling of masonry in-plane loaded is to capture such anisotropic behaviour and may be addressed by following different strategies which are briefly described in the following paragraphs.

Micro-modelling

The most intuitive way for simulating masonry behaviour is to use a Finite Element model where each unit and mortar joint is represented by means of continuum elements. In this context many contributions were given in the literature by assigning to the constituents non linear constitutive relations based on damage and plasticity theories, Sayed-Ahmed and Shrive (1996), Litewka and Szojda (2006), Massart *et al.* (2004) and Berto *et al.* (2005), Lourenço and Pina-Henriques (2006). Additionally, mortar/brick interface may be accounted for in the model, see Rots (1991), aiming at achieving a further level of detail. This modelling approaches, regarded as refined micro-modelling, prove able in reproducing all the failure modes of masonry as progressive deterioration of the joints and compressive failure due to Poisson's effect, Berto *et al.* (2005), Brenchich and Gambarotta (2005). On the other hand, this strategy is computationally intensive and can be adopted for reproducing the behaviour of limited portions of real structures, Figure 2.4a.

A simplification may be introduced by representing masonry as an assemblage of block modelled as continuum elements separated by joints modelled as zero-thickness interfaces, Figure 2.4b. The Distinct Element Method, which is based on this strategy, was originally proposed by Cundall (1971) for the analysis of rock masses and then applied to the case of masonry by Azevedo *et al.* (2000) and de Felice (2011) among others. The same approach was adopted within the framework of the Finite Element Method by Page (1978), Rots (1991), Lofti and Shing (1994), Gambarotta and Lagomarsino (1997a), among others. This modelling strategy, regarded as simplified micro-modelling, reduces the computational costs of the analysis and makes it possible to reproduce failure modes of masonry related to cracking and sliding of the joints. On the other hand, the interface model does not give information on the Poisson's interaction between mortar and brick and, therefore, cannot directly reproduce failure modes of masonry in compression. The latter limit may be overcome by lumping all the non-linear features of masonry behaviour within the interface and adopting ad hoc constitutive models which include cracking, sliding and crushing modes of failure, Lourenço and Rots (1997a), Chaimoon and Attard (2007).

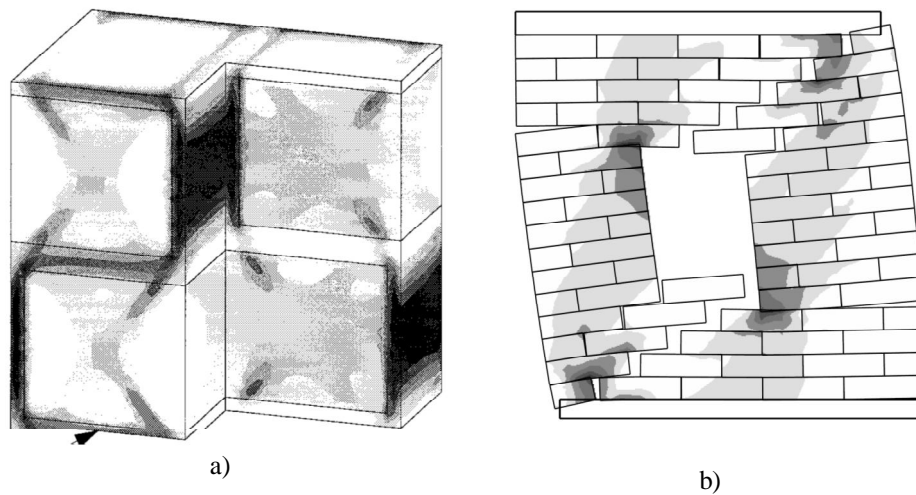


Figure 2.4 Examples of refined (a), Anthoine (1997) and simplified (b), Lourenço (1997a) micromodelling.

Macro-modelling

Even by introducing simplifications concerning the behaviour of mortar joints, the computational effort needed to perform structural analysis precludes the use of micro-modelling approaches for engineering applications involving real size buildings. In the latter cases, macro-modelling approaches seem preferable since they may combine low computational costs and reasonable accuracy. The basic idea is to represent masonry assemblage as an homogeneous material by accounting for the presence of mortar joints in an average sense. Within this context, many strategies were developed in the literature.

The least-refined strategy consists in dividing the structure in macroelements (*i.e.* shear walls, lintel beams) employing truss, beam or plate element and assigning them a proper constitutive relation expressed in terms of overall force-displacement, Brencich and Lagomarsino (1998), Magenes and Della Fontana (1998) among others. These models rely on a simple representation of the structure and require few essential information which make it possible to perform both static and time-history non linear analyses in a limited amount of time. For these reasons, the latter approach is adopted by the majority of commercial programs oriented to the analysis and design of masonry structures. Despite important developments occurred regarding the validation with respect to valuable experimental data, large errors in predicting structural behaviour may derive by adopting inadequate structural elements or constitutive relationships.

A more refined approach makes use of the Finite Element Method, which requires a constitutive identification of masonry expressed in terms of local stress-strain relationship. In this context, many authors adopted the smeared crack model, originally developed for concrete, aiming at predicting cracking and failure of masonry walls. The limits of the latter approach are discussed in detail in Lofti and Shing (1991), Giordano *et al.* (2002).

The first *ad hoc* constitutive model for masonry was developed by Dhanasekar *et al.* (1985) on the basis of the extensive experimental campaign conducted by the authors on masonry wallets under biaxial states of stress.

Further failure criteria for masonry were derived by Ganz (1989), Alpa and Monetto (1994), Andreaus (1996) by means of mechanical reasoning on the interaction between masonry components within a wall subjected to in-plane loads. The cited authors proposed rather complex yield surfaces that almost preclude the use of modern numerical algorithms and an accurate representation of inelastic behaviour (hardening and softening).

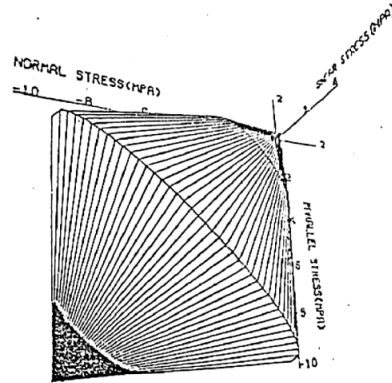


Figure 2.5 Empirical strength criteria proposed by Dhanasekar *et al.* (1985).

Lourenço *et al.* (1998) overcame this limitation proposing a composite criterion, obtained by the combination of Hill-type and Rankine-type criteria, which includes different hardening/ softening behaviour along different material axes, Figure 2.6.

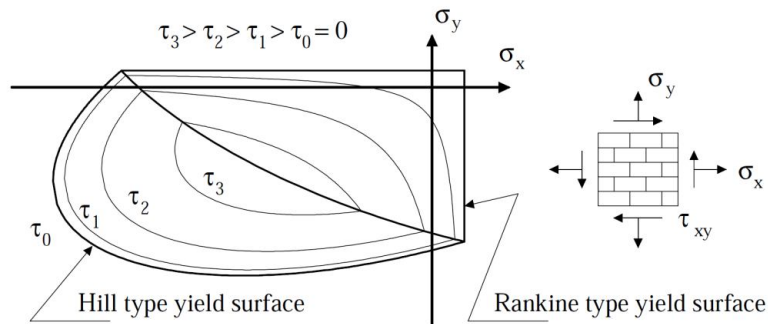


Figure 2.6 Combined strength criterion adopted for modelling in plane loaded masonry, Lourenço *et al.* (1998).

Standing the good agreement with the experimental tests, the abovementioned constitutive relations take into account only in phenomenological way the effects of brick and mortar arrangement within the brickwork. Accordingly, models calibrated for specific type of masonry can be hardly adopted when different constituents and geometry are encountered. Therefore “phenomenological” criteria need to be calibrated either by performing experimental tests on wallet, which are usually costly due to the large size of the specimens and required testing equipment, or by performing numerical analysis based on micro modelling approaches.

Multi-scale approaches

An alternative and less expensive approach to experimental tests is to measure the individual properties of unit and mortar on small samples and, then, to use a theoretical model that combines the information from the components and makes it possible to obtain masonry overall properties. Because of its importance, this latter issue has been the subject of many investigations during the last fifty years. One of the first attempts was made by Haller (1958), which developed a theoretical model suitable for predicting the deformation of a stack bonded masonry prism, by defining a set of compatibility and equilibrium equations between the components under simplifying assumptions, *i.e.* uniform stress fields within mortar and brick. A similar scheme was adopted by Shrive and England (1981) and Brooks (1990), with models that extend the formulation to the case of running bond masonry.

The abovementioned approaches are limited to the case of masonry subjected to vertical loads in the elastic range. The analysis of structures subjected to vertical and horizontal loads, where brickwork acts either as load-bearing elements or in conjunction with a structural frame, requires a better characterization of masonry as a continuum material both in the elastic and inelastic ranges. This can be achieved by resorting to multi-scale approaches. The basic idea derives from the intuition that the response of heterogeneous materials may be analyzed at different scales of observations passing from macroscopic scales to finer and finer microscopic scales. In the coarser level the material is represented roughly by means of a continuum model whose response is derived by bridging information at the proper underlying level. In this way it is possible to retain memory of the internal microstructure without forsaking the advantages deriving from a continuum scheme. In the case at hand, two different levels may be considered: the macroscopic one, which is comparable to the dimensions of the wall or of the structure under consideration, and the microscopic one, which is comparable to the dimensions of brick and mortar phases.

The terms “multi-scale” includes many strategies developed in the literature that differ in terms of the up-scaling method, *i.e.* the method for transferring information at different scales, Weinan *et al.* (2009). In the present work attention is restricted to the multi-scale approaches that make use of the asymptotic homogenization theory Bensoussan *et al.* (1978), Sanchez-Palencia (1980), Suquet (1987). The latter theory is based on the asymptotic expansion of

the field variables in powers of a parameter representing the ratio between the characteristic length of the heterogeneities and the characteristic length of the whole domain under consideration. When the abovementioned ratio is small enough, the macroscopic constitutive relation of heterogeneous materials may be obtained by solving an auxiliary boundary value problem, also called localization problem, defined at the microscopic scale on a Representative Volume Element of the medium (RVE). Both first- and second-order homogenization were applied in the literature to the case of masonry.

The first order asymptotic homogenization relies on the classical linearization of the macroscopic deformation map meaning that both micro- and macro- scales are represented as Cauchy continua. In the specific case of masonry the problem was addressed by Anthoine (1995) in a rigorous way and solved in the elastic range by means of the finite element method. The use of finite elements to solve the auxiliary boundary value problem in a full three-dimensional manner usually requires intensive numerical computations so that the problem is usually tackled under plane conditions, by taking advantage of the small thickness of masonry walls with respect to the other dimensions.

The opportunity of achieving an analytical solution of the localization problem proves particularly attractive. For this purpose the homogenization technique was applied in literature introducing simplifying assumptions that made it possible to handle the problem analytically. In most cases the constant strain, or Voigt assumption, is made together with simplifications concerning the brickwork geometry.

One approach is to neglect the presence of head joints and to consider masonry as a periodic layered material made of alternating layers of brick and bed joint, Carbone and Codegone (2005).

Another approach is to perform the homogenization in two steps, Pande *et al.* (1989), defining first the equivalent homogenous properties of the horizontal courses made of bricks and head joints and then representing running bond masonry as a periodic layered material made of bed joints and of the homogenous courses defined in the first step. Analogous assumptions have been made by Pietruszczak and Niu (1992). The above mentioned procedures do not fully address the influence of bond patterns on masonry overall behaviour, since the head or bed joints are not introduced simultaneously, Lourenço and Rots (1997b).

A further approach consists in treating joints as zero-thickness interfaces, de Felice *et al.* (2001,2010), Cecchi and Sab (2002a). The simplification introduced makes it possible to derive masonry elastic properties in closed form

taking due account of the arrangement of units while losing the Poisson interaction between the constituents and its influence on masonry overall behaviour.

Zucchini and Lourenço (2002) followed an “engineering” approach by introducing simplified deformations mechanisms over the basic cell which are derived from observations of finite element analyses results. The equivalent properties of masonry as a homogeneous material are then obtained by imposing a set of equilibrium and compatibility equations between each constituent.

The extension of the asymptotic homogenization approach to the non linear range is not straightforward. An attractive solution consists in defining an homogenized yield surface delimiting the locus of the admissible macroscopic stress. The latter issue maybe achieved by applying the homogenization techniques within the framework of limit analysis. After the pioneer paper of De Buhan and de Felice (1997), Figure 2.7, many other works followed which applied either kinematic and static method for deriving, respectively, upper bound and lower bound estimates for the failure surfaces, Milani *et al.* (2006a, 2006b, 2006c, 2008), Cecchi and Milani (2008).

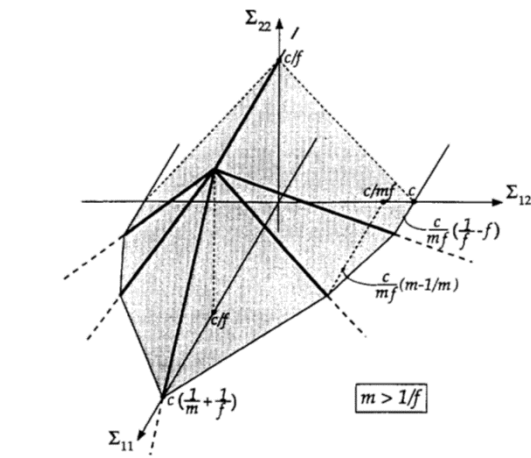


Figure 2.7 Strength domain of brick masonry as an homogenized material in space of macroscopic stresses, De Buhan and de Felice (1997).

Despite the fact that limit analysis approach proved able in predicting the collapse of in-plane and out-of-plane loaded walls, it is unable to provide information in terms of displacement. In order to trace the complete equilibrium path of the structure, de Felice *et al.* (2010) endowed the domain obtained by means of the limit analysis with an elasto-plastic constitutive relation defined at

the macroscopic scale. The advantage of the cited approach is that the up-scaling process is performed once so that during the analysis the material is always treated as an homogeneous medium. The latter method makes it possible to apply the common integration scheme developed for multi-surface plasticity. On the other hand, in spite of the quasi-brittle behaviour of mortar and brick which would require non associative flow rule and finite ductility, perfect plasticity assumption and associated flow rule of the constituents is considered in this context.

In order to use constitutive laws for the components covering the abovementioned phenomena, a transition between micro- and macro- scales is required at each step of the analysis. One of the earliest paper in this direction is from Luciano and Sacco (1997) who proposed a discrete damage evolution law for masonry obtained by schematizing the damage process by only few possible damaged state of the material. Each damaged configuration is characterized by a certain distribution of cracks and by an overall compliance matrix of the homogeneous material which may be evaluated by means of finite element analyses. Fixed paths of damage are then identified, *i.e.* the evolution from a damaged state to another. From the macroscopic point of view the damage evolution is obtained by assigning to the homogeneous material the reduced compliance matrix which pertains to the damage state reached. More in general, the scale transition may be handled by means of computation homogenization procedure, Anthoine (1997), Ma *et al.* (2001), Massart *et al.* (2004, 2005). In order to reduce the typical high costs of the latter approach, transformation field analysis, originally proposed by Dvorak (1992), was adopted by Sacco (2009), Marfia and Sacco (2012) for deriving the non-linear behaviour of in-plane loaded masonry. The author assumed a linear elastic behaviour of the brick while introduced a constitutive law for the joints including damage and friction which makes it possible to reproduce the cyclical response of mortar. In order to reduce to the minimum the complexity of the problem, the scale transition may be defined explicitly *a-priori*. Masiani and Trovalusci (2003) assumed a direct relation between the macroscopic strain field and the microscopic displacement field defined on the RVE, where masonry is seen as a system of rigid block connected by frictional interfaces. The up-scaling process is then made by imposing the Hill-Mandel equality of the works computed on the two scales. This approach introduces a lack of equilibrium at the microscopic scale which is expected to have effects on the macroscopic scale too. For instance one effects is the mismatching between the deformability of the Cauchy and Cosserat identifications proposed by the cited authors in the limit case where the

dimensions of the blocks tends to be infinitely small with respect to the dimension of the structure, see Salerno and de Felice (2009) and Trovalusci and Masinai (2003).

Another approach consists in handling the non linear homogenization by treating masonry as a stratified material. In this context the main contributors were Lourenço (1997b), who considered elasto-plastic behaviour of the constituents, Gambarotta and Lagomarsino (1997b) and Uva and Salerno (2006), who introduced ad-hoc constitutive relation for the joints which includes damage and plasticity and accounts for the cyclical response of mortar. By neglecting the presence of head joints, the latter models are thought to overestimate the response of masonry under shear loading. In order to overcome these limitations Zucchini and Lourenço (2004, 2007, 2009) proposed a non-linear homogenization procedure based on a micromechanical model for masonry which accounts for the whole set of mortar joints and introduces a coupled damage-plasticity model for the constituents. This approach may be referred to as “*engineering*” approach since the response of the RVE under a generic state of stress is derived as a superimposition of two mechanical problems defined separately, the first one in which the RVE undergoes normal axial loads and a second one where the RVE undergoes shear loads. Within this ambit falls the model developed by Calderini and Lagomarsino (2008) who performed the homogenization by treating the joints as interfaces and analyzing the response of the RVE under different deformation modes. The cited authors defined ad-hoc constitutive relation for the components which accounts for tensile cracking, sliding and compressive crushing and proves able to reproduce the cyclical behaviour of the materials.

The first order homogenization approach is by now well-established and widely used in the scientific and engineering community but it presents two major disadvantages, Geers *et al.* (2011):

- The method is based on the separation of scales and is, therefore, not suited for critical regions where high deformation gradient is expected. Thus, when softening behaviour is considered the model is affected by well-known localization and mesh dependency problems.
- The separation of scale assigns an infinitely small size to the RVE so that the method neglects size effects.

In order to overcome part of the mentioned limits, second-order homogenization techniques, based on a second order Taylor series expansion of the deformation map, were developed in the literature. The latter approach

couples a Cosserat continuum at the macroscopic scale with a classical continuum at the microscopic scale. In the linear elastic range Masiani *et al.* (1995) referred to a lattice model and derived an identification of the elastic constant of masonry as an analytical function of the shape, size and arrangement of the components. Recently, Salerno and de Felice (2009) compared the capability of Cosserat and Cauchy identification to reproduce the elastic deflection of masonry treated as a rigid blocky system. In the inelastic range Masiani and Trovalusci (1996) and Trovalusci e Masinai (2003) developed multi-scale procedures referring to a microstructural model consisting in rigid block connected by non-linear springs obeying to a Mohr-Coulomb criterion. Later, Salerno and Uva (2002) proposed a multi-scale procedure by assuming an explicit down-scaling process relating the Cosserat macroscopic strain measure with the strain measure at the local level. Here masonry is handled as a system of rigid block connected by interfaces, which are endowed with a constitutive law including damage and friction. Finally, the Hill-Mandell work equality is adopted by the cited authors for performing the up-scale process. More recently, starting from the original work by Sacco (2009), Addessi *et al.* (2010, 2012) proposed an enhanced non linear homogenization approach based on the transformation field analysis. The main benefits of the second-order approach are:

- The method accounts for a microscopic length scale.
- The problem of moderate localization is resolved along with the mesh dependency at the macroscopic scale.

On the other hand, if localization appears with a band which is below the RVE size, even the second order homogenization fails in reproducing closely the kinematics of the problem.

In the case of intense localization the continuous-discontinuous scale transition may be adopted. It consists in the definition of a localization band which allows for strain discontinuities at a macroscopic scale. The jump of displacement is driven by the resolution of a boundary value problem defined on the RVE. The first approach based on this concept was developed in Massart *et al.* (2007). An alternative consists in resorting to the substructuring or multigrid approach, Brasile *et al.* (2007), which is based on an iterative scheme using two different, local and global, modelling of the masonry mechanics simultaneously. The local model represents the interaction between adjacent bricks by means of the nonlinear response of mortar joints modelled as springs at contact. The latter model is a linearized Finite Element approximation of the previous model,

defined at the rough scale of the wall, and is used as iterative pre-conditioner to accelerate the iteration.

Strategies for modelling masonry under out-of-plane loads

The dynamic behaviour of walls undergoing out-of-plane forces is rather complex, due to both the discontinuous and non-homogeneous nature of masonry, and the interaction with the remainder of the building. Bearing in mind that these types of mechanism usually develop large displacements and are affected by second order effects, the definition of models able to handle on the whole this set of aspects constitutes a true challenge for the technical community.

The classical approaches adopted for modelling out-of-plane loaded walls rely on simple plane model where the wall is represented as a single or a system of rigid blocks. This assumption introduces important simplifications, since the number of parameters governing the problem strongly reduces and the equations of motion may be solved by accounting for finite displacement either under monotonic or dynamic loads.

Within this ambit, the pioneer work is from Housner (1963) who formulated an analytical model for evaluating the response of a free-standing rigid parallelepiped block, also named inverted pendulum, under free-oscillations and acceleration pulses. The interface at the base of the wall is rigid and the kinematics of the system is expressed in terms of the rotation of the block only, Figure 2.8.

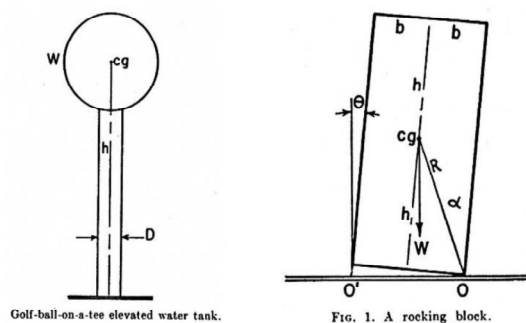


Figure 2.8 Housner (1963) inverted pendulum.

The dissipation of energy during the motion has been introduced when the block impacts the foundation, being the amount of energy lost expressed by means of a coefficient of restitution as a function of the velocity of the block immediately before the impact. The main findings of Housner research is that,

unlike the classical single-degree-of-freedom oscillator, the inverted pendulum has a period of vibration that depends on the amplitude of the motion. This model, despite its simplicity, makes it possible to capture the essential features of the response of a monolithic wall undergoing out-of-plane actions since accounts for second order effects and for the energy dissipation over impacts.

Later on, Housner inverted pendulum has been refined by many authors. Aslam *et al.* 1980 considered time-history acceleration at the base of the block instead of dynamic pulse. Plaut *et al.* (1996) studied the behaviour of a parallelepiped block resting on an inclined foundation, Figure 2.9a. These models proved not feasible for the analysis of real buildings where the presence of transversal walls introduces a further constrain to the out-of-plane motion of the walls. In order to include this aspect, Hogan (1992), Liberatore and Spera (2003) and Sorrentino *et al.* (2008) analyzed the case of free standing rigid blocks which on one side were free to rotate while on the opposite side were constrained by the presence of transversal elements, Figure 2.9b.

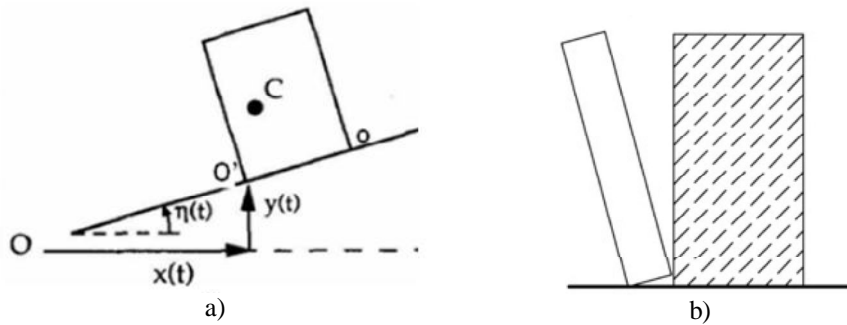


Figure 2.9 Enrichments of Housner's model: (a) block resting on inclined foundation, Plaut *et al.* (1996), and (b) block constrained on one-side by transversal walls, and Sorrentino *et al.* (2008).

A major enrichment of Housner's inverted pendulum has been introduced by Doherty *et al.* (2002) and Sorrentino *et al.* (2008). Starting from the discrepancies found between the original model and experimental evidences, the cited authors introduced some imperfections in the behaviour of the parallelepiped block by adopting a three-linear relation between the restoring force and the displacement of the block instead of the bilinear relation envisaged by Housner's approach, Figure 2.10. In this way an initial finite stiffness and a reduced strength of the block are introduced, which made it possible to obtain a reasonable matching with experimental results.

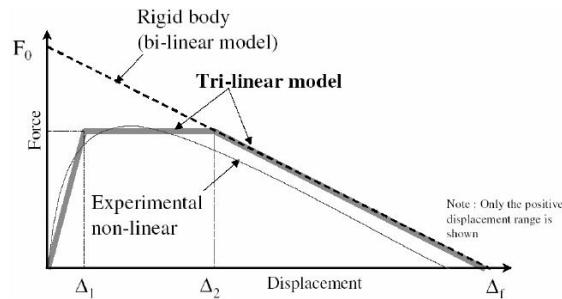


Figure 2.10 Three linear relation between the resorting force and the out-of-plane displacement of the block proposed by Doherty *et al.* (2002) and Sorrentino *et al.* (2008).

Other approaches assumes either a Winkler-type foundation, Phycaris and Jennings (1984), Blasi and Spinelli (1986) or that the base of the block has a cylindrical shape, Capecchi *et al.* (1996), Figure 2.11. Both this type of assumptions introduce a smooth transition between positive and negative rotation of the block, a finite initial stiffness and a reduced strength with respect to Housner's inverted pendulum. More precisely, this smoothness is related to the progressive migration during the motion of the hinge point located at the base of the wall from one corner of the foundation to the other.

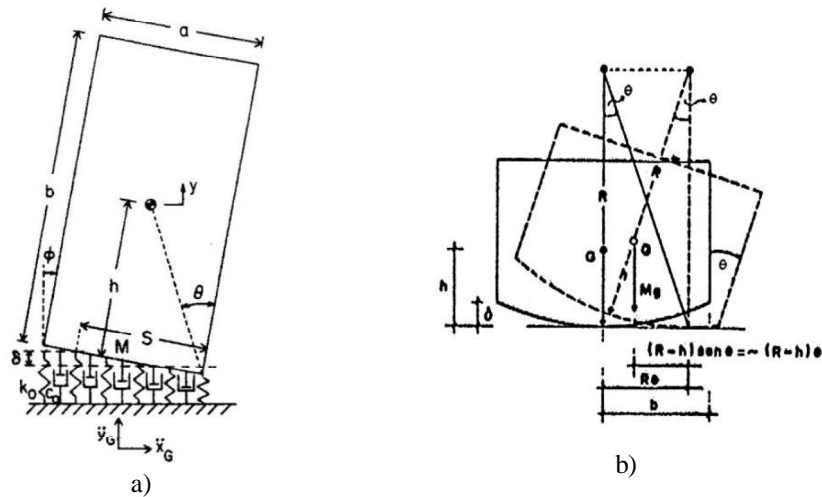


Figure 2.11 Model proposed by (a) Phycaris and Jennings (1984) and (b) Capecchi *et al.* (1996).

The approaches developed so far assume that the behaviour of the wall under out-of-plane actions may be assumed as monolithic. This assumption holds true as far as transversal bond is ensured by a good interlocking of masonry unit throughout the thickness of the wall. When dealing with regular masonry the latter condition is usually encountered. Conversely when historical masonry is analyzed, the hypothesis of monolithic behaviour of the wall during rocking motion may not be acceptable anymore.

The effect of masonry morphology on the behaviour of historical masonry out-of-plane loaded has been investigated by de Felice (2011) with reference both to regular dry block masonry (*opus quadratum*) and to rubble stonework. The methodology proposed, which is based on the distinct element method, relies on a plane model of the wall where masonry is represented as an assembly of rigid block separated by non-linear interfaces, Figure 2.12. This approach abandones the hypothesis of monolithic behaviour of the material and accounts for the actual disposition of the units throughout the thickness of the wall. The use of the distinct element method may be regarded as the natural evolution of Housner's approach. As a matter of fact, this method makes it possible to analyze the static and dynamic behaviour of a system made by several rigid blocks separated by non-linear interfaces by solving the equation of motion under the assumption of finite displacement.

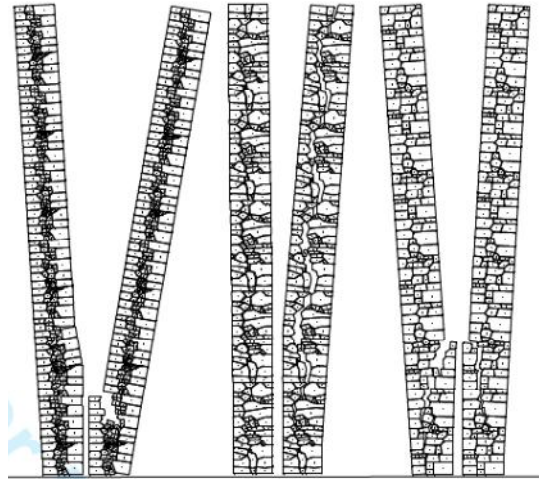


Figure 2.12 Rubble masonry walls out-of-plane loaded analyzed by means of the distinct element method, de Felice (2011).

De Felice and Giannini (2001) investigated the effects of the connections between the wall which experiences rocking and transversal walls assuming that at their intersection the bond is provided by unit interlocking. Two types of mechanisms have been considered: the overturning of the façade due either to a stair step vertical crack at the corner or a diagonal crack on the transversal wall, Figure 2.13.

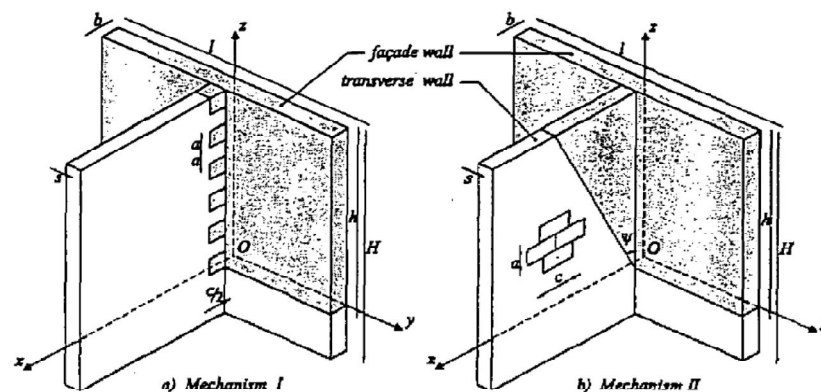


Figure 2.13 Mechanisms analyzed by de Felice and Giannini (2001) by accounting for façade-transversal wall bond.

The models presented up to now, while taking into consideration in approximate way the arrangement of the units within the wall and the bond with other structural elements of the buildings, *i.e.* floors, transversal walls etc..., do not account properly for three dimensional effects. More complex failure mechanisms may be analyzed in a complete three dimensional framework by subdividing the structure in a system of rigid block, Restrepo-Velez (2004). Anyway the problem becomes increasing difficult so that the use of dynamic analysis is precluded in this case.

In the last ten years new approaches have been developed which renounce to follow the complete motion of out-of-plane mechanisms under dynamic actions. For a given structure, their main goal is to define the minimum collapse load multiplied and the related mechanism, *i.e.* the portion of the structure that tends to fail out-of-plane, by performing static push-over finite element analysis under the assumption of small displacement. These approaches may account for the texture of the material, for three dimensional effects and for the interaction with the remainder of the structure but renounce to catch the features of the phenomenon related to second order effects. Within this ambit the same strategies presented for the case of in-plane loaded walls have been followed in

the literature, *i.e.* macro-modelling and multi-scale approaches. An example of macro modelling approach is presented in Lourenço (2000) where the combined Hill-Rankine orthotropic model developed for in-plane loading has been extended to a multilayered shell in order to replicate the behaviour of masonry walls out-of-plane loaded.

The homogenization technique has been widely used both in the elastic range, Cecchi and Sab (2002b,2004,2007), and in the framework of the limit analysis theory, Mistler *et al.* (2007), Milani *et al.* (2006c,2008), Cecchi *et al.* (2007), Figure 2.14. Within the ambit of multi-scale approaches, the main contribution has been provided recently by Mercatoris *et al.* (2009,2010) who performed a computational two scale homogenization where the localization of damage both at the microscopic and macroscopic scale is handled by a criterion based on acoustic tensor adapted to shell kinematics. Except for the methodologies based on the limit analysis theory, the remaining approaches still need to be validated in terms of their applicability to real size structures.

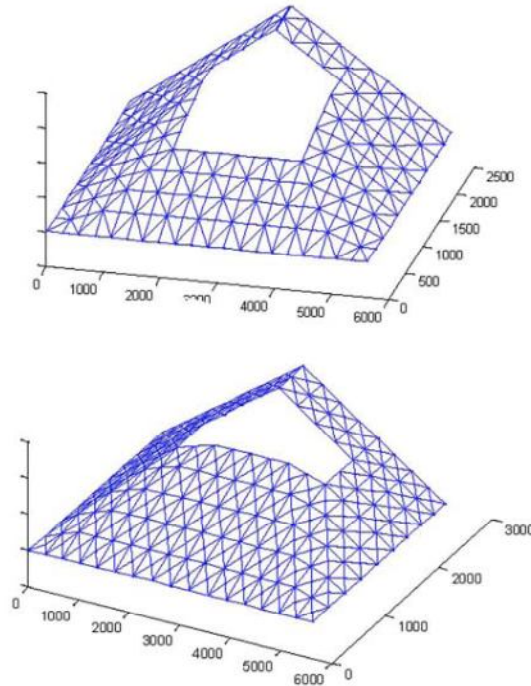


Figure 2.14 Out-of-plane limit analysis of masonry walls based on homogenization technique, Milani *et al.* (2006).

3. Out-of-plane loaded masonry walls: experimental tests and distinct element modelling

Damages observed after strong earthquakes have shown that perimeter walls are the most vulnerable elements of existing masonry buildings. Because of seismic ground motion, they are prone to separate from internal structures, such as transverse walls and horizontal floors, and to overturn out-of-plane, Figure 3.1.



Figure 3.1. L'Aquila (Central Italy), after the April 6, 2009 earthquake. a) Church of San Pietro di Coppito; b) Oratory of San Giuseppe dei Minimi.

The analysis of the dynamic behaviour of walls undergoing out-of-plane inertia forces is rather complex, because of both the discontinuous and nonhomogeneous nature of masonry and the interaction with the remainder of the building. Such a problem has been addressed in the past by means of experimental campaigns which have been mainly devoted to study the behaviour of artificial brick or block masonry or of single-block stone elements. So far, no forced vibration tests have been performed on natural stone masonry, which is more frequent in existing masonry buildings, especially in the Mediterranean area. Moreover, no such tests have considered a façade laterally restrained on one side by transverse walls (so called one-sided rocking), although analytic

models have been presented recently, Sorrentino *et al.* (2008) and references therein. All the previous investigations have shown the capacity of rocking mechanisms to survive earthquake ground motion although the wall was cracked. This suggests the importance of accounting for the post-cracking capacity of a wall. Attempts have been made both in technical literature, Doherty *et al.* (2002), and in seismic codes, CSLLPP (2009), by means of displacement based static procedures, as well as dynamic analyses de Felice and Giannini (2001) and Sorrentino *et al.* (2008). However, there is the need to develop experimentally validated dynamic models in order to perform non-linear time history analyses as well as to use them for the calibration of equivalent static procedures.

The present chapter is devoted to study the out-of-plane seismic behaviour of a wall, from now on referred to as the façade, which on one side is restrained by two transverse walls. The façade is carrying its own weight only, as is the case in existing masonry building with floors resting on transverse walls. A shake table experimentation on a natural scale specimen is presented and the results of 34 tests under four recorded accelerograms scaled to different amplitudes are discussed. A non-linear dynamic approach based on the Distinct Element Method (DEM) is developed and the related numerical time histories analyses are compared to the experimental results. Finally, the Italian seismic assessment code procedure is checked against both experimental results and numerical time histories, obtained for a wider set of wall geometries.

Test summary

The experimental results that are presented in this section are part of a wider experimental campaign investigating the behaviour of unreinforced masonry under out-of-plane seismic action. The campaign includes different wall specimens tested at different stages of their behaviour: undamaged, cracked, and strengthened. For the purpose of the present thesis, one specimen is considered, consisting of the façade, and two transverse walls, resulting in an overall U-shaped configuration. The specimen is in a cracked state, that is the façade is separated from the transverse walls, and is subjected to out-of-plane seismic input as shown in Figure 3.2. The choice of a pre-cracked specimen results in a safe assumption, which is justified in the practice, in view of the uncertainties on the effective quality and mechanical characteristics of the connections between walls in existing masonry structures.

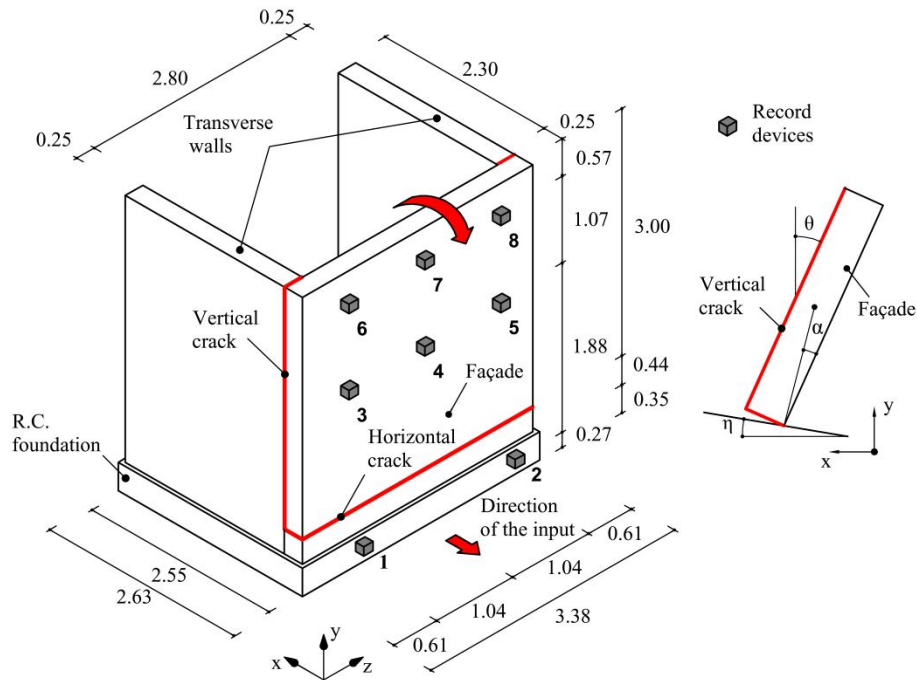


Figure 3.2 Test setup: each marker corresponds to an accelerometer and a displacement wire-transducer. All measurements are in meters.

The façade is 3.30 m long, 3.44 m height and 0.25 m thick; transverse walls have the same height and thickness as the façade and are 2.55 m long. The first masonry course is laid within a reinforced-concrete foundation, which is 3.38 m long, 2.63 m deep and has a 0.35×0.35 m cross section. A horizontal crack, located 0.44 m above the foundation, and two vertical cracks, between the façade and the transverse walls, exist as a consequence of previous tests. The walls are built with 250×370×110 mm tuff units and hydraulic lime mortar. The tuff has the following mean properties: bulk specific weight 12.06 kN/m³, cubic compressive strength 5.98 MPa, elastic modulus 1575 MPa. The mortar has mean cubic compressive strength 4.08 MPa, elastic modulus 2038 MPa, tensile strength 0.84 MPa (bending test).

The specimen is connected to the shake table through seven double UNP 100 steel channels passing through the foundation and anchored to the shake table by means of steel rods (Figure 3.3). Six steel heels, namely four at the base of the façade and one at the base of each transverse wall, provide a further horizontal restraint against sliding of the foundation.



Figure 3.3 View of the specimen with the anchor devices and the retaining structure:
UNP 100 steel channel (dotted line) and steel heels (solid line)

The transverse walls are prestressed through vertical rods, in order to avoid any out-of-plane damage. The façade is provided with a retaining structure, inclined outwards, consisting of a steel mesh stiffened with steel sections, in order to protect the shake table as well as to restore the vertical position of the

specimen once overturned. The shake table is located in the Department of Innovation of the ENEA Casaccia research centre in Rome: it has a 4.0 m wide square shape, six degrees of freedom and is able to provide displacement or acceleration time-history within a frequency range 0-500Hz, maximum acceleration of $\pm 3g$, maximum velocity of ± 500 mm/s and maximum displacement ± 125 mm. The table is controlled by four horizontal and four vertical hydraulic actuators. Because the main goal was recording the out-of-plane motion of the façade, this has been instrumented with six wire transducers, measuring absolute displacements (Figure 3.2). Two additional transducers are placed on the foundation. Eight accelerometers are positioned as the same place of the transducers, in order to provide a refined description of the dynamic response as well as to identify the overall dynamic properties of the specimen. Acquisition was carried out with a 100 Hz frequency, through a National Instruments SCXI-1000 control unit.

Selection of the records

Italian records, related to normal faulting events, have been used in the tests. The accelerograms have been selected from a larger set, encompassing a wide range of PGV, Sorrentino *et al.* (2006), based on the results of numerical analyses performed using a one-sided rocking wall model, Sorrentino *et al.* (2008). Because the mechanism is asymmetric, each accelerogram has been considered also with a reversed polarity. The criteria for choice of the signals have been: a not-too-severe response (in order to observe rocking) and a smooth Incremental Dynamic Analysis (IDA) curve. As a result, the four accelerograms of Table 3.1 have been selected. Each record has been applied to the specimen with different scale factors, ranging from 0.22 to 1.13.

Table 3.1. Italian accelerograms selected to perform shake table tests. Data have been collected from SISMA database [<http://151.100.4.92/>]

Earthquake	Year	M_w	Station	Soil type (EC8)	D_f (km)*	Record	PGA (g)	PGV (cm/s)
Irpinia	1980	6.9	Bagnoli Irpino	A	8.0	BagnirWE**	0.167	37.7
Umbria-Marche	1997	6.0	Nocera Umbra	B	4.7	R1168EW	0.438	28.0
Irpinia	1980	6.9	Calitri	B	20.5	CalitWE	0.181	31.7
Irpinia	1980	6.9	Sturmo	B	6.7	SturWE	0.313	70.0

* Distance from the surface projection of the fault, ** Polarity has been inverted

The sequence of tests (records and scale factors) was designed to progressively increase the dynamic response so as to investigate the wall's dynamic reserve of stability, from the activation of motion up to overturning. Therefore, BagnirWE (negative polarity), CalitWE and R1168EW have been

used in the first tests, while SturWE has been used at later stage, because it was expected to induce a more severe response according to the preliminary simulations performed, Al Shawa *et al.* (2011).

Experimental results

On the whole, a set of 34 shake-table tests has been performed (Table 3.2). Up to test 9, the specimen displayed a pronounced out-of-plumb (of about 60 mm) due to the presence of mortar fragments fallen within the cracked joint during repetition of tests. This was reduced in subsequent tests (10-34), by inserting shims in the horizontal cracked joint. The acceleration time-histories recorded on the r.c. foundation have been processed by applying a baseline correction, and a 3rd order Butterworth band-pass filter, within the 0.35-9.00 Hz range. Moreover, a 2nd order band-stop filter proved necessary in the 2.0-2.1 Hz range of frequencies, due to noise introduced by the shake table. In Figure 3.4, pseudo-acceleration response spectra of input accelerograms are compared to response spectra of the signals recorded on the table (A1-A2 in Figure 3.2). The plots have similar shape, although the ordinates corresponding to the accelerations measured on the shake table are lower in the long-period range.

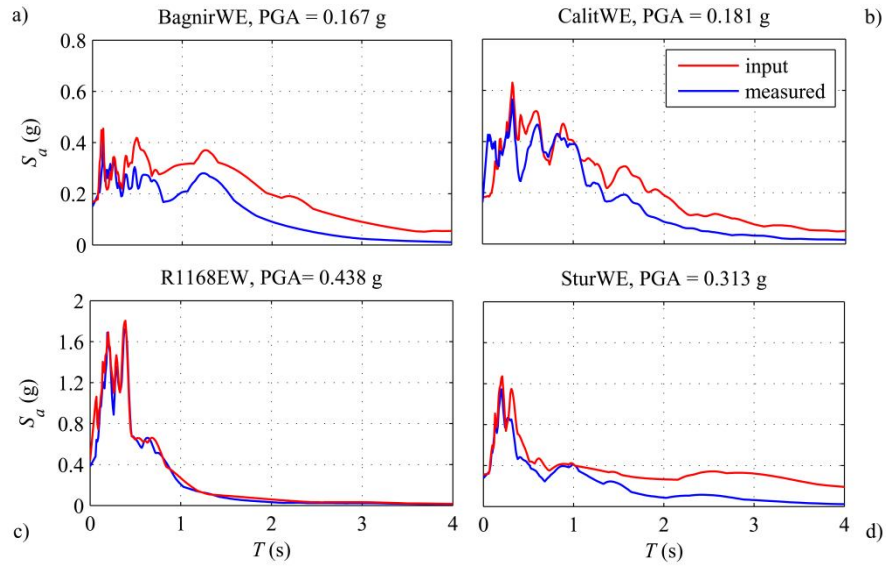


Figure 3.4 Response spectra of signals imposed to the shake table and of accelerograms measured on the specimen's foundation.

Table 3.2. Sequence of tests performed: main properties of the accelerogram recorded at the base of the wall and summary of the results. SF = Scale factor in terms of PGA with respect to the original earthquake (Table 3.1), I_A = Arias Intensity, VSI = Velocity Spectrum Intensity within the range of periods (0-4) s, MIV = Maximum Incremental Velocity, η = initial out-of-plumb recorded, θ = maximum values recorded for the rotation, α = internal angle of the wall (Figure 3.1), f = predominant frequency of the wall's free vibrations measured at the end of the test.

TH	PGA				Intensity Measures				Test results		
	Record	SF	Imposed (g)	Recorded (g)	PGV (cm/s)	I_A -	VSI ₀₋₄ (cm/s)	MIV (cm/s)	η/α (%)	θ/α (%)	f (Hz)
-	-	-	(g)	(g)	(cm/s)	-	(cm/s)	(cm/s)	(%)	(%)	(Hz)
1	BagnirWE	0.24	0.04	0.037	4.7	0.05	25.1	5.1	7.9	27.7	0.7
2	CalitWE	0.22	0.04	0.038	4.2	0.09	29.3	7.5	10.5	29.8	0.6
3	R1168EW	0.91	0.4	0.364	17.2	1.34	66.8	31.6	16.0	44.2	0.6
4	R1168EW	0.09	0.04	0.047	3.5	0.04	16.7	6.1	16.0	54.1	0.6
5	BagnirWE	0.38	0.063	0.057	9.4	0.11	47.3	8.8	16.1	106.5**	0.6
6	BagnirWE	0.38	0.063	0.057	7.9	0.09	40.3	9.6	17.7	117.1**	0.6
7	BagnirWE	0.24	0.04	0.044	4.6	0.08	34.5	6.8	11.8	35.2	0.5
8	CalitWE	0.22	0.04	0.041	5.1	0.13	42.8	9.5	10.3	23.5	0.6
9	BagnirWE	0.38	0.063	0.066	8.9	0.35	43.9	9.7	1.9	11.7	2
10***	BagnirWE	0.50	0.083	0.070	8.7	0.19	56.1	9.9	2.3	17.8	1.8
11	BagnirWE	0.50	0.083	0.091	11.2	0.15	66.0	17.3	2.2	18.8	NA
12	BagnirWE	0.62	0.104	0.090	9.9	0.18	57.4	13.7	2.6	18.2	2
13	BagnirWE	0.75	0.125	0.185	17.2	0.26	94.5	19.9	2.8	22.2	2
14	BagnirWE	0.87	0.146	0.120	18.1	0.29	83.6	17.4	2.9	28.9	2
15	BagnirWE	1.00	0.167	0.151	18.6	0.31	87.7	20.2	3.5	31.0	1.7
16	BagnirWE	1.13	0.188	0.171	22.5	0.39	114.6	22.9	4.1	33.8	1.8
17	CalitWE	0.50	0.09	0.075	7.5	0.30	50.9	11.0	3.9	21.9	1.1
18	CalitWE	0.38	0.068	0.091	7.7	0.21	41.7	9.7	3.7	16.8	1.5
19	CalitWE	0.38	0.068	0.066	6.4	0.19	42.9	10.7	4.7	18.3	1.1
20	CalitWE	0.50	0.09	0.190	10.9	0.34	54.2	15.2	3.9	32.3	1.3
21	R1168EW	0.28	0.123	0.172	5.6	0.11	22.2	8.2	3.5	17.1	1.3
22	R1168EW	0.42	0.185	0.145	9	0.24	34.2	12.0	3.7	34.1	1.1
23	R1168EW	0.56	0.246	0.216	9.9	0.44	35.8	15.3	3.9	51.0	1.7
24	SturWE	0.25	0.078	0.077	4.1	0.08	28.8	6.4	0.7	5.4	2.1
25	SturWE	0.37	0.117	0.113	8.4	0.15	48.8	11.4	4.6	26.3	2.3
26	SturWE	0.50	0.156	0.154	13.1	0.27	67.9	13.7	4.5	41.8	1.7
27	SturWE	0.62	0.195	0.187	13.6	0.40	86.0	15.4	4.5	34.7	0.9
28	SturWE	0.75	0.234	0.233	16.8	0.58	101.2	19.6	4.7	74.0	0.9
29	CalitWE	0.75	0.136	0.128	13.7	0.66	84.2	20.1	5.9	52.5	1.1
30	CalitWE	0.63	0.113	0.207	17.4	0.56	86.6	23.5	5.8	39.8	1.3
31	R1168EW	0.70	0.308	0.309	15.2	0.92	56.3	28.2	5.7	74.1	1.1
32	CalitWE	0.87	0.158	0.311	13.7	0.91	90.7	23.8	6.8	53.8	0.9
33	CalitWE	1.00	0.181	0.298	19.6	1.14	102.7	31.0	7.4	68.2	0.9
34	CalitWE	1.12	0.203	0.232	18.8	1.34	114.7	25.3	8.6	123.5***	0.9

* Figure 3.5

** The wall impacted the retaining structures.

*** Out-of-plumb reduced by means of shims

The results of the tests are synthetically recalled in Table 3.2 in terms of predominant frequency f of the wall's free vibrations, normalised initial out-of-plumb η/α and normalised maximum rotation θ/α , with these parameters depicted in Figure 4.1. More detailed results are presented for tests 16, 27, 31, and 33 in Figure 3.5 and Figure 3.6, in terms of base acceleration and relative displacements of instrumented points.

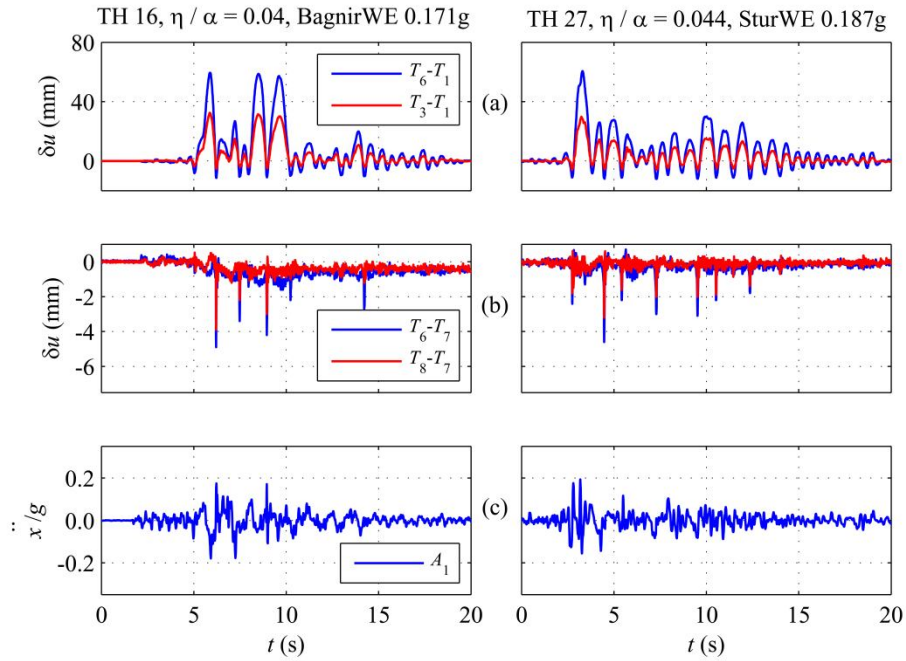


Figure 3.5 Time histories recorded during tests 16, 27. (a) Relative displacement δu measured between wire transducers vertically aligned T6-T1 and T3-T1; b) Relative displacement measured between wire transducers horizontally aligned T6-T7 and T8-T7; c) Acceleration measured on the foundation by accelerometer A1. g = gravity acceleration.

In all experiments, the façade behaves approximately as a rigid body undergoing rocking motion. The time histories of horizontal displacement at different heights (Figure 3.5a, Figure 3.6a) indicate that the façade rocks, with an inward (negative) rotation, limited by the transverse walls, and a more pronounced outward (positive) rotation.

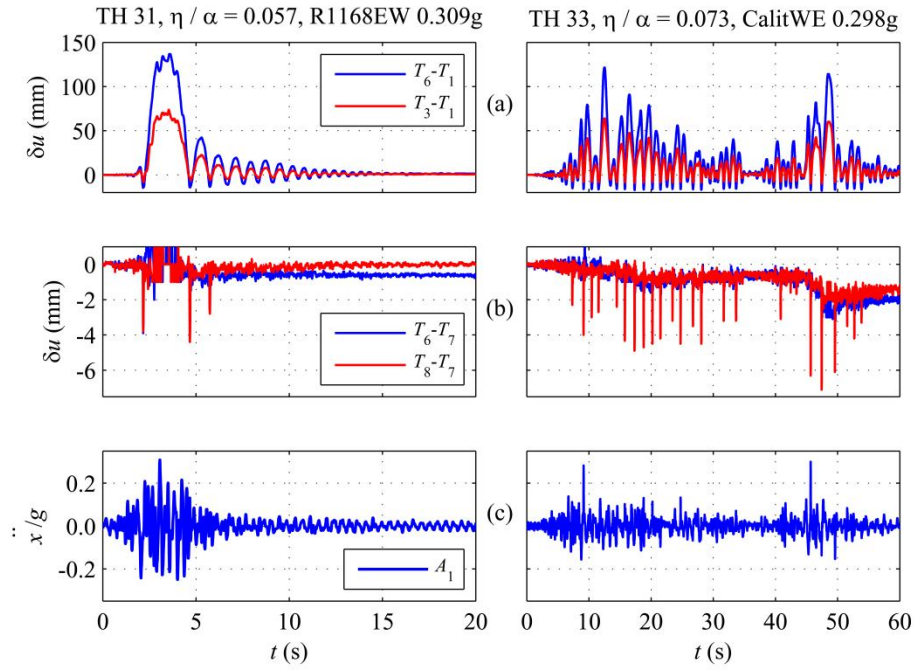


Figure 3.6 Time histories recorded during tests 31 and 33. (a) Relative displacement δu measured between wire transducers T6-T1 and T3-T1; (b) Relative displacement measured between wire transducers T6-T7 and T8-T7; (c) Acceleration measured on concrete foundation by accelerometer A1. g = gravity acceleration.

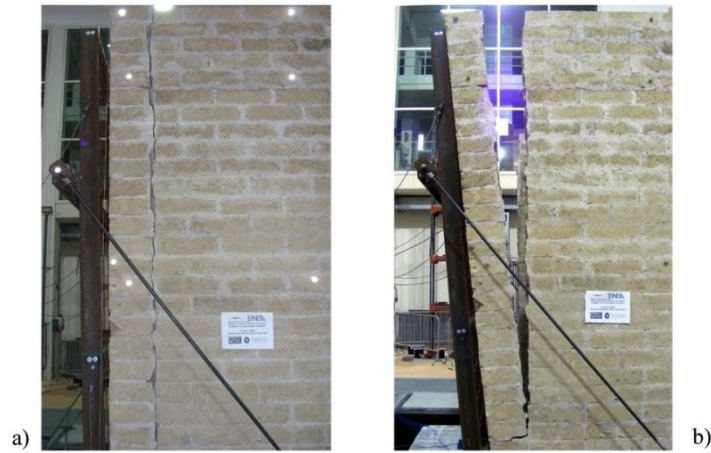


Figure 3.7 View of the specimen at the beginning (a) and at the end (b) of test 34.

The inward rotation takes place thanks to the vertical gap between the façade and the transverse walls, resulting from both the out-of-plumb of the façade and the void caused by the debonding of the mortar in vertical joints. In addition to the primary rocking motion, a negligible sliding motion takes place on the horizontal crack plane and induces a cumulative slip of a few millimetres at the end of the test series.

Dynamic modelling of a masonry wall rocking on an inclined foundation

In order to reproduce the experimental out-of-plane dynamic behaviour observed during the tests, a modelling strategies based on the Distinct Element Method (DEM) is presented, by taking advantage of the intrinsic discrete character of the specimen, consisting of a façade separated from the transverse walls. The cited method, originally proposed by Cundall (1971), is the most common tool to analyse the behaviour of rock masses and assemblages of blocks. The method is particularly suitable for problems in which the dynamic of the system is mainly governed by relative motion and by creation and loss of contacts between adjacent blocks. Because of these features, DEM has been widely applied in the literature for studying the dynamics of rocking motion induced by earthquakes on block structures, Azevedo *et al.* (2000), Papantonopoulos *et al.* (2002), Peña *et al.* (2007).

The program UDEC, Itasca (2003), is adopted for the numerical simulations. The specimen described in the previous section is represented by a plane model consisting of two rigid bodies as depicted in Figure 4.7. One body represents the portion of the façade that experienced the rocking motion during the tests. The other body consists of the remaining part of the specimen together with the foundation, which is assumed to move rigidly under ground motion. In order to reproduce the actual configuration of the specimen during each test, a gap d at the vertical interface is considered, accounting for the space left by the mortar fallen during test repetition. Moreover, an initial out-of-plumb is introduced by tilting the horizontal interface by an angle η . Within the horizontal and vertical joints, separating the two bodies, two sets of contact points, which obey a Mohr-Coulomb yield criterion, are evenly distributed. Due to existing cracks, the joints have zero tensile strength, no cohesion, no dilatancy, while the friction angle was set high enough to avoid excessive sliding. In the elastic range the behaviour of the joints is governed by normal and tangential stiffnesses, denoted as k_n and k_t , respectively, with $k_t = 0.4k_n$, corresponding to a mortar

Poisson ratio equal to 0.25. Moreover, because the bed joint is 3.3 m long, while the two head joints are 0.25 m deep, the stiffness of the vertical contacts is 15% that of the bed contacts.

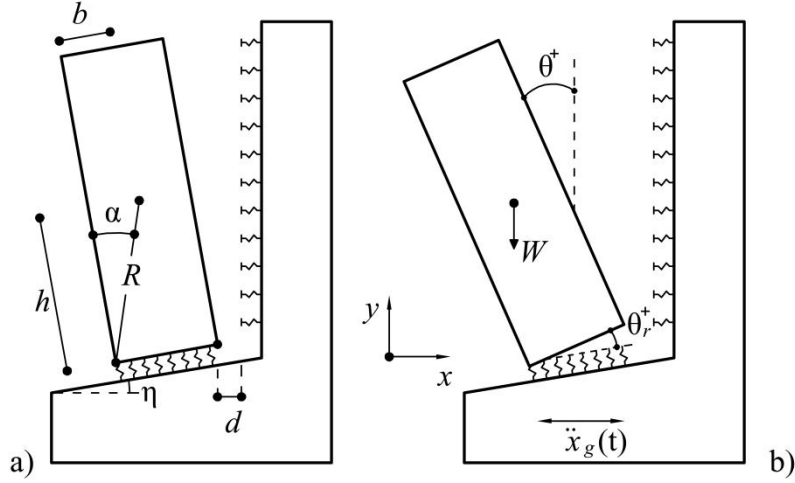


Figure 3.8 Distinct element model of masonry specimen. (a) Configuration before each test: initial out-of-plumb η and gap d related to mortar vertical joint. (b) Kinematic descriptors of the motion: out-of-plane rotation of the façade wall measured with respect to the vertical (θ) and to the tilted foundation (θ_r).

In order to investigate the effects of the interface properties, which may dramatically influence the dynamic response as shown in El Gawady *et al.* (2011), a sensitivity analysis has been performed on the number n of contact points, the normal stiffness k_n and the initial out-of-plumb η . The results, in terms of moment–rotation curves, obtained by varying the number of contacts of the bed interface from 2 to 15 are plotted together with the analytical curves of a rigid and Winkler-type foundations (Figure 3.9a).

The expressions for the Winkler foundation are derived following the approach in Blasi and Spinelli (1986):

$$M_R = W R \cdot \sin[\alpha - (\theta_r + \eta)] - W b \cos \eta + \frac{2}{3} k_n b^3 \theta_r \quad \theta_r \leq \theta_{r,cr} \quad (3.1)$$

$$M_R = W R \cdot \sin[\alpha - (\theta_r + \eta)] - \frac{1}{6} k_n \theta_r \sqrt{\left[\frac{2 W \cdot \cos \eta}{k_n \cdot \theta_r} \right]^3} \quad \theta_r \geq \theta_{r,cr} \quad (3.2)$$

$$\theta_{r,cr} = \frac{W \cdot \cos \eta}{2b^2 k_n} \quad (3.3)$$

where M_R is the restoring moment, W the self-weight of the façade, R the distance of the centroid from the corner of the base, $\theta_r = \theta - \eta$ the relative rotation with respect to the tilted foundation (Figure 3.8), and $\theta_{r,cr}$ is the relative rotation corresponding to lift-off of the block, *i.e.* when the contact is lost in one of the corners of the base.

The response curve obtained for $n=2$ is close to the rigid foundation case, except for the initial elastic response (Figure 3.9a). As the number of contacts increases, the response of the interface gets closer to that of a Winkler-type foundation: the initial stiffness, the peak load and the ultimate rotation tend to decrease and a smoother transition is found from the initial elastic phase towards the softening branch. A two-contacts scheme proved suitable for reproducing the rocking motion of granite blocks Peña *et al.* (2007) and may be calibrated for reproducing the time-varying response of a Winkler type foundation Psycharis and Jennings (1983). However, the proposed equivalence is amplitude dependent and the model is unable to reproduce the smooth moment-rotation relationship of a masonry mortar joint, as the one obtained experimentally in Doherty *et al.* (2002). Therefore, in the following, 15 contact points are used, both in bed and head joints, which provide a reasonable approximation of the limit case $n=\infty$ corresponding to the Winkler foundation (a). In Figure 3.9b the response curves obtained by varying the stiffness of the contacts at the base of the block are plotted against the frequency f_0 , related to small-amplitude rocking motion and evaluated on the initial branch of the curves, *i.e.* up to 50 % of the peak restoring moment. The larger the stiffness, the larger are the peak strength and the ultimate rotation. For $k_n=135$ GPa, the behaviour is that of a block on a rigid foundation, while a value of 1.35 GPa is necessary to obtain an initial frequency close to those measured during the tests (1-2 Hz). Bearing in mind the depth of the joint, such stiffness is approximately 1/5 of the elastic modulus of uncracked mortar. Finally, sensitivity analyses on the initial out-of-plumb in the range $\eta/\alpha=0.04-0.08$ have shown a negligible effect on maximum restoring moment and ultimate rotation.

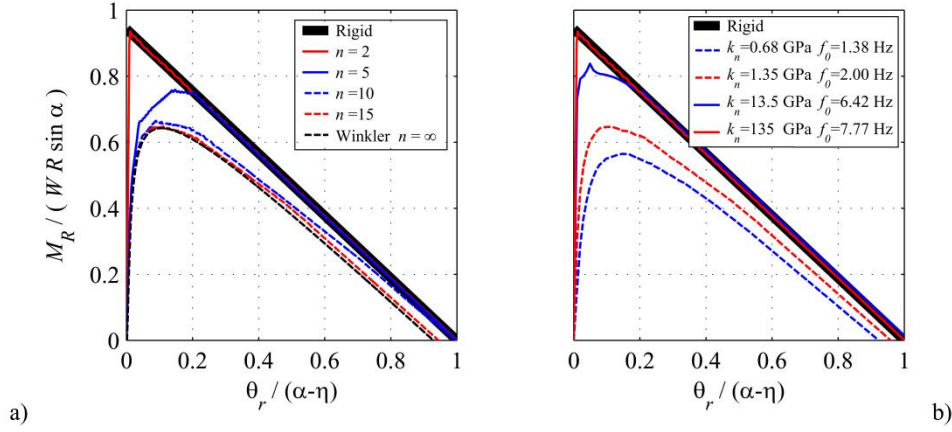


Figure 3.9 Normalized response curves in terms of restoring moment (M_R)- rotation (θ_r) relationships, varying: (a) number n of contacts, and (b) normal stiffness k_n . f_0 denotes the frequency of small amplitude rocking motion.

Dynamic analyses have been performed in two subsequent steps. First gravity is applied and the system is allowed to evolve until convergence is achieved. Then the ground velocity experimented by the base of the specimen is assigned to the block consisting of the transverse wall and the foundation. The equations of motion are integrated explicitly in the time domain, and the contacts that are made or lost during the analysis are automatically recognised, Itasca (2003). The energy loss that takes place during the motion results from slippage and a stiffness-proportional viscous damping; a mass-proportional damping is neglected, because it may over-damp the response of the block, Papantonopoulos *et al.* (2002). Accordingly, the damping is described by the ratio ξ at the frequency $f_c = p / (2\pi)$ (Peña *et al.* (2007), de Felice (2011)), where $p = \sqrt{3g/(4R)}$ is the frequency parameter of an homogeneous and parallelepiped rocking block Housner (1963). The value of ξ has been calibrated in order to obtain the best fit of the experimental results.

In order to measure the differences between numerical, $\theta_{\text{num}}(t)$, and experimental, $\theta_{\text{exp}}(t)$, time histories, two error estimators have been used. The first, RMS^* , is based on the Root Mean Square evaluated as:

$$\text{RMS}^* = \frac{|\text{RMS}_{\text{exp}} - \text{RMS}_{\text{num}}|}{|\text{RMS}_{\text{exp}}|} \quad (3.4)$$

The second estimator is the Weighted Mean Error, WME, computed as follows:

- The numerical signal is time-shifted by a lag Δt ranging within a ± 0.5 s interval;
- A threshold is introduced so that only values higher then 20% of the maximum rotation (experimental or numerical, whichever is largest) are considered. Such a threshold is useful to avoid numerical divergences related to small-amplitude oscillations and to estimate the accuracy of the model in predicting the large-amplitude oscillations, which are of practical interest for seismic vulnerability assessment;
- The WME is finally defined as the minimum value of the error evaluated over the interval of lag Δt under consideration:

$$\text{WME} = \min_{\Delta t \in [-0.5; +0.5]} \frac{\int_0^T |\theta_{\text{exp}}(t) - \theta_{\text{num}}(t + \Delta t)| dt}{\int_0^T |\theta_{\text{exp}}(t)| dt} \quad (3.5)$$

In Figure 3.10a comparison between the experimental and numerical time histories is plotted. The model is able to reproduce reasonably the dynamic response for different initial configurations and under different ground motions. The value of the damping ratio ξ fitting the tests is found to increase, from $0.025 \tan \alpha$ to $0.10 \tan \alpha$, with α defined in Figure 3.8. The increase in damping seems related to the accumulation of damage during test repetitions. For the purpose of estimating the sensitivity of the simulations to joint stiffness and damping ratio, a parametric analysis has been performed. The results are plotted in Figure 3.11 as greyscale error maps in terms of RMS* and WME. It is possible to identify different combinations (k_n, ξ) that allow reproducing the experimental time histories reasonably well ($\text{RMS}^* < 0.3$, $\text{WME} < 0.7$). It is worth noting the presence of a region, at the bottom of the maps, where the system is under-damped and is likely to overturn.

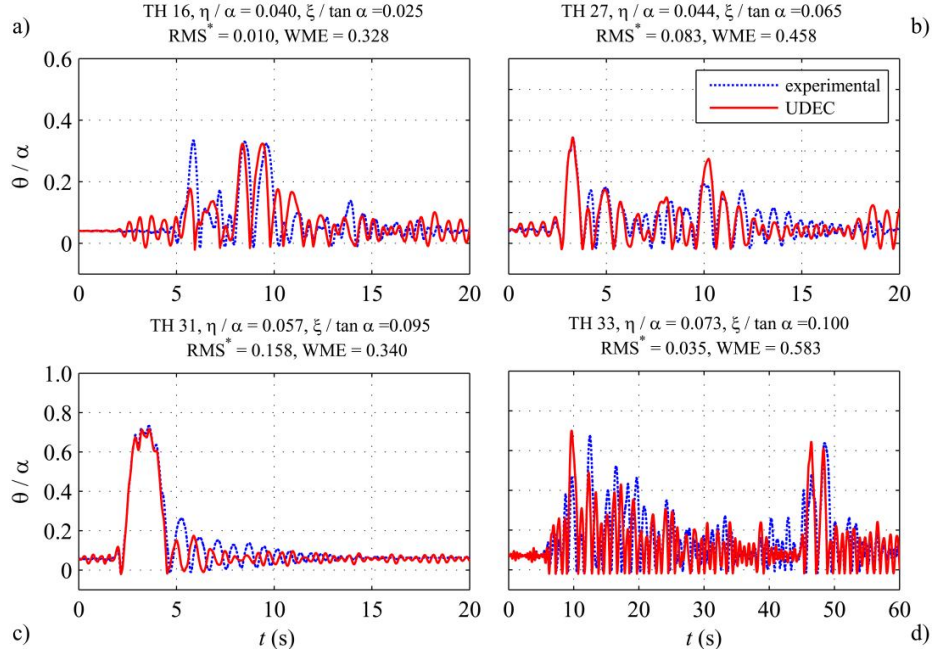


Figure 3.10 Comparison between experimental and numerical time histories. $d=4$ mm;
 $n=15$, $k_n = 1.35$ GPa, $k_t = 0.4 k_n$, $f_c = p / (2\pi)$.

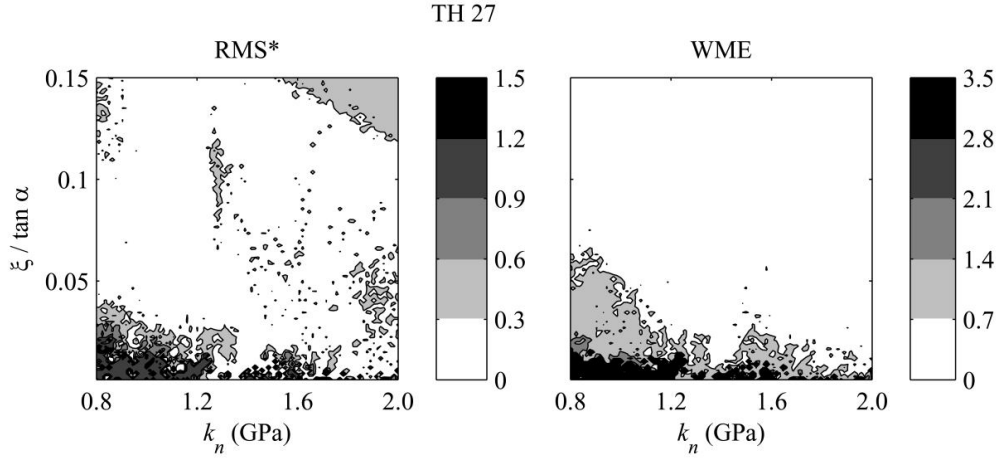


Figure 3.11 Parametric analysis with respect to the damping ratio (ξ) and the stiffness (k_n) of the bed joint: synthetic comparison between numerical and experimental time histories for test 27, in terms of RMS* and WME (Eqs.3.4 -3.5).

Comparison between experimental and numerical results

A direct comparison between experiments and numerical simulations has been carried out in terms of maximum rotations. For each test, UDEC numerical results have been obtained computing the mean $\bar{\theta}_{DEM,max}$ of the maximum rotation over twenty responses when varying the damping ratio ξ in the range $0.02 \tan \alpha - 0.1 \tan \alpha$. A reasonable agreement, taking into consideration the usual scatter in these measurements, between numerical and experimental results is obtained, as shown in Figure 3.12.

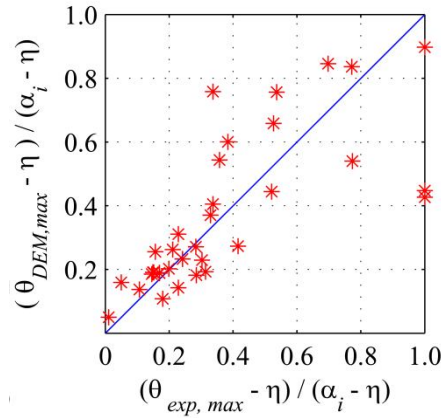


Figure 3.12 Comparison between experimental and DEM numerical results in terms of normalized maximum rotation assuming $d = 4$ mm; $n = 15$, $k_n = 1.35$ GPa, $k_t = 0.4 k_n$, $f_c = p / (2 \pi)$.

Comparison with code assessment procedures

In order to compare the experimental results to the Italian code's equivalent static procedure CSLLPP (2009), normalised maximum rotations are plotted against code demand/ capacity ratios. The code suggests two possible assessment procedures: 1) strength-based, 2) displacement-based. In order to apply these procedures, let us refer to a simple representation of the wall consisting in a monolithic block resting on a rigid foundation as depicted in Figure 3.13. The base of the block is reduced so as to obtain an equivalence between the latter model and the DEM model in terms of ultimate rotation

capacity. To this purpose $b_i = 0.94 b$. Standing these considerations, the acceleration capacity defined by strength-based procedure writes:

$$a_0^* = \frac{\lambda_0 g}{e^* CF} \quad (3.6)$$

with $\lambda_0 = \tan(\alpha_i - \eta)$ static collapse load multiplier of the mechanism at rest (Figure 3.13), g gravity acceleration, e^* fraction of participating mass, CF confidence factor. In the case at hand $e^* = 1.0$, while it has been assumed $CF = 1.0$. The corresponding acceleration demand, for a mechanism located on the foundation, is equal to the expected peak acceleration divided by a behaviour factor $q = 2.0$.

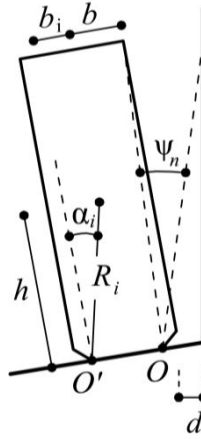


Figure 3.13 Rigid-block model adopted for evaluating the response according to code procedures, CSLPP (2009).

Experimental and code demand/capacity ratios are presented in Figure 3.14a. In both the approaches here considered, the demand has been derived from the acceleration measured on the foundation of the wall. It is possible to observe that, with just two exceptions, both referred to marked out-of-plumb, the code procedure is conservative, *i.e.* points are well below the $\pi / 4$ line.

The displacement-based procedure defines a displacement capacity d_u^* , which for the wall under consideration (Figure 3.13), is equal to 40% of the collapse displacement of the centre of mass:

$$d_u^* = 0.4 R_i \sin(\alpha_i - \eta) \quad (3.7)$$

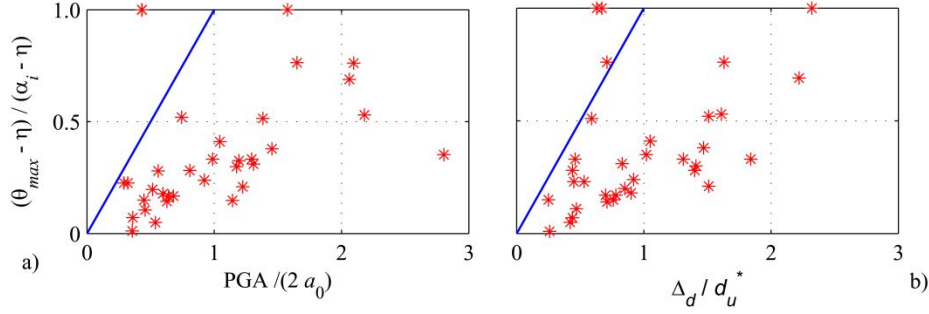


Figure 3.14 Comparison between experimental and code demand / capacity ratios. (a): strength-based, linear, and (b): displacement-based, nonlinear, code procedures, CSLPP (2009).

The corresponding displacement demand Δ_d , for a mechanism located on the foundation, is equal to the spectral displacement $S_{De}(T_s)$ evaluated for the secant period (T_s) of the local mechanism:

$$T_s = 2\pi \sqrt{\frac{d_s^*}{a_s^*}} \quad (3.8)$$

with $d_s^* = 0.4 d_u^*$, and a_s^* acceleration of the bilinear response curve for $d^* = d_s^*$. In the case examined here, accounting for the indented rocking hinge, the secant period is:

$$T_s \cong 2\pi \sqrt{\frac{0.19 R_i \cos(\alpha_i - \eta)}{g}} \quad (3.9)$$

Such a definition has a conventional meaning, because it is well known that in such oscillators the period is amplitude-dependent, Housner (1963), CSLPP (2009).

The comparison between experimental and code demand/capacity ratios is presented in Figure 3.14b. It is possible to observe that only in three cases, out of 34, the code is unconservative. The mean value of the experimental/code ratios is 42%, which is very close to the coefficient applied by the code to define the displacement capacity d_u^* . Thus, the code procedure seems able to capture, on average, the behaviour observed in the tests. The choice of the 40% threshold remains debatable; however, given the scattered behaviour of out-of-plane loaded walls, it is probably careful to guarantee an adequate safe margin. Such comparison is the result of conventional assumptions, with regard to both the

period of the mechanism and the acceleration-displacement relationship. If the three-branches relationship previously defined, Sorrentino *et al.* (2008), is used, the plots do not change markedly. As expected, the strength-based procedure becomes more restrictive, because the acceleration capacity is noticeably reduced. On the contrary, the displacement-based procedure is much less affected, because the displacement capacity is weakly influenced by the change of the moment-rotation relationship. Therefore, the use of the refined three-branches moment-rotation relationship does not seem to improve significantly the equivalent static procedure assessment methods.

With a view to extending the comparison to walls with different geometries, additional time histories have been generated by means of the non linear dynamic model previously presented. Four walls, having (b, h) (Figure 3.8, Figure 3.14) = (0.125, 1.5), (0.20, 3.0), (0.25, 3.0), (0.375, 3.0) have been considered. The same four accelerograms of Table 3.1, whose amplitudes have been scaled with ten coefficients varying between 0.2 and 2.0, have been used together with 12 spectrum-compatible accelerograms artificially generated as addressed next. For each signal three horizontal elastic response spectra have been derived according to EuroCode 8 and considering the ground type of the record and different design peak ground accelerations (0.15, 0.25, 0.35 g). Then, the original records have been scaled in order to match the corresponding spectra within the 0.8- 1.8 s range of periods, containing the secant periods of the four walls considered. Both positive and negative polarities have been considered. On the whole 416 numerical analyses have been performed. In order to follow up the comparison with the code even when overturning occurs, the demand/capacity ratio, provided by numerical analyses, has been evaluated as addressed next. The capacity E_C is defined as the maximum variation of the potential energy of the block ΔE_p , reached for $\theta = \alpha_i$.

$$E_C = \Delta E_p(\theta = \alpha_i) = WR_i(1 - \cos \alpha_i) \quad (3.10)$$

The demand E_D is evaluated as the maximum potential energy ΔE_p recorded during the motion when $\theta_{\max} < \alpha$:

$$E_D = \Delta E_p(\theta = \theta_{\max}) = WR_i(1 - \cos \theta_{\max}) \quad (3.11)$$

or otherwise as the sum of potential ΔE_p and kinetic energies E_c evaluated at $\theta = \alpha_i$:

$$E_D = \Delta E_p(\theta = \alpha_i) + E_c(\theta = \alpha_i) \quad (3.12)$$

Finally the demand/capacity ratios expressed in terms of kinetic and potential energies, writes:

$$\begin{aligned} \frac{E_D}{E_C} &= \frac{1 - \cos \theta_{\max}}{1 - \cos \alpha_i} & \theta_{\max} \leq \alpha_i \\ \frac{E_D}{E_C} &= 1 + \frac{\sin \alpha_i (b^2 + 3b_i^2 + 4h^2)}{6gb_i(1 - \cos \alpha_i)} \dot{\theta}^2(\theta = \alpha_i) & \theta_{\max} \geq \alpha_i \end{aligned} \quad (3.13)$$

It is worth noting that, in a linearised kinematic framework, when no overturning takes place, the ratio $E_D/E_C = \theta_{\max}/\alpha$.

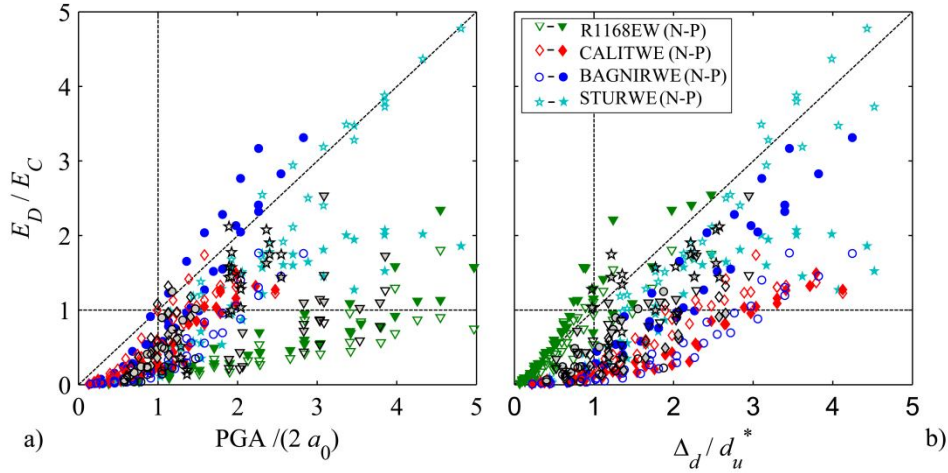


Figure 3.15 Comparison between non linear dynamic and code (CSLLPP 2009) demand / capacity ratios. (a): strength-based, and (b): displacement-based code procedures adopting the DEM model. Empty (solid) marker is referred to Negative (Positive) polarity; coloured (grayscale) marker is referred to natural (artificial) accelerograms.

When neglecting the results in which both, numerical analyses and code estimates, give demand/capacity ratio greater than one, the strength-based procedure is conservative in 99% of cases and the displacement-based procedure is conservative in 82% of cases.

The scatter between non-linear dynamic results and code estimates, in terms of Coefficient of Determination, is equal to 0.38 and 0.49 for strength- and displacement-based approaches, respectively. The larger scatter of strength-based approach justifies the larger safety margin; as a matter of fact, by using a behaviour factor q of about 4, the strength base approach is still conservative in

70% of cases, Figure 3.16.

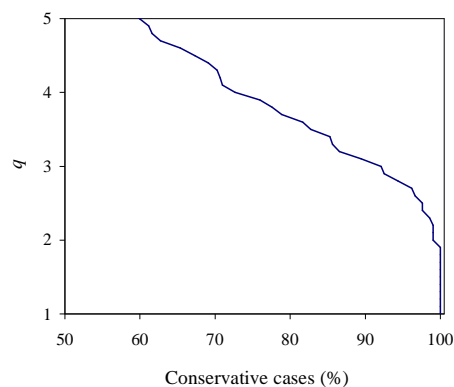


Figure 3.16 Behaviour factor q versus the percentage of conservative cases evaluated by means of numerical analyses.

The two code procedures may yield very different results, depending on ground motion characteristics; for instance, a record such as R1168EW with a large PGA but very small spectral displacements, gives a conservative estimate in the strength-based approach while it leads to a rather unconservative estimate in the displacement-based approach. Due to the asymmetry of the collapse mechanism, the response to the same accelerogram, with reversed polarity, is usually different, as in the case of BagnirWE record. Such behaviour escapes static procedures.

4. A homogenization approach for the in-plane analysis of masonry in the linear elastic range

A macroscopic constitutive description of masonry may be achieved by means of experimental campaigns, which usually are costly due to the large size of the specimens and required testing equipment. An alternative and less expensive approach is to measure the individual properties of unit and mortar on small samples and, then, to use a theoretical model that combines the information from the components and makes it possible to obtain the overall properties of the assemblage. When the arrangement of the unit within the brickwork may be regarded to as periodic, the latter issue may be tackled in the literature by resorting to the homogenization theory of periodic media, Suquet (1987).

Referring to in-plane loaded masonry in the elastic range, the problem has been solved by resorting to the finite element method, Anthoine (1995). Nevertheless, the derivation of closed form expressions for the compliance matrix of masonry has always been attractive and different attempts have been made in the literature by introducing assumptions which make it possible to handle the problem analytically. The simplified homogenization techniques proposed so far rely on:

- simplification assumptions concerning the mortar joints;
- the Voigt kinematics hypothesis, *i.e.* uniform strain within the mortar and brick phases;
- plane stress assumption at a microscopic level.

For instance, by neglecting the presence of the head joint, masonry may be regarded as a stratified material, Carbone and Codegone (2005). The head joint may be introduced in a second step by following the so called two step homogenization approach proposed by Pande *et al.* (1989). Alternatively, the whole set of joints may be accounted for in one step by treating them as zero-thickness interfaces, Cecchi and Sab (2002a), de Felice (1995, 2001). These simplifications are thought to introduce some errors in predicting the properties of the equivalent homogeneous continuum, Lourenço and Rots (1997b). Moreover, the simplified techniques fail in reproducing the microscopic stresses arising within the phases either depending on the bond pattern, which is

neglected in multi-step approaches, or related to the Poisson interaction between mortar and brick, which is not accounted for when joints are treated as interfaces. Additionally, the plain stress assumption is in disagreement with the exact three-dimensional solution, as showed by Anthoine (1995). All this arguments suggest that the extension of the abovementioned models to the non-linear range may leads to erroneous estimation of the mechanical behaviour of masonry. Some of the limits of previous formulations may be overcome following an “engineering” approach by introducing simplified deformations mechanisms over the basic cell, Lopez *et al.* (1999), Zucchini and Lourenço (2002).

Referring to the case of masonry walls in-plane loaded, a novel approach is followed in the present chapter, which gets rid of ad-hoc engineering assumptions and applies rigorously the homogenization theory of periodic medium in one step considering three-dimensional effects, the actual thickness and the whole set of mortar joints. In the first part the boundary value problem attached to the Representative Volume Element (RVE) is formulated. A linear elastic behaviour is assumed for the constituents, *i.e.* mortar and brick, and the problem is formulated by introducing a simplified kinematics for the RVE: the hypothesis of piece-wise constant strain field allows us to handle the localization problem analytically and to derive the elasticity tensor of masonry as a function of mortar and brick geometrical and mechanical properties. Furthermore, relevance is given to the tensors of strain and stress localization which make it possible to derive the microscopic fields for a given macroscopic load. The results obtained are compared with the analytical formulations available in literature, with the results of finite element analyses and with experimental data collected in the literature. Eventually, the proposed scheme is applied to provide an estimate of the limit elastic domain of masonry under in-plane loads which is compared with experimental data, Page (1981,1983), in terms of both failure surface and triggering failure mode.

Formulation of the localization problem

Let us consider as a domain of reference Ω the single leaf masonry wall depicted in Figure 4.1a, consisting of bricks, with dimensions h_b and l_b , arranged regularly so as to reproduce a running bond pattern, and of two families of orthogonal mortar joints. The bed joints, which are laid horizontally with a thickness of t_m , separate adjacent courses of brick and span the whole brickwork without interruptions; the head joints, which are laid vertically with a thickness of t_h , separate contiguous bricks on the header faces and are staggered between adjacent courses; the cross joints are located at the intersection between bed joints and head joints.

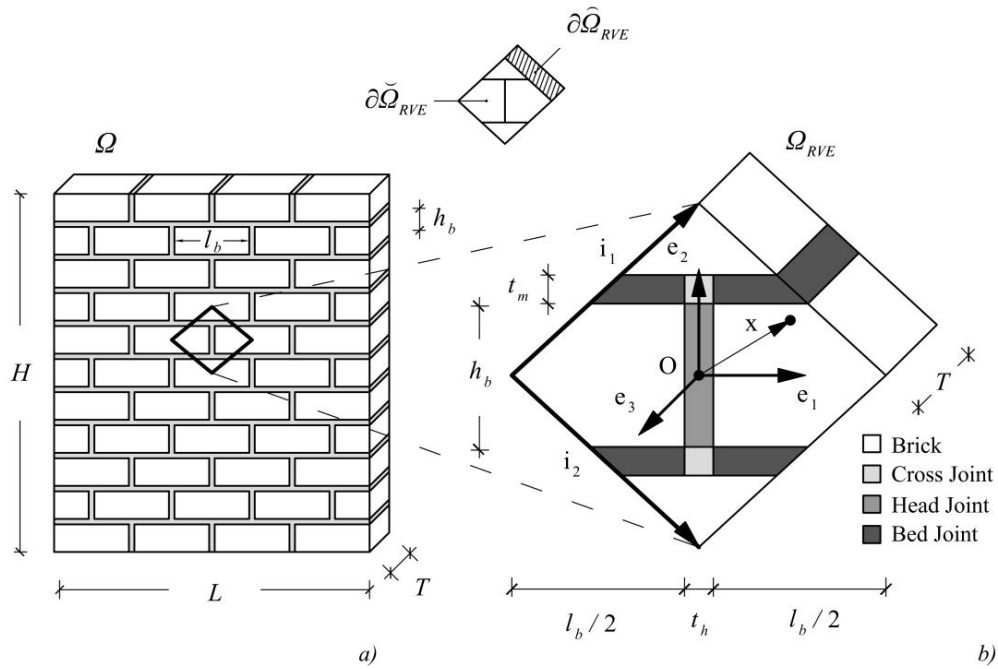


Figure 4.1 Domain of reference Ω (a) and corresponding representative volume element Ω_{RVE} (b).

The whole domain Ω can be reproduced by repetition along the directions of periodicity of a representative volume element, Ω_{RVE} , identified as the lozenge with vertex located in the centre of four adjacent bricks and extruded throughout the whole thickness T of the wall. With respect to the system of reference $Oe_1e_2e_3$ depicted in Figure 4.1b, the pattern of the domain proves

periodic only in the Oe_1e_2 plane. Thus two directions of periodicity i_1 and i_2 are found, expressed as:

$$i_1 = \frac{(l_b + t_h)}{2} e_1 + (h_b + t_m) e_2 \quad ; \quad i_2 = \frac{(l_b + t_h)}{2} e_1 - (h_b + t_m) e_2 \quad (4.1)$$

The boundary of Ω_{RVE} may be divided into two different regions, $\partial\Omega_{RVE} = \partial\bar{\Omega}_{RVE} \cup \partial\Omega_{RVE}$ (Figure 4.1): the former ($\partial\bar{\Omega}_{RVE}$), which is internal to the wall and separates adjacent RVEs, can be divided into pairs of opposite sides, *i.e.* that correspond by periodicity; the latter region ($\partial\Omega_{RVE}$) consists of the boundary of the RVE that lies on the two external faces of the wall which, unlike the previous case, can not be referred to as opposite sides.

Since the brick-laying process does not ensure that the vertical joints are perfectly filled with mortar, it may be convenient to characterize bed joints separately from cross joints and head joints. For this purpose Ω_{RVE} has been divided into 11 sub-domains Ω^i , as reported in Figure 4.2: hence the regions that pertain to the brick have index i ranging from 1 to 4, whereas the sub-domains pertaining to mortar joints have index i ranging from 5 to 8 for the bed joints, equal to 9 for the head joint and ranging from 10 to 11 for the cross joints.

Brick and mortar are assumed to be elastic so that for a given point $x \in \Omega_{RVE}$ the stress $\sigma(x)$ and strain $\varepsilon(x)$ are related by means of the following constitutive relationship:

$$\sigma(x) = C(x) : \varepsilon(x) \quad \text{with} \quad C(x) = \begin{cases} C^b & \forall x \in \Omega^i \quad i = 1, \dots, 4 \\ C^m & \forall x \in \Omega^i \quad i = 5, \dots, 8 \\ C^h & \forall x \in \Omega^i \quad i = 9, \dots, 11 \end{cases} \quad (4.2)$$

where C^b and C^m are fourth order tensor representing the elasticity tensors of brick and bed joints, respectively, while C^h is the elasticity tensor assumed for both head joints and cross joints. It is worth noting that each component may be characterized separately provided that the resulting function $C(x)$ is periodic on opposite sides of $\partial\bar{\Omega}_{RVE}$. Moreover, no hypotheses are made concerning the level of anisotropy of each component, leaving the possibility to assume either an isotropic or orthotropic behaviour for the bricks in order to take into account for the presence of holes or other.

When the dimensions of the brick are small compared with those of the domain Ω , it is convenient to describe masonry as an equivalent homogeneous continuum; hence, microscopic stress $\sigma(x)$ and strain $\varepsilon(x)$, which act on each constituent, are not accounted directly and relevance is given to macroscopic

stress Σ and strain E , which act on the composite material as a whole and read:

$$\Sigma = \langle \sigma(x) \rangle = \frac{1}{\Omega_{RVE}} \int_{\Omega_{RVE}} \sigma(x) d\Omega \quad (4.3)$$

$$E = \langle \varepsilon(x) \rangle = \frac{1}{\Omega_{RVE}} \int_{\Omega_{RVE}} \varepsilon(x) d\Omega \quad (4.4)$$

where $\langle \bullet \rangle$ denotes the average operator over the representative volume element. The latter assumption introduces an important simplification in modelling masonry, since bricks and mortar joints should no longer be explicitly reproduced within the domain Ω . The constitutive identification of the equivalent homogeneous medium, *i.e.* Σ – E relationship, may be derived by resorting to the homogenization theory, Suquet (1987), by solving a boundary value problem that is attached to Ω_{RVE} , also called localization problem.

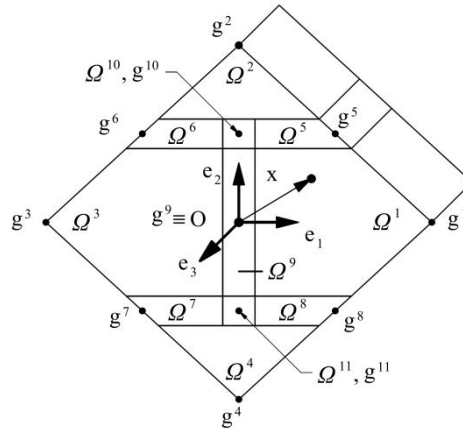


Figure 4.2 Division of Ω_{RVE} in brick (Ω^i with $i=1,\dots,4$) and mortar (Ω^i with $i=5,\dots,11$) sub-domains, together with the respective centres g^i .

In the present work, in order to define the overall in-plane properties of masonry assemblage, the abovementioned problem is stated referring to the case in which the lateral faces of the wall are stress-free and the macroscopic loads act only along the Oe_1e_2 plane so as to maintain the symmetry with respect to the middle plane of the domain. From the macroscopic point of view the latter conditions correspond to a plane stress statement of the problem in which the following components of tensor Σ vanish:

$$\Sigma_{13} = \Sigma_{23} = \Sigma_{33} = 0 \quad (4.5)$$

The respective macroscopic strain, on the contrary, is a three-dimensional field in which the components E_{13} and E_{23} vanish, owing to the symmetry of the problem, while the component E_{33} assumes a finite value. It should be noted that the local strain $\sigma(\mathbf{x})$ and stress $\varepsilon(\mathbf{x})$ are fully three-dimensional fields and that the plane stress condition at macroscopic level only implies, by virtue of Eqs. (4.3)-(4.4), that the averages of the out-of-plane component are zero:

$$\langle \varepsilon_{1,3} \rangle = \langle \varepsilon_{2,3} \rangle = \langle \sigma_{1,3} \rangle = \langle \sigma_{2,3} \rangle = \langle \sigma_{3,3} \rangle = 0 \quad (4.6)$$

Given the consideration made above, the localization problem, attached to Ω_{RVE} and related to the in-plane behaviour of the homogeneous material, reads:

$$\text{div } \sigma(\mathbf{x}) = 0 \quad (4.7)$$

$$\sigma(\mathbf{x}) \cdot \mathbf{n} \quad \text{anti-periodic on opposite sides of } \partial\hat{\Omega}_{\text{RVE}} \quad (4.8)$$

$$\sigma(\mathbf{x}) \cdot \mathbf{n} = 0 \quad \text{on } \partial\check{\Omega}_{\text{RVE}} \quad (4.9)$$

$$\sigma(\mathbf{x}) = \mathbf{C}(\mathbf{x}) : \varepsilon(\mathbf{x}) \quad (4.10)$$

$$\varepsilon(\mathbf{x}) = \text{sym } \nabla \mathbf{u}(\mathbf{x}) \quad (4.11)$$

$$\mathbf{u}(\mathbf{x}) = \mathbf{E} \cdot \mathbf{x} + \hat{\mathbf{u}}(\mathbf{x}) \quad (4.12)$$

$$\hat{\mathbf{u}}(\mathbf{x}) \quad \text{periodic on opposite sides of } \partial\hat{\Omega}_{\text{RVE}} \quad (4.13)$$

where $\mathbf{u}(\mathbf{x})$ and $\hat{\mathbf{u}}(\mathbf{x})$ are local displacement fields defined on Ω_{RVE} . The problem can be solved by means of a strain controlled loading by imposing the components E_{ij} with $i, j=1, 2$ of the macroscopic strain. Noteworthy, according to the macroscopic plane stress assumption, the normal out-of-plane strain E_{33} is workless and therefore the solution of the localization problem does not depend on the latter component, the value of which can be evaluated *a posteriori* as the average over Ω_{RVE} of the microscopic strain $\varepsilon_{33}(\mathbf{x})$, Eq. (4.4).

The localization problem may be stated in a weak form by introducing suitable test fields $\hat{\mathbf{u}}^{\text{test}}(\mathbf{x})$, Suquet (1987):

$$\int_{\Omega_{RVE}} \sigma(x) \cdot \nabla \hat{u}^{test}(x) \, d\Omega = 0 \quad \forall \hat{u}^{test}(x) \in \mathbf{V}_{per} \quad (4.14)$$

$$\mathbf{V}_{per} = \left\{ \hat{u}(x) \in \mathbf{H}^1(\Omega_{RVE}) \mid \begin{array}{l} \hat{u}(x) \text{ is periodic on } \partial\hat{\Omega}_{RVE} \\ \langle \hat{u}(x) \rangle = 0 \end{array} \right\}$$

where \mathbf{V}_{per} and $\mathbf{H}^1(\Omega_{RVE})$ denote the space of periodic and fluctuating displacement fields and a Sobolev space defined over Ω_{RVE} , respectively. By introducing the constitutive relations of mortar and brick, Eq. (4.3), the resolution of the localization problem amounts to find the admissible displacement field $\hat{u}(x) \in \mathbf{V}_{per}$ fulfilling the following relation:

$$\int_{\Omega_{RVE}} \mathbf{C}(x) : [\mathbf{E} + \nabla \hat{u}] : \nabla \hat{u}^{test}(x) \, d\Omega = 0 \quad \forall \hat{u}^{test}(x) \in \mathbf{V}_{per} \quad (4.15)$$

A simplified kinematics for the Representative Volume Element

In order to obtain an analytical solution of the localization problem, Eq. (4.15), simplifying assumptions are made concerning the kinematics within the representative volume element. Let us assume that the fluctuating part $\hat{u}(x)$ of the displacement field can be approximated by a piecewise function belonging to \mathbf{H}^1 as addressed next. Bricks, bed and head joints are supposed to undergo an affine displacement, while cross joints are supposed to undergo a displacement field described by a second order polynomial function of the position x .

$$\hat{u}(x) = \hat{u}(g^i) + H^i \cdot (x - g^i) \quad \forall x \in \Omega^i \quad i = 1, \dots, 9 \quad (4.16)$$

$$\hat{u}(x) = \hat{u}(g^i) + H^i \cdot (x - g^i) + \frac{1}{2} [\mathbf{B}^i \cdot (x - g^i)] \cdot (x - g^i) \quad (4.17)$$

$$\forall x \in \Omega^i \quad i = 10, 11$$

where g^i is the centre of each sub-domain depicted in Figure 4.2, H^i is a second order tensor and \mathbf{B}^i a symmetric third order tensor of \mathbb{R}^3 . In order to represent an admissible displacement field, $\hat{u}(x)$ has to fulfil the boundary conditions, Eq. (4.13) which express the periodicity on opposite sides of $\partial\hat{\Omega}_{RVE}$, together with

the compatibility conditions between each sub-domain, which ensure that the displacement field is continuous on Ω_{RVE} , i.e. $\hat{u}(x) \in H^1(\Omega_{RVE})$.

Periodicity conditions

In order to express explicitly the restrictions on the kinematics that derive from the periodicity conditions, let us consider two homologue points $p^i \in \partial\Omega^i$ and $p^j \in \partial\Omega^j$ that belong to the boundary $\partial\Omega_{RVE}$ and correspond each other by periodicity, that is:

$$p^i - p^j = m_1 i_1 + m_2 i_2 \quad (4.18)$$

where i_1 and i_2 are the directions of periodicity, Eq. (4.1), and m_1, m_2 are integer coefficients in the range $[-1, 1]$, Figure 4.3.

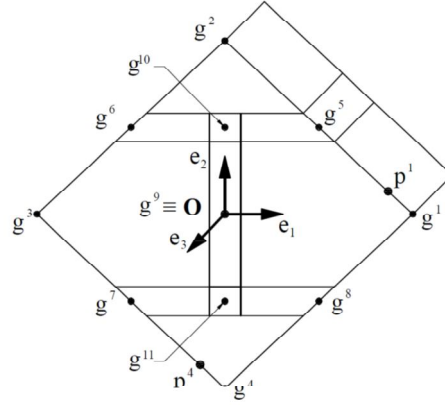


Figure 4.3 Example of points p^i and p^j that correspond by periodicity, Eq. (4.18).

It is worth noting that the centres g^i and g^j of the domains Ω^i and Ω^j are homologues too and fulfil the following condition:

$$p^i - p^j = g^i - g^j \quad (4.19)$$

According to Eq. (4.16) the relative displacement between points p^i and p^j reads:

$$\hat{u}(p^i) - \hat{u}(p^j) = \hat{u}(g^i) - \hat{u}(g^j) + (H^i - H^j) \cdot (p^i - g^i) \quad (4.20)$$

According to the periodicity of the fluctuating displacement field $\hat{u}(x)$, Eq.(4.13), the quantities $\hat{u}(p^i) - \hat{u}(p^j)$ and $\hat{u}(g^i) - \hat{u}(g^j)$ vanish, meaning that $H^i = H^j$.

Following the same reasoning for all the couples of points that fulfil Eq. (4.18),

it is straightforward to prove that the restriction on the kinematics given by the periodicity conditions reduces to:

$$H^i = H \quad i=1,...,4 \quad (4.21)$$

$$H^5 = H^7 \quad (4.22)$$

$$H^6 = H^8 \quad (4.23)$$

where H denotes from now on the gradient of the displacement field that takes place within all the bricks.

Compatibility conditions

The compatibility of the displacement field requires that the piecewise function introduced for $\hat{u}(x)$ is continuous within Ω_{RVE} . Referring to the bed joints, let us consider, for instance, two points $q^i \in \partial\Omega^5 \cap \partial\Omega^2$ and $q^j \in \partial\Omega^7 \cap \partial\Omega^4$ that fulfil the following relationships, Figure 4.4:

$$q^i - g^5 = -(q^j - g^7) \quad (4.24)$$

$$q^i - g^2 = -(q^j - g^4) \quad (4.25)$$

The relative displacement of the abovementioned points according to Eqs. (4.16),(4.21),(4.22) writes:

$$\hat{u}(q^i) - \hat{u}(q^j) = H^5 \cdot (q^i - g^5) - H^5 \cdot (q^j - g^7) \quad (4.26)$$

$$\hat{u}(q^i) - \hat{u}(q^j) = H \cdot (q^i - g^2) - H \cdot (q^j - g^4) \quad (4.27)$$

Now, by exploiting Eqs. (4.24)-(4.25) and equating the above expressions, the following relationship is obtained:

$$H^5 \cdot (q^i - g^5) = H \cdot (q^i - g^2) \quad (4.28)$$

It is possible to recast Eq. (4.28) by choosing three points q^i in order to obtain a linear system of nine independent equations, the resolution of which makes it possible to express the components of tensor H^5 and H^7 as a function of the components of tensor H , Eq. (4.29).

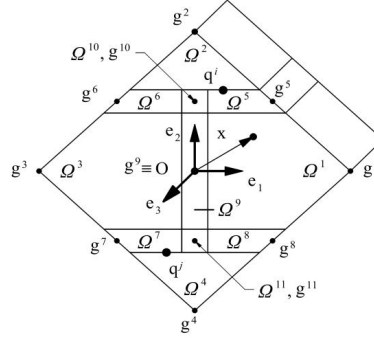


Figure 4.4 Example of points q^i and q^j that fulfil Eqs. (4.24)-(4.25).

$$\begin{aligned}
 H^{5-7} = & H_{11} \mathbf{e}_1 \otimes \mathbf{e}_1 + \left[\frac{(l_b + t_h)}{2 t_m} H_{11} - \frac{h_b}{t_m} H_{12} \right] \mathbf{e}_1 \otimes \mathbf{e}_2 + H_{13} \mathbf{e}_1 \otimes \mathbf{e}_3 + \\
 & H_{21} \mathbf{e}_2 \otimes \mathbf{e}_1 + \left[\frac{(l_b + t_h)}{2 t_m} H_{21} - \frac{h_b}{t_m} H_{22} \right] \mathbf{e}_2 \otimes \mathbf{e}_2 + H_{23} \mathbf{e}_2 \otimes \mathbf{e}_3 + \\
 & H_{31} \mathbf{e}_3 \otimes \mathbf{e}_1 + \left[\frac{(l_b + t_h)}{2 t_m} H_{31} - \frac{h_b}{t_m} H_{32} \right] \mathbf{e}_3 \otimes \mathbf{e}_2 + H_{33} \mathbf{e}_3 \otimes \mathbf{e}_3
 \end{aligned} \quad (4.29)$$

Similarly, referring to Ω^6 and Ω^8 , the following relationships for tensor H^6 and H^8 are obtained, Eq. (4.30).

$$\begin{aligned}
 H^{6-8} = & H_{11} \mathbf{e}_1 \otimes \mathbf{e}_1 - \left[\frac{(l_b + t_h)}{2 t_m} H_{11} + \frac{h_b}{t_m} H_{12} \right] \mathbf{e}_1 \otimes \mathbf{e}_2 + H_{13} \mathbf{e}_1 \otimes \mathbf{e}_3 + \\
 & H_{21} \mathbf{e}_2 \otimes \mathbf{e}_1 - \left[\frac{(l_b + t_h)}{2 t_m} H_{21} + \frac{h_b}{t_m} H_{22} \right] \mathbf{e}_2 \otimes \mathbf{e}_2 + H_{23} \mathbf{e}_2 \otimes \mathbf{e}_3 + \\
 & H_{31} \mathbf{e}_3 \otimes \mathbf{e}_1 - \left[\frac{(l_b + t_h)}{2 t_m} H_{31} + \frac{h_b}{t_m} H_{32} \right] \mathbf{e}_3 \otimes \mathbf{e}_2 + H_{33} \mathbf{e}_3 \otimes \mathbf{e}_3
 \end{aligned} \quad (4.30)$$

A similar reasoning can be followed with respect to the kinematics of the head joint, for which the relationship found for H^9 reads:

$$\begin{aligned}
 H^9 = & -\frac{l_b}{t_h} H_{11} \mathbf{e}_1 \otimes \mathbf{e}_1 + H_{12} \mathbf{e}_1 \otimes \mathbf{e}_2 + H_{13} \mathbf{e}_1 \otimes \mathbf{e}_3 - \frac{l_b}{t_h} H_{21} \mathbf{e}_2 \otimes \mathbf{e}_1 + \\
 & H_{22} \mathbf{e}_2 \otimes \mathbf{e}_2 + H_{23} \mathbf{e}_2 \otimes \mathbf{e}_3 - \frac{l_b}{t_h} H_{31} \mathbf{e}_3 \otimes \mathbf{e}_1 + H_{32} \mathbf{e}_3 \otimes \mathbf{e}_2 + \\
 & H_{33} \mathbf{e}_3 \otimes \mathbf{e}_3
 \end{aligned} \quad (4.31)$$

Concerning the cross joints, let us consider, for instance, two points $q^i \in \partial\Omega^{10} \cap \partial\Omega^i$ and $q^j \in \partial\Omega^{10} \cap \partial\Omega^j$ pertaining to the borders that Ω^{10} has in common with the bricks, $i, j=1, \dots, 4$.

According to Eqs. (4.16)-(4.17) the relative displacement between points q^i and q^j reads:

$$\begin{aligned} H \cdot (q^i - g^i) - H \cdot (q^j - g^j) = \\ H^{10} \cdot (q^i - q^j) + \frac{1}{2} [B^{10} \cdot (q^i - q^j)] \cdot (q^i - q^j) \end{aligned} \quad (4.32)$$

$i, j = 1, \dots, 4$

By writing Eq. (4.32) choosing nine pairs of points q^i and q^j , it is possible to obtain a linear system of 27 independent equations and thus to define tensors H^{10} and B^{10} , as a linear function of H :

$$\begin{aligned} H^{10} = & -\frac{(l_b - t_h)}{2 t_h} H_{11} e_1 \otimes e_1 - \frac{h_b}{t_m} H_{12} e_1 \otimes e_2 + H_{13} e_1 \otimes e_3 + \\ & -\frac{(l_b - t_h)}{2 t_h} H_{21} e_2 \otimes e_1 - \frac{h_b}{t_m} H_{22} e_2 \otimes e_2 + H_{23} e_2 \otimes e_3 + \\ & -\frac{(l_b - t_h)}{2 t_h} H_{31} e_3 \otimes e_1 - \frac{h_b}{t_m} H_{32} e_3 \otimes e_2 + H_{33} e_3 \otimes e_3 \end{aligned} \quad (4.33)$$

$$\begin{aligned} B^{10} = & H_{11} \frac{(l_b + t_h)}{t_m t_h} [e_1 \otimes e_1 \otimes e_2 + e_1 \otimes e_2 \otimes e_1] + \\ & H_{21} \frac{(l_b + t_h)}{t_m t_h} [e_2 \otimes e_1 \otimes e_2 + e_2 \otimes e_2 \otimes e_1] + \\ & H_{31} \frac{(l_b + t_h)}{t_m t_h} [e_3 \otimes e_1 \otimes e_2 + e_3 \otimes e_2 \otimes e_1] \end{aligned} \quad (4.34)$$

By following an analogous reasoning, one would find the following expressions for tensors H^{11} and B^{11} :

$$H^{11} = H^{10} \quad (4.35)$$

$$B^{11} = -B^{10} \quad (4.36)$$

Some considerations on the main simplifications deriving from the kinematics adopted prove necessary. Apart from the quadratic terms pertaining to the cross joints, Eq. (4.17), the fluctuating displacement field $\hat{u}(x)$ may be

expressed as a linear function of tensor H , that is:

$$\hat{u}(x) \approx \hat{u}(g^i) + (A^i : H) \cdot (x - g^i) \quad i = 1, \dots, 11 \quad (4.37)$$

where A^i is a fourth order tensor of \mathbb{R}^3 that reduces to the identity tensor for $i = 1, \dots, 4$, Eq. (4.21), while for $i = 5, \dots, 11$, Eqs. (4.29)-(4.35), depends on the geometrical properties of mortar and brick phases. The full kinematics of Ω_{RVE} is then defined by the nine components of tensor H , which further reduce to four provided that, owing to the symmetry of the problem with respect to the middle plane of the wall, $H_{13}^i, H_{31}^i, H_{23}^i, H_{32}^i$ are null. Accordingly, the microscopic strain and stress fields reduces to piece-wise constant fields:

$$\sigma(x) = \sigma^i \quad \forall x \in \Omega^i \quad (4.38)$$

$$\varepsilon(x) = \varepsilon^i \quad \forall x \in \Omega^i \quad (4.39)$$

where σ^i, ε^i are the stress and the strain that take place within the generic sub domain Ω^i .

From tensor to Voigt notation

The tensor notation adopted until now proves suitable to exploit both periodicity and compatibility conditions in a rather simple way in terms of the displacement field $\hat{u}(x)$. Alternatively, the same conditions may be imposed directly on the strain fields pertaining to each sub-domain, see Zucchini and Lourenço (2002) and Lopez *et al.* (1999). The latter approaches require a bigger effort since periodicity and compatibility equations are derived, first, by analysing the deformation of the basic cell for different loading conditions, then, by superimposing the results obtained. Conversely, when solving the localization problem, the fourth order tensors obtained in the previous paragraphs prove difficult to handle. Therefore, once the kinematics of Ω_{RVE} has been defined, Eq.(4.37), it is convenient to adopt a Voigt-type notation as explained next. The non-null components of the displacement's gradient H^i , of the microscopic stress σ^i and strain ε^i , that pertains to each sub-domain Ω^i , are collected into vectors:

$$\sigma^i = \{ \sigma_{11}^i \quad \sigma_{22}^i \quad \sigma_{33}^i \quad \tau_{12}^i \}^T \quad (4.40)$$

$$\varepsilon^i = \{ \varepsilon_{11}^i \quad \varepsilon_{22}^i \quad \varepsilon_{33}^i \quad \gamma_{12}^i \}^T \quad (4.41)$$

$$\mathbf{H}^i = \{ H_{11}^i \quad H_{22}^i \quad H_{33}^i \quad H_{12}^i \quad H_{21}^i \}^T \quad (4.42)$$

The same applies to the macroscopic strain:

$$\mathbf{E} = \{ E_{11} \quad E_{22} \quad E_{33} \quad E_{12} \}^T \quad (4.43)$$

The relation between the gradient of displacement \mathbf{H}^i and the deformation of the sub-domain $\boldsymbol{\varepsilon}^i$, Eq. (4.12), writes:

$$\boldsymbol{\varepsilon}^i = \mathbf{E} + \mathbf{M}_s \cdot \mathbf{H}^i \quad \text{with} \quad \mathbf{M}_s = \begin{bmatrix} 1 & 0 & 0 & 0 & 0 \\ 0 & 1 & 0 & 0 & 0 \\ 0 & 0 & 1 & 0 & 0 \\ 0 & 0 & 0 & 1 & 1 \end{bmatrix} \quad (4.44)$$

Higher order linear applications, *i.e.* \mathbf{A}^i and \mathbf{C}^i , are collected into second order tensor. Accordingly, the constitutive relation of the sub domain \mathcal{Q}^i , Eq. (4.2), writes as reported in Eq. (4.45).

$$\boldsymbol{\sigma}^i = \mathbf{C}^i \cdot \boldsymbol{\varepsilon}^i \quad \text{with} \quad \mathbf{C}^i = \begin{bmatrix} \lambda^i + 2\mu^i & \lambda^i & \lambda^i & 0 \\ \lambda^i & \lambda^i + 2\mu^i & \lambda^i & 0 \\ \lambda^i & \lambda^i & \lambda^i + 2\mu^i & 0 \\ 0 & 0 & 0 & \mu^i \end{bmatrix} \quad (4.45)$$

In the latter expression λ^i, μ^i are the Lamé's constants. The compatibility of the displacement fields among the sub-domain of the \mathcal{Q}_{RVE} , Eq.(4.37), may be expressed as:

$$\mathbf{H}^i = \mathbf{A}^i \cdot \mathbf{H} \quad (4.46)$$

where matrixes \mathbf{A}^i are reported in the following.

$$\mathbf{A}^{5-7} = \begin{bmatrix} 1 & 0 & 0 & 0 & 0 \\ 0 & -\frac{h_b}{t_m} & 0 & 0 & \frac{(l_b + t_h)}{2 t_m} \\ 0 & 0 & 1 & 0 & 0 \\ \frac{(l_b + t_h)}{2 t_m} & 0 & 0 & -\frac{h_b}{t_m} & 0 \\ 0 & 0 & 0 & 0 & 1 \end{bmatrix} \quad (4.47)$$

$$\mathbf{A}^{6-8} = \begin{bmatrix} 1 & 0 & 0 & 0 & 0 \\ 0 & -\frac{h_b}{t_m} & 0 & 0 & -\frac{(l_b + t_h)}{2 t_m} \\ 0 & 0 & 1 & 0 & 0 \\ -\frac{(l_b + t_h)}{2 t_m} & 0 & 0 & -\frac{h_b}{t_m} & 0 \\ 0 & 0 & 0 & 0 & 1 \end{bmatrix} \quad (4.48)$$

$$\mathbf{A}^9 = \begin{bmatrix} -\frac{l_b}{t_h} & 0 & 0 & 0 & 0 \\ 0 & 1 & 0 & 0 & 0 \\ 0 & 0 & 1 & 0 & 0 \\ 0 & 0 & 0 & 1 & 0 \\ 0 & 0 & 0 & 0 & -\frac{l_b}{t_h} \end{bmatrix} \quad (4.49)$$

$$A^{10-11} = \begin{bmatrix} -\frac{(l_b - t_h)}{2 t_h} & 0 & 0 & 0 & 0 \\ 0 & -\frac{h_b}{t_m} & 0 & 0 & 0 \\ 0 & 0 & 1 & 0 & 0 \\ 0 & 0 & 0 & -\frac{h_b}{t_m} & 0 \\ 0 & 0 & 0 & 0 & -\frac{(l_b - t_h)}{2 t_h} \end{bmatrix} \quad (4.50)$$

A closed form solution for the localization problem

In order to solve the boundary value problem attached to Ω_{RVE} the Galerkin method is adopted here. The test function $\hat{u}^{test}(x)$ is assumed to have the same shape of $\hat{u}(x)$ as defined in Eq. (4.37). By adopting the Voigt-like notation, the weak formulation of the localization problem, Eq. (4.14), writes:

$$\int_{\Omega_{RVE}} \sigma(x) \cdot \nabla \hat{u}^{test}(x) \, dx \approx \sum_i \Omega^i \sigma^{i,T} \cdot M_s \cdot A^i \cdot H^{test} = 0 \quad \forall H^{test} \in \mathbb{R}^5 \quad (4.51)$$

The latter equality holds for all the possible choice of the test function H^{test} over \mathbb{R}^5 , so that it is possible to write:

$$\sum_i \Omega^i \sigma^{i,T} \cdot M_s \cdot A^i = 0 \quad (4.52)$$

which is a system of five equations expressing, in average sense, the equilibrium over Ω_{RVE} in terms of the microscopic stress components. By introducing the constitutive relation of the phases, Eq.(4.45), into the weak formulation, one obtains:

$$\sum_i \Omega^i [C^i \cdot (E + M_s \cdot A^i \cdot H)]^T \cdot M_s \cdot A^i = 0 \quad (4.53)$$

After some manipulations, the latter expression may be rewritten as:

$$\left(\sum_i \Omega^i A^{i,T} \cdot M_s^T \cdot C^i \right) \cdot E + \left(\sum_i \Omega^i A^{i,T} \cdot M_s^T \cdot C^i \cdot M_s \cdot A^i \right) \cdot H = 0 \quad (4.54)$$

which corresponds to a linear system of five equations in terms of the five

components of H . Provided that the coefficient matrix of the latter system is non-singular, the solution of the localization problem writes as:

$$H = - \left(\sum_i \Omega^i A^{i,T} \cdot M_s^T \cdot C^i \cdot M_s \cdot A^i \right)^{-1} \cdot \left(\sum_i \Omega^i A^{i,T} \cdot M_s^T \cdot C^i \right) E \quad (4.55)$$

By introducing the average operator over Ω_{RVE} defined for piecewise constant fields:

$$\langle \bullet^i \rangle = \frac{1}{\Omega_{RVE}} \sum_i \Omega^i \bullet^i \quad (4.56)$$

Eq. (4.55) reduces to:

$$H = - \left\langle A^{i,T} \cdot M_s^T \cdot C^i \cdot M_s \cdot A^i \right\rangle^{-1} \cdot \left\langle A^{i,T} \cdot M_s^T \cdot C^i \right\rangle \cdot E \quad (4.57)$$

The solution of the localization problem makes it possible to define, apart from a rigid translation, the complete kinematic of the RVE for a given macroscopic strain E . Noteworthy, the component E_{33} remain workless and does not affect the solution of the problem. Accordingly, by neglecting the affine terms pertaining to cross joints and by virtue of Eq. (4.44), the microscopic strain may be expressed as:

$$\begin{aligned} \varepsilon^i &= E + M_s \cdot A^i \cdot H = D^i \cdot E \quad i = 1, \dots, 11 \\ D^i &= I - M_s \cdot A^i \cdot \left\langle A^{i,T} \cdot M_s^T \cdot C^i \cdot M_s \cdot A^i \right\rangle^{-1} \cdot \left\langle A^{i,T} \cdot M_s^T \cdot C^i \right\rangle \cdot E \end{aligned} \quad (4.58)$$

where I is the identity tensor and D^i is the tensor of strain localization, Suquet (1987). The macroscopic stress corresponding to a prescribed macroscopic strain E may be derived by resorting to Eqs. (4.3), (4.45):

$$\Sigma = \langle \sigma^i \rangle = \langle C^i \cdot \varepsilon^i \rangle = \langle C^i \cdot D^i \rangle \cdot E = C^{\text{hom}} \cdot E \quad (4.59)$$

Thus the elasticity tensor of the homogeneous material writes:

$$\begin{aligned} C^{\text{hom}} &= \langle C^i \cdot D^i \rangle = \\ &= \langle C^i \rangle - \left\langle C^i \cdot M_s \cdot A^i \right\rangle \cdot \left\langle A^{i,T} \cdot M_s^T \cdot C^i \cdot M_s \cdot A^i \right\rangle^{-1} \cdot \left\langle A^{i,T} \cdot M_s^T \cdot C^i \right\rangle \end{aligned} \quad (4.60)$$

Finally, the relationship that yields the microscopic stress $\sigma(x)$ in terms of macroscopic stress Σ may be obtained by combining Eqs. (4.45), (4.59):

$$\sigma^i = S^i \cdot \Sigma \quad i=1,\dots,11 \quad \text{where} \quad S^i = C^i \cdot D^i \cdot C^{\text{hom}^{-1}} \quad (4.61)$$

where S^i is the tensor of stress localization pertaining to sub-domain Ω^i .

Discussion and validation of the results

As an alternative to the weak formulation, a variational approach may be followed and the solution of the localization problem may be found by imposing the minimization of the internal strain energy attached to Ω_{RVE} . The two approaches would coincide provided that the constituents exhibit an elastic behaviour. Since the solution of the localization problem is obtained by adopting a compatible approach, the minimization of the strain energy would be performed on a sub-space of \mathbf{V}_{per} , *i.e.* the space of the admissible displacement fields. Thus the elasticity tensor \mathbf{C}^{hom} provided by Eq. (4.60) constitutes an upper bound estimate of the actual elastic tensor of the material. Moreover, the microscopic stress envisaged by the proposed scheme is constant through the thickness of the wall and fulfils the out-of-plane equilibrium only from the macroscopic point of view, $\langle \sigma_{i3}(\mathbf{x}) \rangle = 0$ with $i = 1, 2, 3$, while it violates locally the conditions that the lateral faces of the domain are stress-free, Eq. (4.9). Such an assumption corresponds to the generalized plane strain (GPS) scheme, which is representative of the behaviour of the material located far from the external faces of the wall, see also Anthoine (1997) and Massart *et al.* (2005). For these reasons the upper bound solution obtained is found to be independent of the actual thickness of the wall T , Figure 4.1.

Alternatively, it is possible to solve the localization problem in plane stress (PS) condition assuming that the local stress components $\sigma_{i3}(\mathbf{x})$, $i = 1, \dots, 3$, are zero, handling the microscopic fields as second order tensors defined on \mathbb{R}^2 , Eqs. (4.62)-(4.65), adopting a proper elasticity tensor for the constituents and defining tensors \mathbf{A}^i and \mathbf{M}_s accordingly:

$$\boldsymbol{\sigma}_{PS} = \{ \sigma_{11}^i \quad \sigma_{22}^i \quad \tau_{12}^i \}^T \quad (4.62)$$

$$\boldsymbol{\varepsilon}_{PS}^i = \{ \varepsilon_{11}^i \quad \varepsilon_{22}^i \quad \gamma_{12}^i \}^T \quad (4.63)$$

$$\mathbf{H}_{PS}^i = \{ H_{11}^i \quad H_{22}^i \quad H_{12}^i \quad H_{21}^i \}^T \quad (4.64)$$

$$\mathbf{E} = \{ E_{11} \quad E_{22} \quad E_{12} \}^T \quad (4.65)$$

The solution found in the latter case is thought to be representative of the behaviour of the material located in correspondence to the external faces of the wall. The differences between the PS and the GPS statement of the localization problem are discussed in subsequent sections together with a comparison with

standard finite element analyses and with formulations previously proposed in literature for the homogenization of masonry.

Parametrical analysis

A parametrical analysis was performed in order to investigate the influences of joint thickness and of elastic properties of the components (mortar and brick) on the macroscopic properties of masonry assemblage. The bricks adopted have a length of 250 mm, height of 55 mm and width of 120 mm, and reflect the dimensions of the most common typology of units adopted in Italy and produced in accordance with UNI 5628/65. The Young modulus Y_b and the Poisson coefficient of the brick ν_b were assumed equal to 11000 MPa and 0.20, respectively. No distinction was made between the properties of head and bed joints, which have the same thickness t . Mortar properties were defined in terms of the Young Modulus Y_m and the Poisson coefficient ν_m , with the latter assumed as equal to 0.25. By keeping the properties of the brick constant, the elastic properties of masonry as a homogeneous material were evaluated in plane stress (PS) and in generalised plane strain (GPS) conditions, varying the thickness of the joint from 0 to 30 mm and for different Y_b / Y_m ratios ranging from 1.1 to 10. To be noted that the mortar was assumed more deformable than the brick in order to reflect the most common case of ancient and modern brickwork. The results of the parametrical analysis are reported in Figure 4.5 and in Figure 4.6 where masonry elastic constants are plotted as relative values of the elastic constants of the brick. According to the proposed model, masonry is characterized by a high degree of anisotropy, with a stiffer behaviour in the horizontal direction compared to the vertical direction. This is due to the fact that in the horizontal direction, the staggered configuration involves normal stress in brick and head joint combined with shear transfer in the bed joints while in vertical direction bricks and bed joints can be assimilated to a chain association. The overall elastic modulus of the material decreases as the mortar joint deformability or thickness increases. Note that three-dimensional modelling of the RVE proves slightly stiffer compared to the plane stress condition except for the shear modulus, the expression of which remains unchanged passing from the PS to the GPS condition, in agreement with the observation made by Anthoine (1995).

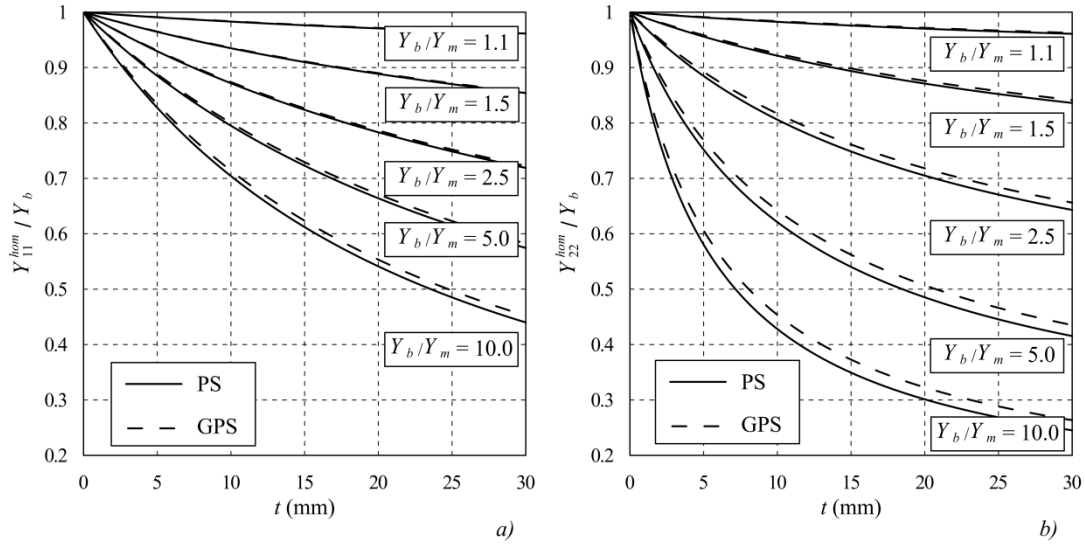


Figure 4.5 Elastic moduli of masonry in horizontal (a) and vertical (b) directions versus the thickness of the joints t evaluated in plane stress (PS) and in generalised plane strain (GPS) conditions for different ratios of the Young moduli of brick and mortar, Y_b/Y_m .

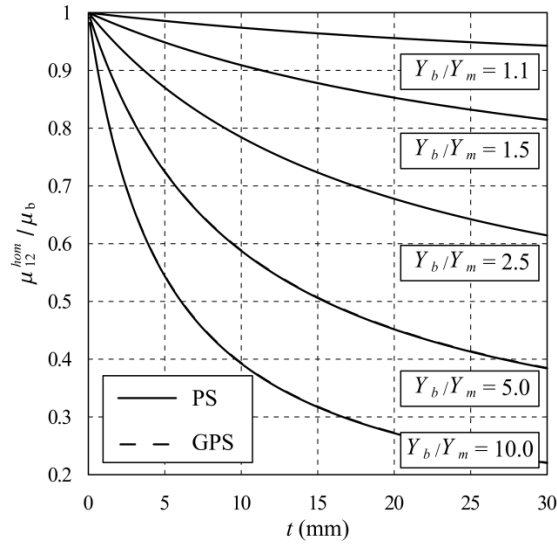


Figure 4.6 Shear modulus of masonry versus the thickness of the joints t evaluated in plane stress (PS) and in generalised plane strain (GPS) conditions for different ratios of the Young moduli of brick and mortar, Y_b/Y_m .

Comparison with closed-form solutions given in the literature

In order to test the robustness of the proposed approach, the solution of the localization problem obtained in the present work is now studied in the limit conditions where the joints reduce to interfaces, i.e. the thickness t reduces to zero. Let us then distinguish two cases. In the first case let us consider a perfectly cohesive interface in which the continuity of the displacement field between adjacent bricks is ensured, that is:

$$\lim_{t \rightarrow 0} \frac{\lambda_m + 2\mu_m}{t} = \infty \quad (4.66)$$

$$\lim_{t \rightarrow 0} \frac{\mu_m}{t} = \infty \quad (4.67)$$

In the second case let us assume that the elastic properties of mortar vary with t so that in the limit the joint maintains a finite stiffness:

$$\lim_{t \rightarrow 0} \frac{\lambda_m + 2\mu_m}{t} = K_n \quad (4.68)$$

$$\lim_{t \rightarrow 0} \frac{\mu_m}{t} = K_t \quad (4.69)$$

where K_n and K_t denote the normal and tangential stiffness of the interface. In these conditions the joint behaves as an elastic interface that allows a displacement jump between adjacent bricks, see also Cecchi and Sab (2002a).

In the simple case in which both head and bed joints reduce to perfectly cohesive interfaces the heterogeneity of the material induced by the presence of mortar joints vanishes and the macroscopic elasticity tensor provided by Eq. (4.60) reduces to that of the brick C^b :

$$\lim_{t \rightarrow 0} C^{\text{hom}} = C^b \quad (4.70)$$

In the case where only the head joint reduces to perfectly cohesive interface, masonry reduces to a stratified material (SM) made of alternating horizontal layers of mortar and brick. The elastic constants obtained by the proposed model are reported hereafter and result in agreement with those originally proposed by Salomon (1968) and then extended to the case of masonry by Pande *et al.* (1989), Eqs. (3.71)-(4.74).

$$\frac{1}{Y_{SM,11}^{\text{hom}}} = \quad (4.71)$$

$$\frac{(h_b + t)[t \mu_m (\lambda_b + 2\mu_b)(\lambda_m + \mu_m) + h_b \mu_b (\lambda_b + \mu_b)(\lambda_m + 2\mu_m)]}{(h_b \mu_b + t \mu_m) [h_b \mu_b (3\lambda_b + 2\mu_b)(\lambda_m + 2\mu_m) + t \mu_m (3\lambda_m + 2\mu_m)(\lambda_b + 2\mu_b)]}$$

$$\frac{v_{SM,21}^{\text{hom}}}{Y_{SM,11}^{\text{hom}}} = - \frac{t \lambda_m (\lambda_b + 2\mu_b) + h_b \lambda_b (\lambda_m + 2\mu_m)}{2 [h_b \mu_b (3\lambda_b + 2\mu_b)(\lambda_m + 2\mu_m) + t \mu_m (3\lambda_m + 2\mu_m)(\lambda_b + 2\mu_b)]} \quad (4.72)$$

$$\frac{1}{Y_{SM,22}^{\text{hom}}} = \quad (4.73)$$

$$\frac{t^2 (\lambda_b + 2\mu_b)(\lambda_m + \mu_m) + h_b^2 (\lambda_b + \mu_b)(\lambda_m + 2\mu_m)}{(h_b + t) [h_b \mu_b (3\lambda_b + 2\mu_b)(\lambda_m + 2\mu_m) + t \mu_m (3\lambda_m + 2\mu_m)(\lambda_b + 2\mu_b)]} +$$

$$\frac{t h_b [2(\lambda_b \lambda_m + \mu_b^2 + \mu_m^2) + 3(\lambda_b \mu_b + \lambda_m \mu_m)]}{(h_b + t) [h_b \mu_b (3\lambda_b + 2\mu_b)(\lambda_m + 2\mu_m) + t \mu_m (3\lambda_m + 2\mu_m)(\lambda_b + 2\mu_b)]}$$

$$\frac{1}{\mu_{SM,12}^{\text{hom}}} = \frac{t}{h_b + t} \frac{1}{\mu_m} + \frac{h_b}{h_b + t} \frac{1}{\mu_b} \quad (4.74)$$

Finally, when the whole set of joints reduces to elastic interfaces, the elastic constants of masonry provided by Eq. (4.60) reduce to:

$$\frac{1}{Y_{IM,11}^{\text{hom}}} = \frac{4 h_b}{4 h_b l_b K_n + l_b^2 K_t} + \frac{\lambda_b + 2\mu_b}{\mu_b (3\lambda_b + 2\mu_b)} \quad (4.75)$$

$$\frac{1}{Y_{IM,22}^{\text{hom}}} = \frac{1}{h_b K_n} + \frac{\lambda_b + 2\mu_b}{\mu_b (3\lambda_b + 2\mu_b)} \quad (4.76)$$

$$\frac{v_{IM,21}^{\text{hom}}}{Y_{IM,11}^{\text{hom}}} = - \frac{\lambda_b}{\mu_b (6\lambda_b + 4\mu_b)} \quad (4.77)$$

$$\frac{1}{\mu_{IM,12}^{\text{hom}}} = \frac{1}{h_b K_t} + \frac{4 h_b}{l_b^2 K_n + 4 h_b l_b K_t} + \frac{1}{\mu_b} \quad (4.78)$$

where the subscript “IM” stands for interface model. Note that the expressions given in Eqs. (4.75)-(4.78) generalize those obtained by de Felice *et al.* (1995,

2001, 2010) and Mauro (2008), who referred directly to a system of bricks connected by elastic interfaces under plane stress condition.

A comparison between the elastic modulus given in Eqs. (3.71)-(4.78) and those provided by Eq. (4.60) in GPS condition is shown in Figure 4.7 and Figure 4.8. Please note that the stratified material introduces a small error in predicting the elastic modulus in the vertical direction and the shear modulus. On the contrary, a higher discrepancy is found concerning the elastic modulus in the horizontal direction which is influenced by the deformability of the head joint.

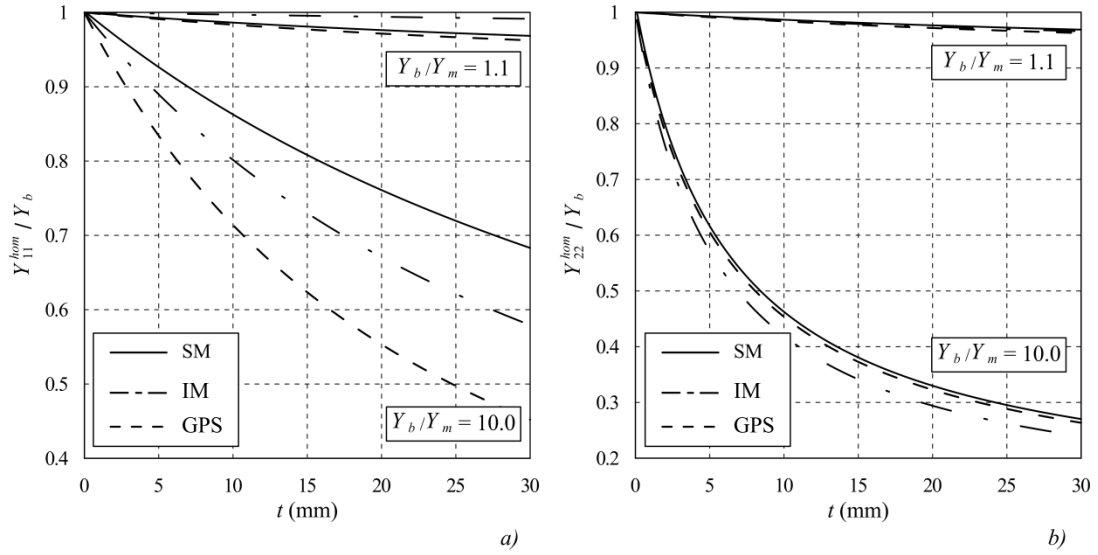


Figure 4.7 Elastic moduli of masonry in horizontal (a) and vertical (b) directions versus the thickness of the joints t evaluated for different ratios of the Young moduli of brick and mortar Y_b/Y_m , referring to the generalized plain strain (GPS) condition, to the stratified model (SM) and to the cohesive interface model (IM).

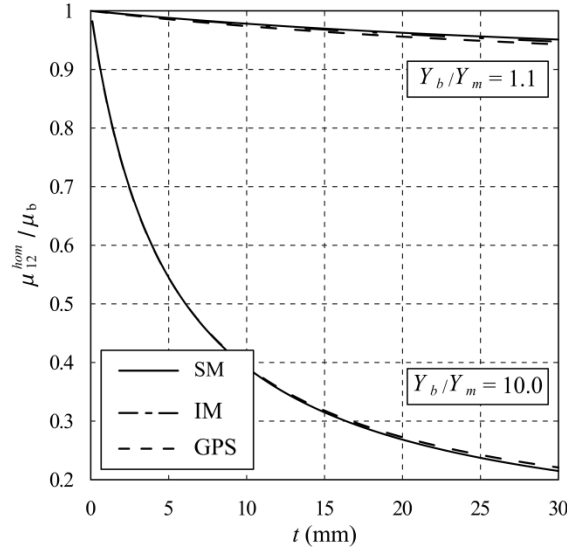


Figure 4.8 Shear modulus of masonry versus the thickness of the joints t evaluated for different ratios of the Young moduli of brick and mortar Y_b/Y_m , referring to the generalized plain strain (GPS) condition, to the stratified model (SM) and to the cohesive interface model (IM).

The model of bricks connected by elastic interfaces can be applied rigorously only for very thin joints since out of this range the hypothesis of the model no longer holds true. In the case of joints having finite thickness it is possible to overcome this limitation by enlarging the dimensions of the brick ($h_b + t, l_b + t$), in order to include the surrounding half-layers of mortar, and assigning the following values to the normal and tangential stiffnesses of the interfaces, see Lourenço and Rots (1997):

$$K_n = \frac{Y_m Y_b}{t (Y_b - Y_m)} \quad (4.79)$$

$$K_t = \frac{\mu_m \mu_b}{t (\mu_b - \mu_m)} \quad (4.80)$$

By introducing the abovementioned modifications a high discrepancy still holds as regards the modulus Y_{11}^{hom} (Figure 4.7a) because of the incapability of the interface model to reproduce the deformation ε_{11} that develops throughout the thickness of the joint, the contribution of which becomes important in the presence of horizontal macroscopic loads. It is worth noting that, even if the

results displayed in terms of elastic modulus are similar, the three models may differ by large amounts in terms of the local stresses acting within each component, giving rise to different predictions when extended to the non-linear range. More precisely, the interface model is unable to reproduce the Poisson interaction between the components deriving from the different stiffness of mortar and brick. This interaction has marginal effects on the elastic moduli of the homogeneous material but plays a relevant role as regards the strength of masonry under compression. In fact, as outlined by Hilsdorf (1969), when mortar is more deformable than the brick the former undergoes a tri-axial compression stresses while the latter undergoes a vertical compression combined with lateral tension which initiates splitting cracks in the brick that are responsible for the failure of masonry. The stratified material takes into account the Poisson interaction between mortar and brick, while is unable to reproduce crack propagation among the head joints, which constitutes the weakest link within the horizontal courses of brick. By adopting the proposed formulation both the Poisson type interaction and the presence of the head joint are properly taken into account.

Comparison with finite element analysis

The localization problem was solved in a standard finite element code for the purpose of testing the accuracy of the proposed model. The RVE reported in Figure 4.9 was adopted owing to its particular properties, *i.e.* the cell has two orthogonal planes of symmetry and is defined by a frame of two orthogonal vectors, that makes it possible to model only a portion of the domain and to reduce the periodicity conditions to ordinary Dirichlet conditions, Anthoine (1995). The three-dimensional problem was defined on one-eighth of the RVE which was divided into 3960 twenty-node hexahedron finite elements, Figure 4.9. The analyses under plane stress condition were carried out on a quarter of the vertical section of the RVE subdivided into 792 eight-node rectangular finite elements, Figure 4.9. Elastic analyses were performed for thickness of the joints varying from 2.5 to 20 mm and reducing Young modulus of mortar so as to obtain Y_b / Y_m ratios ranging from 1 to 1000. Commonly, the initial elastic stiffness of the components leads to relatively low values of the abovementioned ratio in the cases of both new and historic masonry; however, when inelastic behaviour and degradation occur in the joints, the ratio Y_b / Y_m , evaluated referring to the secant stiffness of mortar, may even reach much higher values, explaining the wide range considered for the numerical simulations. The Poisson coefficient of mortar and brick were assumed equal to 0.25 and 0.20

respectively. The relative errors between the proposed model and the finite element analyses are plotted hereafter for three-dimensional (Figure 4.10) and plane stress (Figure 4.11) cases. The comparison confirms that the proposed formulation provides an upper bound estimate for the in-plane behaviour of masonry. For the whole set of analyses performed a good agreement is found in predicting the elastic moduli in the vertical and horizontal directions and the in-plane shear modulus, since the discrepancies are always lower than 7% and 5% for three-dimensional and plane stress conditions, respectively. The Poisson coefficient displays much higher errors, which may reach the magnitude of 50% in the case of lower mortar stiffness and higher joint thickness. These errors, however, are considered of limited importance since the structural analyses are almost independent of this parameter.

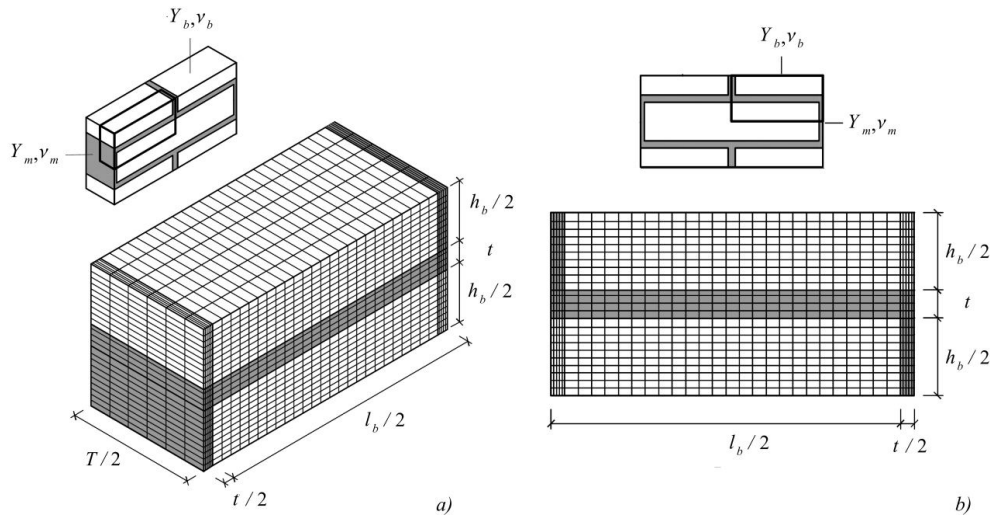


Figure 4.9 Finite element mesh defined on one-eighth of the total volume of the RVE adopted for three-dimensional analysis (a); finite element mesh defined on a quarter of the total RVE adopted for plane stress analysis (b).

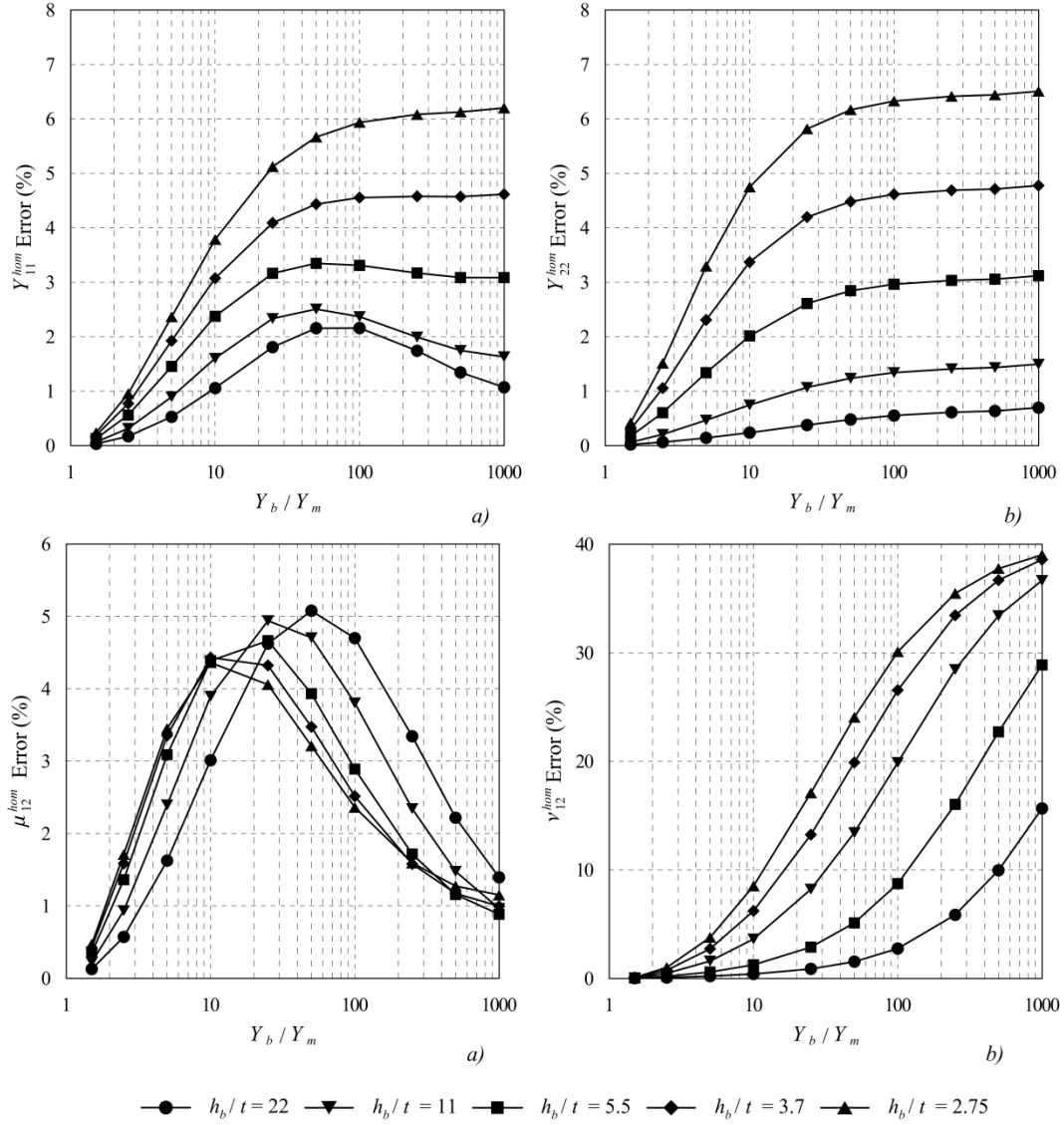


Figure 4.10 Error introduced by the proposed model in evaluating horizontal (a), vertical (b), shear moduli (c) and Poisson coefficient (d) with respect to three-dimensional finite element analyses performed for different ratios between the height of the brick h_b and the thickness of the joints t , varying the ratio between the Young moduli of brick and mortar, Y_b/Y_m .

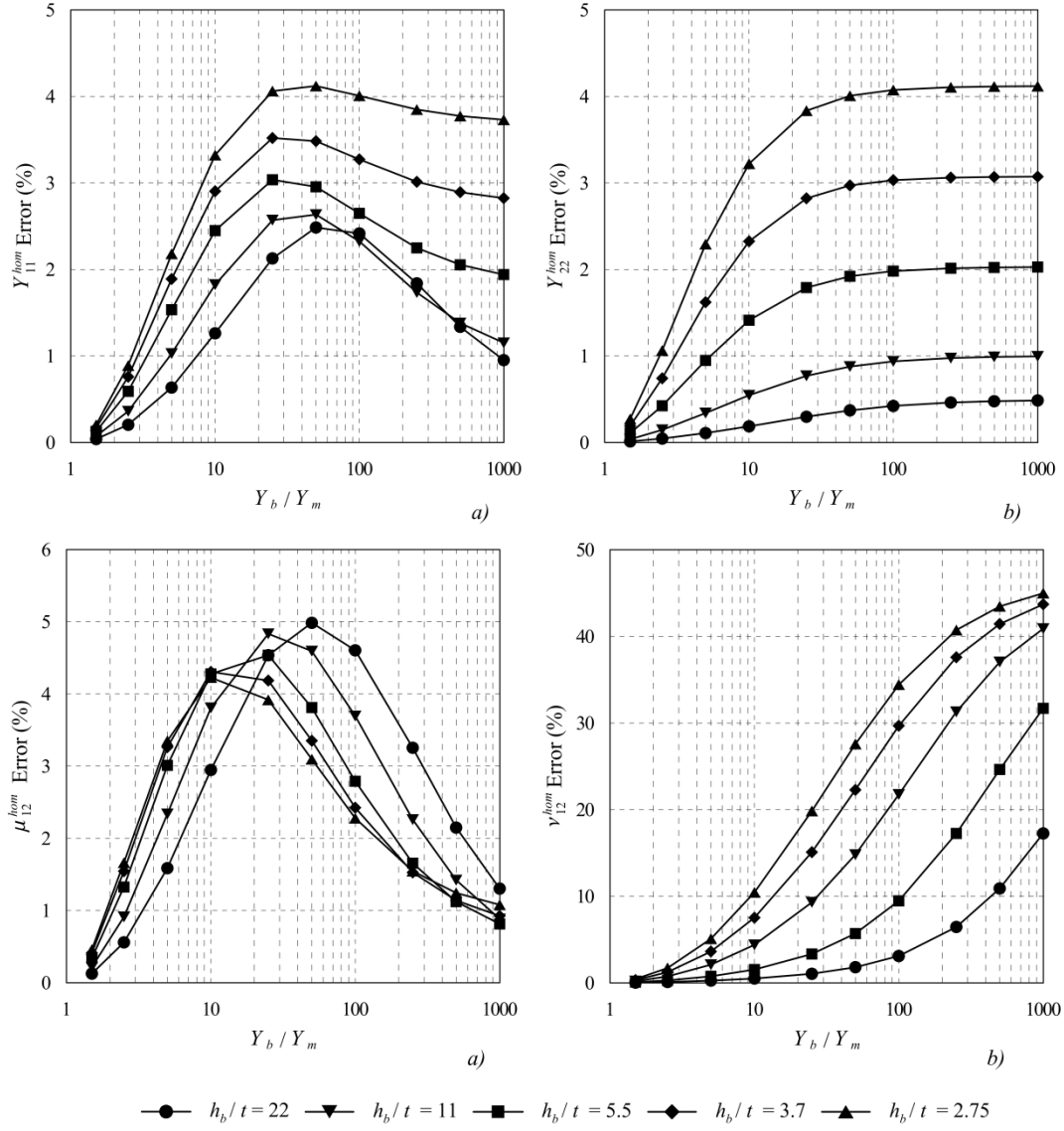


Figure 4.11 Error introduced by the proposed model in evaluating horizontal (a), vertical (b), shear moduli (c) and Poisson coefficient (d) with respect to plane stress finite element analyses performed for different ratios between the height of the brick h_b

The scatter found with finite element analyses derives from the approximation of the strain and strain fields introduced in the proposed homogenization approach. As a matter of fact, this approach accounts for piece-wise constant stress distribution over the RVE, thus, information concerning the stress concentration within mortar and brick is lost, Figure 4.12 . A further issue would consist in evaluating the level of roughness of the model in reproducing the stress fields that develops within the RVE for a given macroscopic stress. For this purpose finite element analysis were conducted applying an unitary macroscopic vertical stress to the RVE considering the joint 10 mm thick and varying the ratio Y_b / Y_m from 1.5 to 1000. The Poisson's ratios of mortar and brick were kept constant and equal to 0.25 and 0.20 respectively. For each sub-domain pertaining to the RVE, the microscopic stress field have been phase-averaged and compared with the microscopic stress predicted by Eq. (4.61).

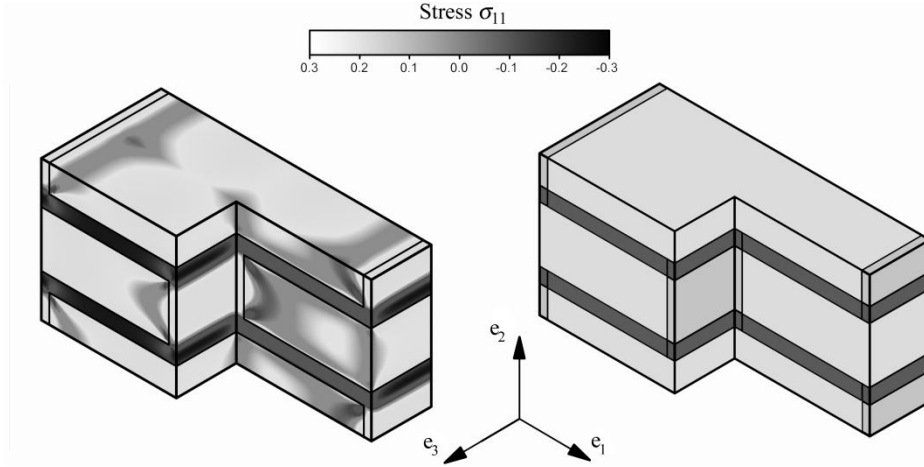


Figure 4.12 Comparison between three dimensional finite element analysis and the simplified homogenization procedure proposed: component σ_{11} of the microscopic stress field for running bond masonry under uniaxial macroscopic compression $\Sigma_{22} = -1$ MPa.

A rather small scatter is found in evaluating bed joint and brick average stresses while an higher discrepancy is found in predicting the microscopic stress acting within the head joint, Figure 4.13. The results shows that when masonry is in compression, the head joint develops transversal tension stresses (σ_{11}, σ_{33}) analogous to those experienced by the brick. Conversely, the former does not benefit, even for moderate Y_b / Y_m ratios, of the vertical compression (σ_{22}) which may explain why vertical joints is the first component to crack when masonry assemblage is loaded in compression perpendicular to bed joints.

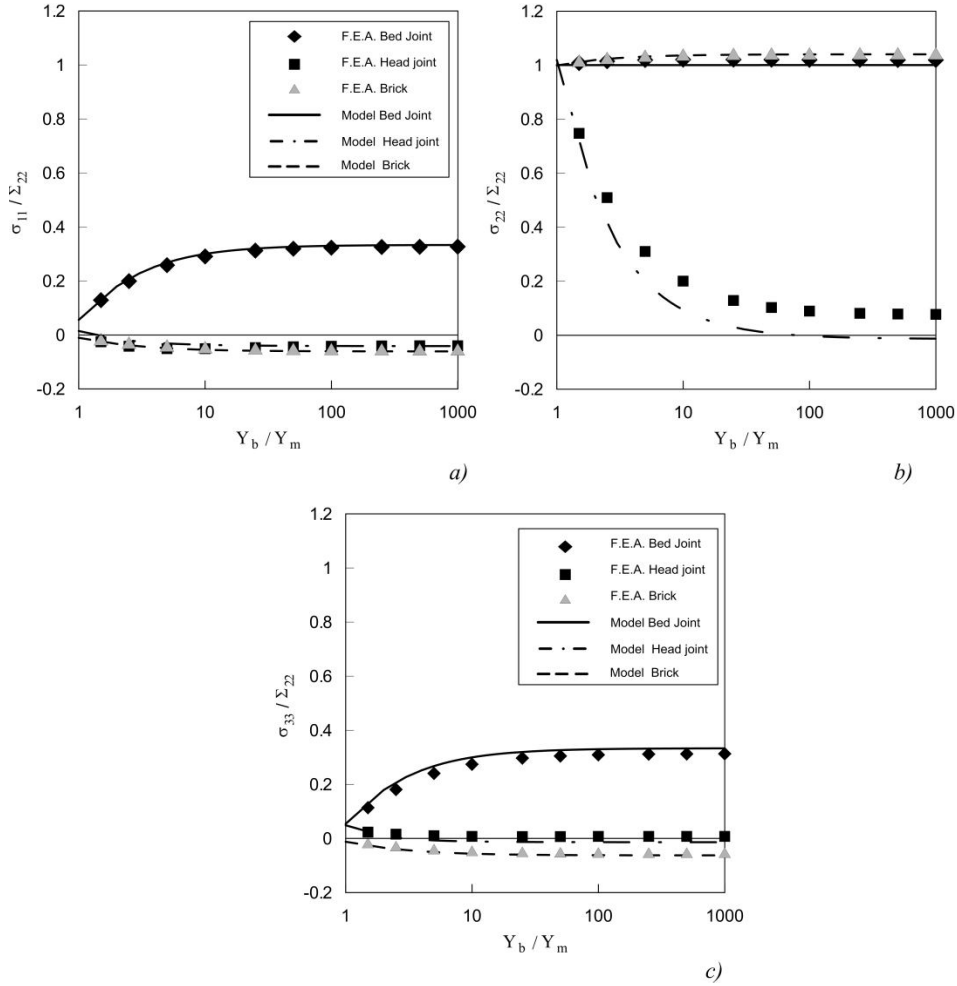


Figure 4.13 Comparison between the phase-averaged stresses evaluated from finite element analyses and the ones predicted by the model for a unitary macroscopic vertical stress Σ_{22} .

Comparison with experimental data

In order to assess the capability of the proposed formulation to reproduce experimental results, data concerning the elastic modulus of masonry perpendicular to bed joints were collected from literature. A common practice in the research field is to perform compressive tests on masonry specimens and separately on small samples of the constituents in order to derive their mechanical properties in term of strength and stiffness. Referring then to the

actual geometry of the brickwork and the individual properties of mortar and brick, a comparison between the predicted elastic modulus and that measured on masonry samples was made as shown in Figure 4.14.

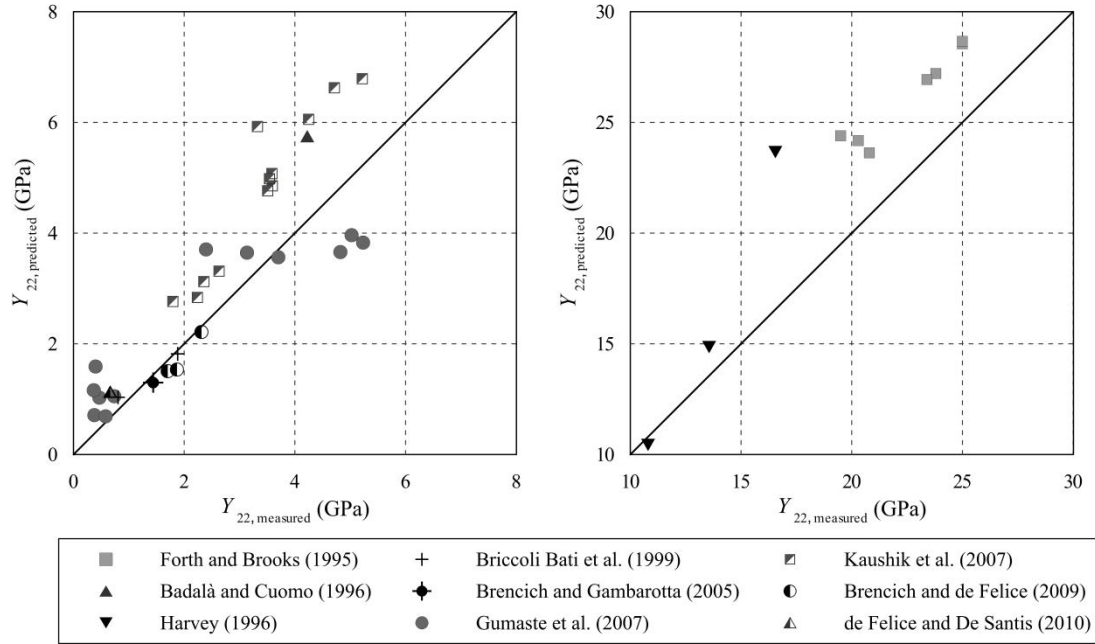


Figure 4.14 Comparison between the elastic modulus in the vertical direction measured on masonry samples, $Y_{22,measured}$, and the respective modulus predicted by the proposed procedure, $Y_{22,predicted}$, referring to mortar and unit properties measured separately.

A fairly good agreement is found with the experimental data. The scatter observed may be related to the different behaviour of unbounded mortar specimens, used in standard tests, and the behaviour of mortar within masonry joints; in fact, the latter is thought to be more deformable because of a weak zone located at brick/mortar interface where diffuse shrinkage cracks occur due to the water suction of the unit, see also Brooks and Abu Baker (1998) for an exhaustive discussion concerning this topic.

Estimate of the homogenized limit elastic domain

A difficult issue in modelling masonry is to deal with the anisotropic behaviour induced by the mortar joints which act as inherent planes of weakness. In fact, as shown experimentally by Page (1981,1983), the strength and the failure mode of masonry panels subjected to proportional biaxial loading are dependent on the direction of the applied load with respect to the orientation of the joints. As usual in cohesion-frictional materials, masonry is found to be much more resistant in compression than in tension. Concerning the failure mode, bed joint cracking and sliding are observed for biaxial tension regimes. Vertical and diagonal cracking of the brick are encountered when vertical compression is accompanied by lateral tension. Finally, when biaxial compressive stresses are applied masonry panels tend to split along the mid-thickness plane showing a transition from in-plane to out-of plane failure.

In literature several attempts have been made to reproduce the directional behaviour of masonry by defining its strength domain. Some approaches, that may be defined as “heuristic”, have been followed by Ganz (1989), Dhanasekar *et al.* (1985) and Andreus (1996) referring to experimental evidence. Introducing non-linear constitutive laws for mortar and brick, the homogenization techniques have been used widely both in an approximate way (Maier *et al.* 1991, Pietruszczak and Niu 1992, Calderini and Lagomarsino 2008) and in a more rigorous way either within the framework of limit analysis (De Buhan and de Felice 1997, Milani *et al.* 2006 and Kawa *et al.* 2008) or accounting for the progressive damage of the constituents (Massart *et al.* 2005).

The following part does not concentrate on the extension to the non-linear range of the proposed scheme but intends to test the capability of the latter to reproduce the limit elastic domain and the triggering failure mode of masonry subjected to in-plane loading under the assumption that the maximum capacity of the homogeneous material is reached whenever the stress acting within one of the components reaches the respective failure criterion.

Statement of the problem

Let us introduce the local strength domain $S(\mathbf{x})$ defined in the space of microscopic stresses:

$$S(\mathbf{x}) = \{\boldsymbol{\sigma} \mid F(\boldsymbol{\sigma}, \mathbf{x}) \leq 0, \mathbf{x} \in \Omega_{RVE}\} \quad (4.81)$$

where the yield function $F(\boldsymbol{\sigma}, \mathbf{x})$ is a periodic function on Ω_{RVE} defining the

boundary of the domain of the admissible stress states, i.e. that can be physically sustained by the material. In our case, assuming that each sub-domain \mathcal{Q}^i is characterized by a proper yield function $F^i(\sigma)$, Eq. (4.81) reduces to:

$$S(x) = \{\sigma \mid F^i(\sigma) \leq 0, x \in \mathcal{Q}^i, i = 1, \dots, 11\} \quad (4.82)$$

where according to periodicity:

$$F^i(\sigma) = F^j(\sigma) \quad i, j = 1, \dots, 4 \quad (4.83)$$

$$F^5(\sigma) = F^7(\sigma) \quad (4.84)$$

$$F^6(\sigma) = F^8(\sigma) \quad (4.85)$$

Let us assume that the maximum capacity of the homogeneous material is reached whenever the stress acting within one of the components reaches the respective limit criterion. Therefore, the aim is to derive the limit elastic domain S^{hom} defined as the set of macroscopic stresses which correspond to an elastic response of masonry:

$$S^{\text{hom}} = \{\Sigma \mid F^{\text{hom}}(\Sigma) \leq 0\} \quad (4.86)$$

where $F^{\text{hom}}(\Sigma) = 0$ is the yield function of the homogeneous material. Before yielding occurs, the behaviour of the material is elastic and the local stress field $\sigma(x)$ can be expressed as a function of the macroscopic stress Σ by means of the relationship of stress localization, Eq. (4.61); accordingly the macroscopic domain S^{hom} can be expressed as:

$$S^{\text{hom}} = \{\Sigma \mid F^i(L^i : \Sigma) \leq 0, \forall i = 1, \dots, 11\} \quad (4.87)$$

which ensures that in none of the sub-domains \mathcal{Q}^i that constitute the RVE, the stress goes beyond its strength domain. For the purpose of deriving the homogenized limit elastic domain, let us refer to an increasing proportional macroscopic loading $\lambda \Sigma$, where λ is the load multiplier and Σ defines the loading direction in the space of the macroscopic stresses, the limit multiplier is given by:

$$\lambda^{\text{lim}} = \min\{\lambda \mid F^i(\lambda L^i \cdot \Sigma) = 0, i = 1, \dots, 11\} \quad (4.88)$$

and the function F^i corresponding to the minimum of λ , singles out the first sub-domain \mathcal{Q}^i that reaches a limit condition and thus the failure mode occurring under the given macroscopic loading path.

This hypothesis reflects the behaviour of an elastic-brittle material and, thereby, in the case of masonry may lead to an underestimation of the actual strength since it neglects the possible reserve of strength deriving from an internal redistribution of stresses among the phases of Ω_{RVE} . On the contrary, on a microscopic scale the effects of the stress concentration is not taken into account when evaluating the failure of brick or mortar joints, since the stress field within Ω_{RVE} is approximated to a piecewise constant function, Eq. (4.61). The latter assumption may lead to an overestimation of the actual strength for non-perfectly plastic behaviour, which is the case of brick and mortar. In order to investigate to what extent the proposed limit elastic domain given in Eq. (4.87) can be used for predicting the failure of masonry under in-plane loads, a phenomenological discussion of the results is given in the next section followed by a comparison with experimental data available in literature.

Description of the failure modes

In Figure 4.15a the limit elastic domain obtained assuming a Mohr-Coulomb criterion for mortar and brick is plotted in the space of the in-plane macroscopic stresses. The geometrical and mechanical parameters adopted are reported in Table 4.1, where f_c and f_t denote respectively the compressive and the tensile strength of the materials.

Mortar			
$Y_m = 2200 \text{ MPa}$	$\nu_m = 0.25$	$t_m = 10 \text{ mm}$	$t_h = 10 \text{ mm}$ $f_c = 5 \text{ MPa}$
$f_t = 0.5 \text{ MPa}$			
Brick			
$Y_b = 11000 \text{ MPa}$	$\nu_b = 0.20$	$h_b = 55 \text{ mm}$	$l_b = 250 \text{ mm}$ $f_c = 15 \text{ MPa}$
$f_t = 1.5 \text{ MPa}$			

Table 4.1 Geometrical and mechanical properties of the phases adopted in defining the limit elastic domain of masonry reported in Figure 4.15

The domain obtained clearly reproduces the anisotropy of masonry. Remarkably, its shape is in close agreement with those of the domains proposed in literature by Dhanasekar *et al.* (1985) and Andreaus (1996) by referring to experimental evidences. Note that, unlike the latter models, which rely upon somewhat heuristic arguments, the one proposed in the present approach was developed in

a rigorous mechanical framework starting from the individual properties of mortar and brick.

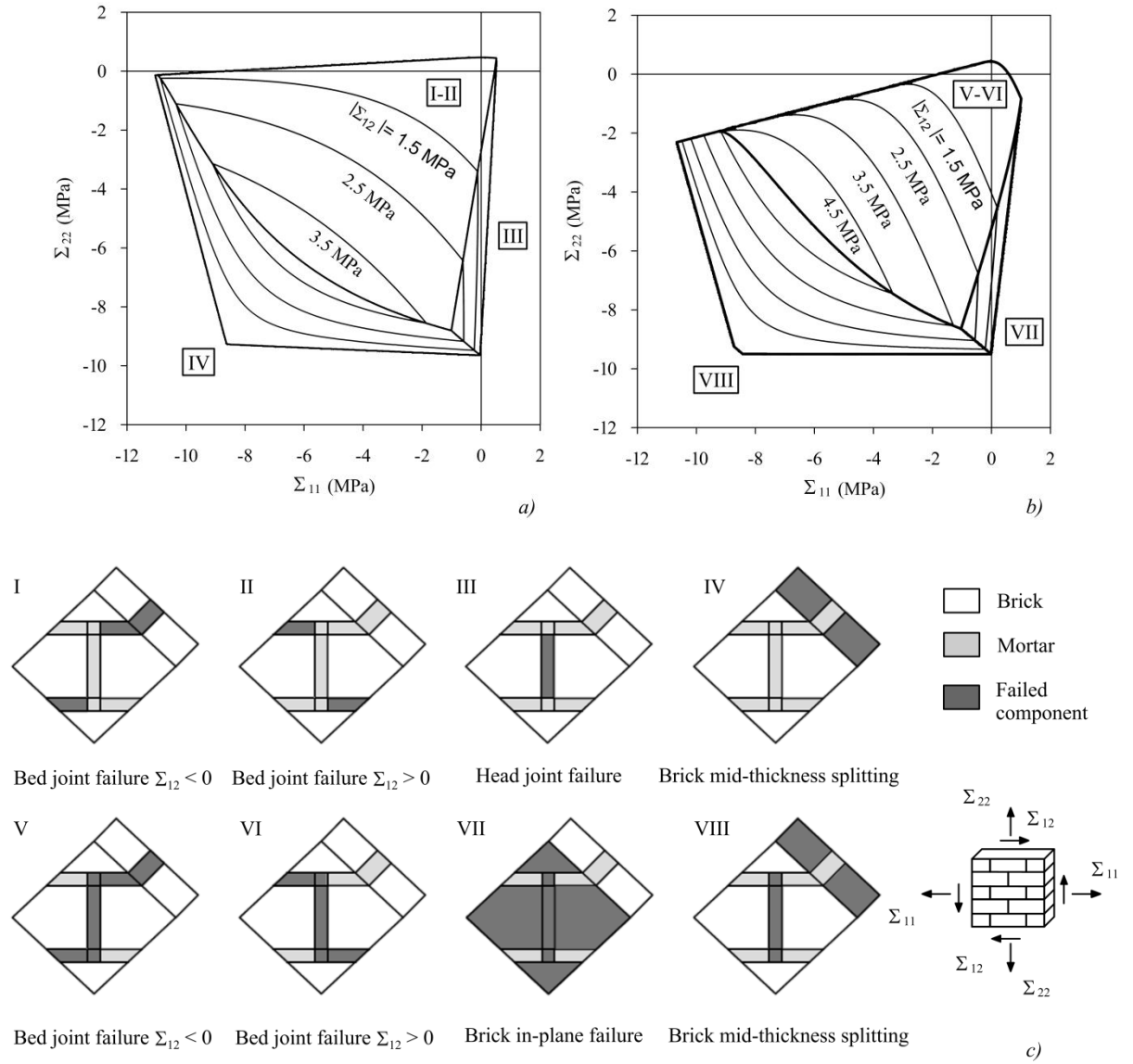


Figure 4.15 Limit elastic domain of masonry with iso-shear stress lines plotted in the space of the macroscopic stress Σ_{11} - Σ_{22} - Σ_{12} considering the head joint filled (a) and unfilled (b) together with abacus of the failure modes (c).

Please note that the boundary of the domain is made of a set of surfaces each corresponding to a failure mode. Failure of the bed joints (modes I-II, Figure 4.15c) is predominant when shear is combined with low biaxial confinement, as well as under biaxial tension regime; cracking of the head joint (mode III, Figure 4.15c) takes places under horizontal traction combined with vertical compression. Out-of-plane splitting of the bricks (mode IV, Figure 4.15c) is encountered under biaxial compression combined with low shear stress. These failure modes are in agreement with the experimental evidence except the head joint failure that usually does not correspond to a failure condition for the overall material since the system is still able to equilibrate increments of the external load relying on the contribution of the bed joints and of the bricks.

In order to evaluate the influence of the vertical joint on the failure of masonry, the limit elastic domain was evaluated also considering the latter joint as unfilled, Figure 4.15b. This assumption is obtained by neglecting the contribution of the head joint to the macroscopic strain energy density, which affects the definition of both the elasticity and stress localization tensors. A remarkable change of the resulting limit elastic domain is obtained, unlike the two step-homogenization approach where only a marginal effect of the head joint is detected, Pietruszczak and Niu (1992). The most important difference, compared to the condition of filled vertical joint, is found under vertical compression combined with horizontal traction, where cracks develop in the bricks along the Oe_1e_2 plane (mode VII, Figure 4.15c). The latter mode of failure is in agreement with the experimental tests in which a progressive failure that envisages firstly the opening of the head joint (mode III Figure 4.15a) then the failure of the material due to cracking of the bricks (mode VII Figure 4.15b) is encountered. Clearly, this progressive crack development may be reproduced only by introducing non-linear constitutive relationships for brick and mortar, which is outside the scope of the present chapter.

Comparison with experimental tests from literature

The most complete set of experimental data carried out to investigate the in-plane behaviour of masonry are from Page (1981,1983) who tested 112 half-scale panels of solid bricks and submitted to proportional biaxial loading. The bricks measure $110 \times 50 \times 35 \text{ mm}^3$ and are separated by mortar head and bed joints 10 mm thick. In order to derive the macroscopic limit elastic domain, a Mohr-Coulomb criterion was assumed for mortar and brick considering a tensile strength f_t of about 1/10 of the compressive strength f_c , being the latter provided by the author (Table 4.2).

Mortar

$$Y_m = 3900 \text{ MPa}^a \quad v_m = 0.25^a \quad t_m = 10 \text{ mm} \quad t_h = 10 \text{ mm} \quad f_c = 5.08 \text{ MPa}$$

$$f_t = 0.5 \text{ MPa}^a$$

Brick

$$Y_b = 6600 \text{ MPa}_a \quad v_b = 0.20_a \quad h_b = 35 \text{ mm} \quad l_b = 110 \text{ mm} \quad f_c = 15.45 \text{ MPa}$$

$$f_t = 1.2 \text{ MPa}_a$$

a: Values assumed in the present work.

Table 4.2 Properties of masonry constituents adopted for reproducing the experimental data from Page (1985).

The elastic moduli of the phases were defined such as to fit the overall elastic properties measured on masonry panels during the tests and reported by Dhanasekar *et al.* (1982), Table 4.3. The limit elastic domain obtained applying the proposed procedure for both plane stress (PS) and generalized plane strain (GPS) conditions is compared in Figure 4.16 with the experimental data.

Measured elastic constants

$$Y_{11}^{hom} = 5700 \text{ MPa} \quad Y_{22}^{hom} = 5600 \text{ MPa} \quad \mu_{12}^{hom} = 2350 \text{ MPa} \quad v_{12}^{hom} = 0.19$$

Predicted elastic constants

$$Y_{11}^{hom} = 5772 \text{ MPa} \quad Y_{22}^{hom} = 5651 \text{ MPa} \quad \mu_{12}^{hom} = 2283 \text{ MPa} \quad v_{12}^{hom} = 0.21$$

a: Values assumed in the present work.

Table 4.3 Comparison between the elastic constants measured on masonry panel Danasekar *et al.* (1982) and the elastic constants predicted introducing in the proposed model the properties of the constituents reported in Table 4.2.

The limit elastic domain provided by the present approach under GPS condition agree reasonably well with experimental data. On the contrary the PS assumption gives reliable results only in the case of low compressive stresses since it is unable to capture the transition from the in-plane to the out-of-plane failure mode under biaxial compression, as already shown by Anthoine (1997) and Massart *et al.* (2005).

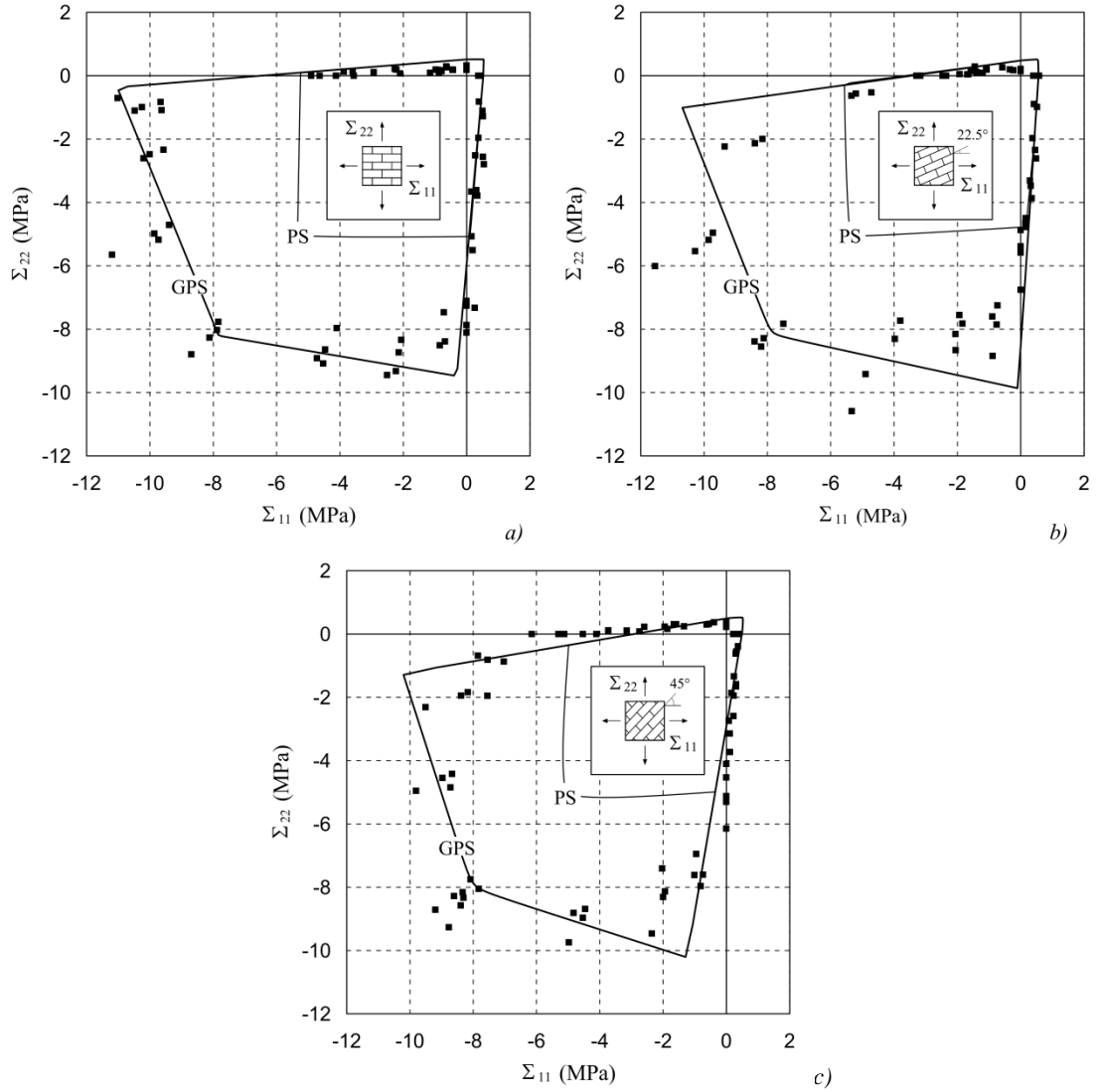


Figure 4.16 Homogenized limit elastic domain evaluated in plane stress (PS) and generalized plane strain (GPS) conditions versus the experimental data from Page (1981,1983). Angles between principal stresses Σ_{11} - Σ_{22} and bed joint orientations 0° (a), 22.5° (b) and 45° (c).

5. A multi-scale approach for the analysis of masonry in the non linear range.

Experimental evidences show that masonry behaviour may deviates from linearity even for low levels of the applied load. As a consequence, when studying the behaviour of real structures, linear elastic analyses are of limited applicability and non linear strategies may be required for reproducing the response under both severe and serviceability load conditions.

Bearing in mind that the use of micro-modelling strategies is precluded in this context, the attention of the technical community focused on the development of equivalent continuum models able to capture the behaviour of masonry beyond the elastic limit. Among the different strategies proposed in the literature, the multi-scale approach based on the homogenization theory became increasing popular in the last ten years. The latter strategy, is based on the identification of two scales, which, in the case at hand, are the macroscopic scale, pertaining to the dimensions of the whole structure, and the microscopic scale, pertaining to the dimensions of brick and mortar joints. The basic idea consists in handling masonry as an homogeneous medium at the structural scale where relevance is given to macroscopic stress and strain which act on the composite material as a whole. Accordingly, the analysis of the entire structure reduces to a boundary value problem defined in terms of the sole macroscopic quantities. During the analysis the response of the homogeneous medium is derived at each material point by performing a scale transition from the macroscopic to the microscopic level and vice versa. More precisely, according to the homogenization theory, the scale transition is governed by an additional boundary value problem, named of localization, which is defined at the microscopic scale and is attached to a representative volume element of masonry where mortar and brick are accounted for as separate entities.

Within this ambit, different strategies have been proposed in the literature which solve the localization problem by resorting to the finite element method. The latter approach, while able to capturing the essential feature of masonry behaviour, Massart *et al.* (2005), is still accompanied by high computational costs when performing analysis on real size structure since for each load step, non linear finite element analyses need to be performed at each material point, *i.e.* at each gauss point if the macroscopic domain is discretized into finite elements. For these reasons, the development of simple and effective techniques

able to solve the nonlinear localization problem received great attention in the technical literature, see Pietruszczak and Niu (1992), Gambarotta and Lagomarsino (1997), Uva and Salerno (2006), Calderini and Lagomarsino (2008), Sacco (2009), Addessi and Sacco (2010), Marfia and Sacco (2011).

The present chapter intends to give a contribution in this direction. A multi-scale algorithm based on the homogenization theory is developed for studying the in-plane behaviour of masonry structures. A micromechanical model is adopted as addressed next: bricks are assumed to exhibit an elastic behaviour and mortar joints are treated as elasto-plastic interfaces obeying to a Mohr-Coulomb yield criteria with non-associative flow rule. A simplified kinematics is introduced over the representative volume element, which makes it possible to express the localization problem in terms of a reduced number of unknowns. An iterative scheme based on Newton-Raphson method is then adopted to solve the latter problem at the microscopic level. The proposed procedure is designed to be implemented into a global incremental-iterative scheme defined at the structural level and thus provides for a prescribed macroscopic strain the respective macroscopic stress and the elasto-plastic tangent operator. Eventually, numerical tests performed on the representative volume element undergoing different macroscopic loading conditions are presented and discussed.

Formulation of the localization problem for the elasto-plastic interface model

Let us consider a wall made of bricks having width l_b and height h_b separated by mortar bed and head joints having thickness t_m and t_h respectively, Figure 5.1a. The vertical joints are staggered within the wall reproducing a running bond pattern. Since the thickness of the joints is usually small when compared to the height of the bricks it is reasonable to model the former by using zero-thickness interface elements, located at joint mid-thickness. A geometrical transformation proves necessary so as to preserve the original geometry of the brickwork. Therefore, an expanded brick is considered, hereafter referred as the unit, that includes a brick and the surrounding half-layers of mortar, Figure 5.1b. Definition of unit height a and length b is trivial:

$$a = h_b + t_m \quad b = l_b + t_h \quad (5.1)$$

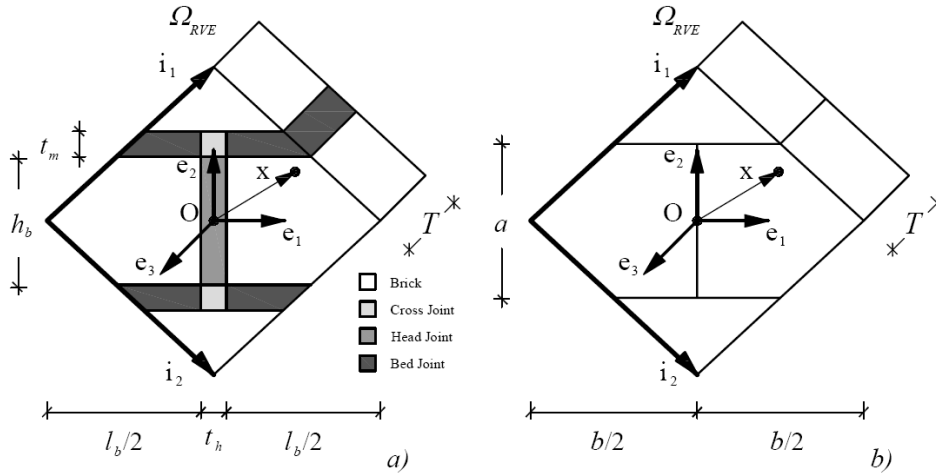


Figure 5.1 Geometrical transformation introduced at the microscopic level: (a) model of joints treated as continuum element and (b) model of joints treated as interfaces.

In these conditions, the full medium may be obtained by repetition of the RVE along the directions of periodicity, defined by the vectors:

$$\mathbf{i}_1 = \mathbf{g}^1 - \mathbf{g}^4 = \frac{b}{2} \mathbf{e}_1 + a \mathbf{e}_2 \quad \mathbf{i}_2 = \mathbf{g}^1 - \mathbf{g}^2 = \frac{b}{2} \mathbf{e}_1 - a \mathbf{e}_2 \quad (5.2)$$

In the above expression, g^i are the vertex of four adjacent bricks Ω^i with $i=1,\dots,4$, (Figure 5.2). The boundary of Ω_{RVE} may be divided into two different regions, $\partial\Omega_{RVE} = \partial\hat{\Omega}_{RVE} \cup \partial\tilde{\Omega}_{RVE}$ and: the former ($\partial\hat{\Omega}_{RVE}$), which is internal to the wall and separates adjacent RVEs, can be divided into pairs of opposite sides, *i.e.* that correspond by periodicity; the latter region ($\partial\tilde{\Omega}_{RVE}$) consists of the boundary of the RVE that lies on the two external faces of the wall which, unlike the previous case, can not be referred to as opposite sides.

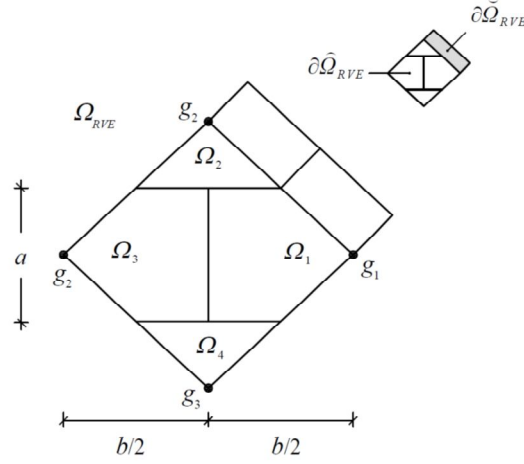


Figure 5.2 Identification of the sub-domains pertaining to the RVE adopted in the present work.

The kinematics of the representative volume element is described in terms of the displacement field $u(x)$ which is continuous within each unit Ω^i and admits jumps of displacement $w^{ij}(x)$ on the boundary between two adjacent units $\partial\Omega^i \cap \partial\Omega^j$:

$$u(x) = u^i(x) \quad \forall x \in \Omega^i \quad i = 1, \dots, 4 \quad (5.3)$$

$$w^{ij}(x) = u^i(x) - u^j(x) \quad \forall x \in \partial\Omega^i \cap \partial\Omega^j \quad i = 1, \dots, 4 \quad (5.4)$$

The unit is assumed to exhibit an elastic behaviour equal to that of the brick and is thus characterized by the elasticity fourth order tensor \mathbf{C}^b :

$$\sigma(x) = \mathbf{C}^b : \varepsilon(x) \quad \forall x \in \Omega^i \quad i = 1, \dots, 4 \quad (5.5)$$

where $\sigma(x)$ and $\varepsilon(x)$ are respectively the stress and strain fields defined over Ω_{REV} .

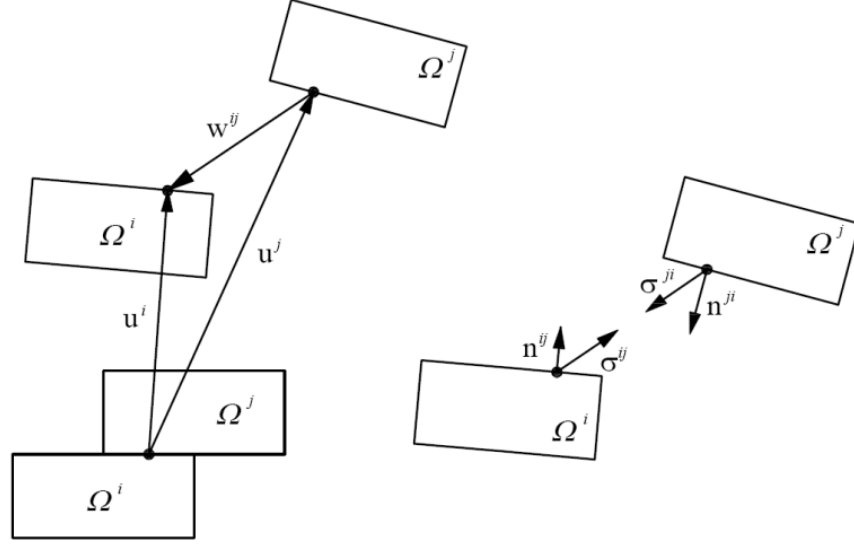


Figure 5.3 Jump of displacement (w^{ij}) and traction (σ^{ij}) acting on the interface.

Noteworthy, the stress field acting within the RVE is continuous. Accordingly, the traction acting on the interface $\sigma^{ij}(x)$ may be expressed in terms of the microscopic stress field acting in the unit $\sigma(x)$ as follows:

$$\sigma^{ij}(x) = \sigma(x) \cdot n^{ij}(x) = -\sigma(x) \cdot n^{ji}(x) \quad \forall x \in \partial\Omega^i \cap \partial\Omega^j \quad (5.6)$$

where n^{ij} and n^{ji} denote the outward normal vectors of the joint corresponding to the border belonging respectively to Ω^i and Ω^j , Figure 5.3.

The joints are assumed to exhibit an elasto-perfect plastic behaviour. Accordingly, the relation between the jump of displacement $w^{ij}(x)$ and the traction $\sigma^{ij}(x)$ acting on the interfaces reads:

$$\sigma^{ij}(x) = K^{ij} \cdot [w^{ij}(x) - w^{ij,p}(x)] \quad \forall x \in \partial\Omega^i \cap \partial\Omega^j \quad i, j = 1, \dots, 4 \quad (5.7)$$

where $w^{ij,p}(x)$ is the plastic jump of displacement and K^{ij} is the elasticity tensor pertaining to the joint, expressed in Eq. (5.8).

$$K^{ij} = K_n n^{ij} \otimes n^{ij} + K_t (t_1^{ij} \otimes t_1^{ij} + t_2^{ij} \otimes t_2^{ij}) \quad (5.8)$$

where t_1^{ij}, t_2^{ij} represent the unitary vectors normal and parallel to the interface $\partial\Omega^i \cap \partial\Omega^j$ and K_n, K_t are respectively the normal and tangential stiffness which are assumed equal for the whole set of joints.

The non linear behaviour of the joints is governed by the yield criterion $F[\sigma^{ij}]$ delimiting a convex set of admissible traction, *i.e.* which fulfils the following condition:

$$F[\sigma^{ij}] \leq 0 \quad (5.9)$$

The evolution of plastic strain $w^{ij,p}$ is controlled by a non-associated flow rule driven by the plastic potential $G[\sigma^{ij}]$:

$$\dot{w}^{ij,p} = \dot{\gamma}^{ij} \frac{\partial G[\sigma^{ij}]}{\partial \sigma^{ij}} \quad (5.10)$$

In the above relation $\dot{\gamma}^{ij} \geq 0$ is the plastic multiplier and is subject to the so-called Kuhn-Tucker complementary condition and to the consistency condition:

$$\dot{\gamma}^{ij} F[\sigma^{ij}] = 0, \quad \dot{\gamma}^{ij} \dot{F}[\sigma^{ij}] = 0 \quad (5.11)$$

In analogy with the previous chapter, let us consider as a domain of reference a masonry wall loaded along its middle plane. Bearing in mind that the latter assumption correspond to a plane stress condition from the macroscopic point of view, Eq. (4.5), the derivation of the response of masonry seen as an homogeneous medium is equivalent to define the relation between macroscopic stress Σ and strain E given by:

$$\Sigma = \langle \sigma(x) \rangle = \frac{1}{\Omega_{RVE}} \int_{\Omega_{RVE}} \sigma(x) d\Omega \quad (5.12)$$

$$E = \langle \varepsilon(x) \rangle = \frac{1}{\Omega_{RVE}} \int_{\Omega_{RVE}} \varepsilon(x) d\Omega \quad (5.13)$$

According to the homogenization theory of periodic medium, the latter issue can be achieved by solving the localization problem, which, in the case at hand and for a prescribed macroscopic strain E , reads:

$$\text{div } \sigma(x) = 0 \quad \forall x \in \Omega_{REV} \quad (5.14)$$

$$\sigma(x) \cdot n(x) \quad \text{anti-periodic on opposite sides of } \partial\tilde{\Omega}_{RVE} \quad (5.15)$$

$$\sigma(x) \cdot n(x) = 0 \quad \text{on } \partial\tilde{\Omega}_{RVE} \quad (5.16)$$

$$\sigma(\mathbf{x}) = \mathbf{C}^b(\mathbf{x}) : \varepsilon(\mathbf{x}) \quad (5.17)$$

$$\varepsilon(\mathbf{x}) = \text{sym } \nabla \mathbf{u}(\mathbf{x}) \quad (5.18)$$

$$\mathbf{u}(\mathbf{x}) = \mathbf{E} \cdot \mathbf{x} + \hat{\mathbf{u}}(\mathbf{x}) \quad (5.19)$$

$$\hat{\mathbf{u}}(\mathbf{x}) \quad \text{periodic on opposite sides of } \partial\hat{\Omega}_{\text{RVE}} \quad (5.20)$$

$$\mathbf{w}^{ij}(\mathbf{x}) = \mathbf{u}^i(\mathbf{x}) - \mathbf{u}^j(\mathbf{x}) \quad \forall \mathbf{x} \in \partial\Omega^i \cap \partial\Omega^j \quad i, j = 1, \dots, 4 \quad (5.21)$$

$$\sigma^{ij}(\mathbf{x}) = \mathbf{K}^{ij} \cdot [\mathbf{w}^{ij}(\mathbf{x}) - \mathbf{w}^{ij,p}(\mathbf{x})] \quad (5.22)$$

$$F[\sigma^{ij}(\mathbf{x})] \leq 0 \quad (5.23)$$

$$\dot{\mathbf{w}}^{ij,p}(\mathbf{x}) = \dot{\gamma}^{ij} \frac{\partial G[\sigma^{ij}(\mathbf{x})]}{\partial \sigma^{ij}} \quad (5.24)$$

$$\dot{\gamma}^{ij} \geq 0 \quad \dot{\gamma}^{ij} F[\sigma^{ij}] = 0, \quad \dot{\gamma}^{ij} \dot{F}[\sigma^{ij}] = 0 \quad (5.25)$$

By introducing suitable test fields $\hat{\mathbf{u}}^{\text{test}}(\mathbf{x})$, the localization problem may be stated in a weak form as follows:

$$\int_{\Omega_{\text{RVE}}} \sigma(\mathbf{x}, \mathbf{E}) \cdot \nabla \hat{\mathbf{u}}^{\text{test}}(\mathbf{x}) \, d\Omega + \sum_{i,j=1}^4 \int_{\partial\Omega^i \cap \partial\Omega^j} \sigma^{ij}(\mathbf{x}, \mathbf{E}) \cdot \hat{\mathbf{w}}^{ij,\text{test}}(\mathbf{x}) \, d\mathbf{x} = 0 \quad \forall \hat{\mathbf{u}}^{\text{test}}(\mathbf{x}) \in \mathbf{V}_{\text{per}}$$

$$\mathbf{V}_{\text{per}} = \left\{ \hat{\mathbf{u}}(\mathbf{x}) \in \mathbf{H}^1(\Omega^i) \mid \begin{array}{l} \hat{\mathbf{u}}(\mathbf{x}) \text{ is periodic on } \partial\hat{\Omega}_{\text{RVE}} \\ \langle \hat{\mathbf{u}}(\mathbf{x}) \rangle = 0 \end{array} \right\}$$

$$\hat{\mathbf{w}}^{ij,\text{test}}(\mathbf{x}) = \hat{\mathbf{u}}^{i,\text{test}}(\mathbf{x}) - \hat{\mathbf{u}}^{j,\text{test}}(\mathbf{x}) \quad \forall \mathbf{x} \in \partial\Omega^i \cap \partial\Omega^j \quad (5.26)$$

$\sigma^{ij}(\mathbf{x}, \mathbf{E})$ fulfilling Eqs. (5.20-5.23)

$\sigma(\mathbf{x}, \mathbf{E})$ fulfilling Eqs. (5.13-5.14)

\mathbf{E} given

where \mathbf{V}_{per} and $\mathbf{H}^1(\Omega^i)$ denote the space of periodic displacement fields and a Sobolev space defined over Ω^i , respectively.

A simplified kinematics for the Representative

Volume Element

In order to obtain an approximate solution of the localization problem, Eq.(5.26), simplifying assumptions are made concerning the kinematics within the representative volume element. Similarly to the approach followed in the previous chapter, the fluctuating part of the displacement field $\hat{u}(x)$ is approximated by a piecewise function, defined within each sub-domain Ω^i as:

$$\hat{u}(x) = \hat{u}(g^i) + H^i \cdot (x - g^i) \quad \forall x \in \Omega^i \quad i = 1, \dots, 4 \quad (5.27)$$

where g^i are the centre of each sub-domain, as depicted in Figure 5.2, and H^i is a second order tensor.

In order to express explicitly the restrictions on the kinematics deriving from the periodicity conditions, let us consider two homologue points $p^i \in \partial\Omega^i$ and $p^j \in \partial\Omega^j$ that belong to the boundary $\partial\Omega_{RVE}$ and correspond each other by periodicity, that is:

$$p^i - p^j = m_1 i_1 + m_2 i_2 \quad (5.28)$$

where i_1 and i_2 are the directions of periodicity, Eq. (5.1), and m_1, m_2 are integer coefficients in the range $[-1, 1]$. It is worth noting that the centres g^i and g^j of the domains Ω^i and Ω^j are homologues too and fulfil the following condition:

$$p^i - p^j = g^i - g^j \quad (5.29)$$

According to Eq. (5.27), the relative displacement between points p^i and p^j reads:

$$\hat{u}(p^i) - \hat{u}(p^j) = \hat{u}(g^i) - \hat{u}(g^j) + (H^i - H^j) \cdot (p^i - p^j) \quad (5.30)$$

Moreover, according to the periodicity of the fluctuating displacement field $\hat{u}(x)$, Eq.(5.20), the quantities $\hat{u}(p^i) - \hat{u}(p^j)$ and $\hat{u}(g^i) - \hat{u}(g^j)$ vanish, meaning that $H^i = H^j$. Following the same reasoning for all the couples of points that fulfil Eq. (5.30), it is straightforward to prove that the restrictions on the kinematics given by the periodicity conditions reduce to:

$$H^i = H \quad i = 1, \dots, 4 \quad (5.31)$$

According to the above expression, no relative rotation and no independent deformation of the units is admitted if periodicity is imposed. It is straightforward to prove that the jump of displacement \hat{w}^{ij} along the interface

between two adjacent units is given by:

$$\hat{w}^{ij}(x) = -H: (g^i - g^j) \quad \forall x \in \partial\Omega^i \cap \partial\Omega^j \quad i, j = 1, 2, 3, 4 \quad (5.32)$$

Noteworthy, because of the periodicity condition, it is possible to identify two pairs of joints which correspond by periodicity:

$$\hat{w}^{12} = -\hat{w}^{34} \quad (5.33)$$

$$\hat{w}^{23} = -\hat{w}^{41} \quad (5.34)$$

From tensor to Voigt notation

According to the kinematics assumptions made, the stress within the unit and the jump of displacement along each interface belonging to the representative volume elements are constant. Owing to the symmetry of the problem under consideration, *i.e.* a wall in-plane loaded, the out-of-plane shear components σ_{i3} with $i = 1, 2$ acting within the unit vanish. Furthermore, since the interface model does not account for the thickness of the joint, the component σ_{33} vanishes too. Accordingly, the problem can be stated in a plane stress condition both from a macroscopic and microscopic point of view. At this stage, it is convenient to adopt a Voigt-type notation as explained next, where the non null components of microscopic fields are collected into vectors:

$$\sigma = \{ \sigma_{11} \quad \sigma_{22} \quad \tau_{12} \}^T \quad (5.35)$$

$$\varepsilon = \{ \varepsilon_{11} \quad \varepsilon_{22} \quad \gamma_{12} \}^T \quad (5.36)$$

$$H = \{ H_{11} \quad H_{22} \quad H_{12} \quad H_{21} \}^T \quad (5.37)$$

$$w^{ij} = \{ w_1^{ij} \quad w_2^{ij} \}^T \quad (5.38)$$

$$\sigma^{ij} = \{ \sigma_1^{ij} \quad \sigma_2^{ij} \}^T \quad (5.39)$$

where H , σ and ε represent the gradient of displacement, the stress and strain pertaining to the unit and w^{ij} and σ^{ij} are the jump of displacement and the traction acting on the generic interface separating Ω^i and Ω^j .

The same applies to the macroscopic strain:

$$\mathbf{E} = \{ E_{11} \quad E_{22} \quad E_{12} \}^T \quad (5.40)$$

The constitutive relation of the unit in terms of the Lamé's constants λ^b, μ^b writes:

$$\boldsymbol{\sigma} = \mathbf{C}^b \cdot \boldsymbol{\varepsilon} \quad \text{with} \quad \mathbf{C}^b = \begin{bmatrix} \lambda^b + 2\mu^b & \lambda^b & 0 \\ \lambda^b & \lambda^b + 2\mu^b & 0 \\ 0 & 0 & \mu^b \end{bmatrix} \quad (5.41)$$

The relation between the gradient of displacement and the deformation of the unit, Eqs. (5.18), (5.19), reads:

$$\boldsymbol{\varepsilon} = \mathbf{E} + \mathbf{M}_s \cdot \mathbf{H} \quad \text{with} \quad \mathbf{M}_s = \begin{bmatrix} 1 & 0 & 0 & 0 \\ 0 & 1 & 0 & 0 \\ 0 & 0 & 1 & 1 \end{bmatrix} \quad (5.42)$$

The jump of displacement on the interface may be expressed as a linear application to the gradient of displacement of the unit, Eq. (5.32), which reads:

$$\hat{\mathbf{w}}^{ij}(\mathbf{x}) = \mathbf{A}^{ij} \cdot \mathbf{H} \quad \forall \mathbf{x} \in \partial\Omega^i \cap \partial\Omega^j \quad i, j = 1, 2, 3, 4 \quad (5.43)$$

where matrixes \mathbf{A}^{ij} assume the following expressions:

$$\mathbf{A}^{12} = -\mathbf{A}^{43} = \begin{bmatrix} -\frac{b}{2} & 0 & a & 0 \\ 0 & a & 0 & -\frac{b}{2} \end{bmatrix} \quad (5.44)$$

$$\mathbf{A}^{23} = -\mathbf{A}^{14} = \begin{bmatrix} \frac{b}{2} & 0 & a & 0 \\ 0 & a & 0 & \frac{b}{2} \end{bmatrix} \quad (5.45)$$

$$\mathbf{A}^{13} = \begin{bmatrix} -b & 0 & 0 & 0 \\ 0 & 0 & 0 & -b \end{bmatrix} \quad (5.46)$$

The kinematics restrictions adopted in the previous paragraph allow us to recast the weak formulation expressed by Eq. (5.26). The Galerkin method is adopted, according to which the test functions are assumed to have the same

shape of the field $\hat{\mathbf{u}}(\mathbf{x})$ as expressed by Eq. (5.27). According to the Voigt-type notation presented and exploiting Eqs. (5.31)-(5.34) the weak formulation of the localization problem reads:

$$\Omega_{RVE} \sigma(\mathbf{E})^T \cdot \mathbf{M}_S \cdot \mathbf{H}^{test} + \sum_{i,j=1}^4 l^{ij} \sigma^{ij}(\mathbf{E})^T \cdot \mathbf{A}^{ij} \cdot \mathbf{H}^{test} = 0 \quad \forall \mathbf{H}^{test}(\mathbf{x}) \in \mathbb{R}^4 \quad (5.47)$$

$$\begin{aligned} \hat{\mathbf{w}}^{test}(\mathbf{x}) &= \hat{\mathbf{u}}^{test,i}(\mathbf{x}) - \hat{\mathbf{u}}^{test,j}(\mathbf{x}) \quad \forall \mathbf{x} \in \partial\Omega^i \cap \partial\Omega^j \\ \sigma^{ij}(\mathbf{x}, \mathbf{E}) &\text{ fulfilling Eqs. (5.20-5.23)} \\ \sigma(\mathbf{x}, \mathbf{E}) &\text{ fulfilling Eqs. (5.13-5.14)} \end{aligned} \quad (5.48)$$

which may be simplified in the following system of four equations:

$$\Omega_{RVE} \sigma(\mathbf{E})^T \mathbf{M}_S + \sum_{i,j=1}^4 l^{ij} \sigma^{ij}(\mathbf{E})^T \cdot \mathbf{A}^{ij} = 0 \quad (5.49)$$

where l^{ij} represents the length of the generic interface $\partial\Omega^i \cap \partial\Omega^j$.

Multi-Scale algorithm

The simplified weak formulation obtained for the localization problem makes it possible to define a simple multi-scale algorithm which proves particular attractive for the implementation into general purpose finite element programs.

Let us consider a generic material point of the structure under consideration, which undergoes a prescribed strain history $\mathbf{E}(t)$ defined within the time interval $[t_0, t_f]$. The aim is to derive the response of the material in terms of the macroscopic stress history $\Sigma(t)$.

To this purpose, an incremental approach is adopted, which consists in subdividing the time domain in discrete increments Δt . Let us refer to the strain increment $\Delta \mathbf{E}_n$ assigned to a generic time t_n belonging to $[t_0, t_f]$, for which all the state variables are known, *i.e.* $\mathbf{w}_n^{ij,p}, \mathbf{H}_n, \mathbf{E}_n$. The purpose is to derive the response of the homogeneous material at the time $t_{n+1} = t_n + \Delta t$ in terms of the macroscopic stress Σ_{n+1} .

The localization problem expressed by Eq. (5.49) is thus solved in terms of \mathbf{H}_{n+1} and $\mathbf{w}_{n+1}^{ij,p}$ by means of an iterative Newton's scheme as addressed next.

1. For the first iteration ($k = 1$) let us assume that all the state variables are frozen except the strain of the brick which is incremented by ΔE_n :

$$\begin{aligned} H_{n+1}^{(k=1)} &= H_n \\ \varepsilon_{n+1}^{(k=1)} &= \varepsilon_n + \Delta E_n \\ w_{n+1}^{ij(k=1)} &= w_n^{ij} \end{aligned} \quad (5.50)$$

2. The response of the brick is evaluated by resorting to Eq. (5.5):

$$\sigma_{n+1}^{(k)} = C^b \cdot \varepsilon_{n+1}^{(k)} \quad (5.51)$$

3. The response of the joint is evaluated by integrating the elasto-plastic constitutive relation Eqs. (5.23)-(5.25) which provides the traction $\sigma_{n+1}^{ij(k)}$ and the tangent moduli $\tilde{K}_{n+1}^{ij(k)}$:

$$\begin{aligned} \sigma_{n+1}^{ij(k)} &= K^{ij} (w_{n+1}^{ij(k)} - w_{n+1}^{ij,p(k)}) \\ \tilde{K}_{n+1}^{ij(k)} &= \frac{\partial \sigma_{n+1}^{ij(k)}}{\partial w_{n+1}^{ij}} \end{aligned} \quad (5.52)$$

4. The residual is evaluated starting from Eq. (5.49):

$$R_{n+1}^{(k)} = \mathcal{Q}_{RVE} \sigma_{n+1}^{(k)T} M_s + \sum_{i,j=1}^4 l^{ij} \sigma_{n+1}^{ij(k)T} \cdot A^{ij} \quad (5.53)$$

5. If the modulus of the residual $\|R_{n+1}^{(k)}\|$ is higher than the tolerance accepted for convergence, the solution of the problem needs to be updated and the procedure is restarted from point 2:

$$\begin{aligned} \Delta H_{n+1}^{(k)} &= -[J_{n+1}^k]^{-1} \cdot R_{n+1}^{(k)} \\ H_{n+1}^{(k+1)} &= H_{n+1}^{(k)} + \Delta H_{n+1}^{(k)} \\ \varepsilon_{n+1}^{(k+1)} &= \varepsilon_{n+1}^{(k)} + M_s \cdot \Delta H_{n+1}^{(k)} \\ w_{n+1}^{ij(k+1)} &= w_{n+1}^{ij(k)} + A^{ij} \cdot \Delta H_{n+1}^{(k)} \end{aligned} \quad (5.54)$$

6. When the modulus of the residual $\| \mathbf{R}_{n+1}^{(k)} \|$ is lower than the tolerance accepted for convergence, the solution of the localization problem is obtained. The macroscopic stress Σ_{n+1} can be evaluated by resorting to Eq. (5.12) which, standing the simplifications introduced for the kinematics of the representative volume elements, reduces to:

$$\Sigma_{n+1} = \langle \sigma_{n+1}(\mathbf{x}) \rangle = \sigma_{n+1} \quad (5.55)$$

The Jacobian matrix needed for solving the localization problem is evaluated as addressed next.

$$\begin{aligned} \mathbf{J}_{n+1}^{(k)} &= \left[\frac{\partial \mathbf{R}}{\partial \mathbf{H}} \right]_{n+1}^{(k)} = \frac{\partial}{\partial \mathbf{H}} \left(\mathcal{Q}_{RVE} \cdot \sigma_{n+1}^{(k)T} \mathbf{M}_S + \sum_{i,j=1}^4 l^{ij} \sigma_{n+1}^{ij(k)T} \cdot \mathbf{A}^{ij} \right) \\ &= \mathcal{Q}_{RVE} \cdot \left[\frac{\partial \sigma}{\partial \varepsilon} \cdot \frac{\partial \varepsilon}{\partial \mathbf{H}} \right]_{n+1}^{(k)T} \cdot \mathbf{M}_S + \sum_{i,j=1}^4 l^{ij} \left[\frac{\partial \sigma_{n+1}^{ij}}{\partial \mathbf{w}_{n+1}^{ij}} \cdot \frac{\partial \mathbf{w}_{n+1}^{ij}}{\partial \mathbf{H}} \right]_{n+1}^{(k)T} \cdot \mathbf{A}^{ij} \end{aligned} \quad (5.56)$$

The latter expression can be simplified by introducing Eqs. (5.10):

$$\mathbf{J}_{n+1}^{(k)} = \mathcal{Q}_{RVE} \mathbf{M}_S^T \cdot \mathbf{C}^b \cdot \mathbf{M}_S + \sum_{i,j=1}^4 l^{ij} \mathbf{A}^{ijT} \cdot \tilde{\mathbf{K}}_{n+1}^{ij(k)} \cdot \mathbf{A}^{ij} \quad (5.57)$$

As an alternative to use of the updated Jacobian $\mathbf{J}_{n+1}^{(k)}$, the solution may be found by using an approximation of Eq. (5.57), for instance by using the Jacobian evaluated by considering the elastic behaviour of the components.

Derivation of the elasto-plastic tangent moduli

A tangent operator consistent with the integration algorithm is needed to improve the rate of convergence of the incremental - iterative scheme adopted at the macroscopic level. Bearing in mind that a single surface yield criterion is adopted for the joints, let us consider the total variation of the stress acting within the brick and within the interfaces:

$$d\sigma_{n+1} = \mathbf{C}^b \cdot \left(d\mathbf{E}_{n+1} + \mathbf{M}_s \cdot \left[\frac{d\mathbf{H}}{d\mathbf{E}} \right]_{n+1} \cdot d\mathbf{E}_{n+1} \right) \quad (5.58)$$

$$d\sigma_{n+1}^{ij} = K^{ij} \cdot \left(A^{ij} \cdot \left[\frac{dH}{dE} \right]_{n+1} \cdot dE_{n+1} - d\gamma_{n+1}^{ij} \left[\frac{\partial G^{ij}}{\partial \sigma^{ij}} \right] \right) \quad (5.59)$$

where γ^{ij} and G^{ij} are defined in Eq. (5.24) and represent the plastic multiplier and the plastic potential of the joint $\partial\Omega^i \cap \partial\Omega^j$. The consistency conditions expressed by Eq. (5.25) reads:

$$dF_{n+1}^{ij} = \left[\frac{\partial F^{ij}}{\partial \sigma^{ij}} \right]^T \cdot d\sigma_{n+1}^{ij} = 0 \quad (5.60)$$

Upon substitution of Eq. (5.59) into the above expression one obtains

$$d\gamma_{n+1}^{ij} = \frac{\left[\frac{\partial F^{ij}}{\partial \sigma^{ij}} \right]^T \cdot K^{ij}}{\left[\frac{\partial F^{ij}}{\partial \sigma^{ij}} \right]^T \cdot K^{ij} \cdot \left[\frac{\partial G^{ij}}{\partial \sigma^{ij}} \right]^T} \cdot A^{ij} \cdot \left[\frac{dH}{dE} \right]_{n+1} \cdot dE_{n+1} \quad (5.61)$$

Accordingly, Eq. (5.59) may be rewritten as:

$$d\sigma_{n+1}^{ij} = K^{ij} \left(I - \frac{\left[\frac{\partial G^{ij}}{\partial \sigma^{ij}} \right] \otimes \left[\frac{\partial F^{ij}}{\partial \sigma^{ij}} \right]^T \cdot K^{ij}}{\left[\frac{\partial F^{ij}}{\partial \sigma^{ij}} \right]^T \cdot K^{ij} \cdot \left[\frac{\partial G^{ij}}{\partial \sigma^{ij}} \right]^T} \right) \cdot A^{ij} \cdot \left[\frac{dH}{dE} \right]_{n+1} \cdot dE_{n+1} \quad (5.62)$$

where introducing the elasto-plastic stiffness tensor defined for the joint \tilde{K}_{n+1}^{ij} one would obtain:

$$d\sigma_{n+1}^{ij} = \tilde{K}_{n+1}^{ij} \cdot A^{ij} \cdot \left[\frac{dH}{dE} \right]_{n+1} \cdot dE_{n+1} \quad (5.63)$$

Let us now exploit the weak formulation obtained for the localization problem by introducing the above expression into Eq. (5.49) which reads:

$$\begin{aligned} dR_{n+1} = \Omega_{RVE} M_s^T \cdot C^b \cdot \left(dE_{n+1} + M_s \cdot \left[\frac{dH}{dE} \right]_{n+1} \cdot dE_{n+1} \right) \\ + \sum_{i,j=1}^4 l^{ij} A^{ijT} \cdot \tilde{K}_{n+1}^{ij} \cdot A^{ij} \cdot \left[\frac{dH}{dE} \right]_{n+1} \cdot dE_{n+1} = 0 \end{aligned} \quad (5.64)$$

By solving the equation with respect to $\left[\frac{dH}{dE} \right]_{n+1}$ one would obtain:

$$\left[\frac{dH}{dE} \right]_{n+1} = -\Omega_{RVE} [J_{n+1}]^{-1} \cdot M_s^T \cdot C^b \quad (5.65)$$

Since the microscopic stress acting within the unit corresponds to the macroscopic stress acting on the whole RVE, Eq. (5.55), the tangent moduli of masonry as an homogeneous material \tilde{C}_{n+1} can be obtained by introducing the latter expression into Eq. (5.58):

$$\tilde{C}_{n+1} = \left[\frac{d\Sigma}{dE} \right]_{n+1} = \left[\frac{d\sigma}{dE} \right]_{n+1} = C^b \cdot \left(I + M_c \left[\frac{dH}{dE} \right]_{n+1} \right) \quad (5.66)$$

In the specific case in which the whole sets of joints provides a null tangent operator it follows from Eq. (5.64) that:

$$\begin{aligned} dR_{n+1} &= \Omega_{RVE} M_s^T \cdot C^b \cdot \left(dE_{n+1} + M_s \cdot \left[\frac{dH}{dE} \right]_{n+1} \cdot dE_{n+1} \right) = 0 \\ dE_{n+1} + M_s \cdot \left[\frac{dH}{dE} \right]_{n+1} \cdot dE_{n+1} &= 0 \Rightarrow I + M_s \cdot \left[\frac{dH}{dE} \right]_{n+1} = 0 \end{aligned} \quad (5.67)$$

and consequently according to Eq. (5.66) the tangent operator of masonry \tilde{C}_{n+1} is null. For instance, by referring to a Mohr-Coulomb criteria, the latter condition correspond to the case in which the stresses within all the joints reach the apex.

Discussion and validation of the results

The multi-scale procedure presented makes it possible to reproduce in a rather simple way the response of masonry for strain-driven loads by exchanging information between the macroscopic and microscopic levels.

Under the assumption of elasto-perfect plastic behaviour of the constituents, which is the case under consideration, Suquet (1987) has shown

that the behaviour of the material from the macroscopic view point is characterized by a strain hardening effect. The latter phenomenon is related to the residual stresses, *i.e.* self equilibrated states of stress, that arise at the microscopic scale when plastic strains start to develop within the components.

Standing the considerations made above, it is possible to identify three different stages of masonry behaviour when the homogenization technique is applied. In the first stage the material is elastic. For increasing levels of load one or more components reach the limit condition and start to develop plastic strain. The behaviour of the material becomes plastic and shows strain hardening related to the development of residual stresses. Finally when all the components achieve the limit conditions, complete yielding of the homogeneous material is reached and masonry behaves as an elastic perfect plastic material.

Within the elastic range the response of the material is governed by the sole stiffness tensor \mathbf{C}^{hom} and the relation between macroscopic stress and strain reads:

$$\Sigma = \mathbf{C}^{\text{hom}} \cdot \mathbf{E} \quad (5.68)$$

An analytical expression for the stiffness tensor can be obtained by adopting the proposed approach. More precisely, in the case at hand, the macroscopic elastic strain energy $W(\mathbf{E})$ assumes the following explicit form:

$$2W(\mathbf{E}) = \frac{Y_{11}^{\text{hom}} \cdot E_{11}^2}{1 - \nu_{12}^{\text{hom}} \nu_{21}^{\text{hom}}} + \frac{Y_{22}^{\text{hom}} \cdot E_{22}^2}{1 - \nu_{12}^{\text{hom}} \nu_{21}^{\text{hom}}} + \frac{2\nu_{21}^{\text{hom}} Y_{22}^{\text{hom}}}{1 - \nu_{12}^{\text{hom}} \nu_{21}^{\text{hom}}} E_{11} E_{22} + 4\mu_{12}^{\text{hom}} E_{11}^2 \quad (5.69)$$

where the four elastic constants introduced ($Y_{11}^{\text{hom}}, Y_{22}^{\text{hom}}, \nu_{12}^{\text{hom}}, \mu_{12}^{\text{hom}}$) may be written in terms of the properties of the joints (K_n, K_t) and of the blocks (a, b, λ_b, μ_b) as follows:

$$\frac{1}{Y_{11}^{\text{hom}}} = \frac{4a}{4abK_n + b^2K_t} + \frac{\lambda_b + 2\mu_b}{\mu_b(3\lambda_b + 2\mu_b)} \quad (5.70)$$

$$\frac{1}{Y_{22}^{\text{hom}}} = \frac{1}{aK_n} + \frac{\lambda_b + 2\mu_b}{\mu_b(3\lambda_b + 2\mu_b)} \quad (5.71)$$

$$\frac{\nu_{21}^{\text{hom}}}{Y_{11}^{\text{hom}}} = -\frac{\lambda_b}{\mu_b(6\lambda_b + 4\mu_b)} \quad (5.72)$$

$$\frac{1}{\mu_{12}^{\text{hom}}} = \frac{1}{aK_t} + \frac{4b}{b^2K_n + 4abK_t} + \frac{1}{\mu_b} \quad (5.73)$$

Noteworthy, the elastic constants obtained are the superimposition of the ones found by de Felice (1995) for the case of rigid blocks connected by interfaces and the elasticity tensor of the unit.

Additionally, it is possible to obtain analytically the relations of stress localization, *i.e.* the relations that yield the microscopic stress field σ for a given macroscopic stress Σ . Bearing in mind that, according to the simplified kinematics adopted, the stresses acting within the components are constant, the relations of stress localization write:

$$\begin{aligned}\sigma &= \Sigma \\ \sigma^{13} &= \left[\frac{4abK_n}{4abK_n + b^2K_t} \Sigma_{11}, \frac{4abK_t}{b^2K_n + 4abK_t} \Sigma_{12} \right] \\ \sigma^{12} = -\sigma^{34} &= \left[\Sigma_{12} - \frac{2abK_t}{4abK_n + b^2K_t} \Sigma_{11}, \Sigma_{22} - \frac{2abK_n}{b^2K_n + 4abK_t} \Sigma_{12} \right] \\ \sigma^{23} = -\sigma^{41} &= \left[-\Sigma_{12} - \frac{2abK_t}{4abK_n + b^2K_t} \Sigma_{11}, \Sigma_{22} + \frac{2abK_n}{b^2K_n + 4abK_t} \Sigma_{12} \right]\end{aligned}\quad (5.74)$$

The behaviour of the homogeneous material is linear until one of the interfaces starts to yield, which is:

$$F(\sigma^{ij}) = 0 \quad i, j = 1, \dots, 4 \quad (5.75)$$

Let us assume for the whole set of joints a Mohr-Coulomb yield criterion, which in the case at hand reads:

$$\begin{aligned}F(\sigma^{ij}) &= v^T \sigma^{ij} - c \\ v &= \mu n^{ij} + \text{sign}(\sigma^{ijT} \cdot t^{ij}) t^{ij} \quad i, j = 1, \dots, 4\end{aligned}\quad (5.76)$$

while the plastic potential adopted in the present work assumes the following expression:

$$\begin{aligned}G(\sigma^{ij}) &= d^T \sigma^{ij} - c = 0 \\ d &= \psi n^{ij} + \text{sign}(\sigma^{ijT} \cdot t^{ij}) t^{ij} \quad i, j = 1, \dots, 4\end{aligned}\quad (5.77)$$

where n^{ij} and t^{ij} are the normal and tangential vector of the interface while μ , ψ and c are the coefficient of friction, the coefficient of the dilatancy and the cohesion, respectively. By exploiting Eqs. (5.74)-(5.76) it is possible to obtain an analytical expression for the limit elastic domain of the material defined as the set of macroscopic stress inducing a linear elastic response within the

components. The elastic limit domain proves bounded by a set of surfaces, each of them corresponding to the yielding of one of the interfaces belonging to the RVE, Figure 5.4.

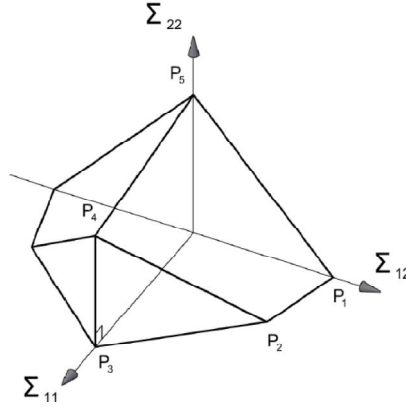


Figure 5.4 Limit elastic domain of masonry in the macroscopic state of stress.

For instance, the surface defined by the points P1-P2-P4-P5 corresponds to the yielding of bed joints $\partial\Omega^2 \cap \partial\Omega^3$ and $\partial\Omega^4 \cap \partial\Omega^1$, Figure 5.2. The surfaces delimiting the limit elastic domain may be derived by the following expressions which define the vertex of the surfaces depicted in Figure 5.4:

$$\begin{aligned}
 P_1 &= \left[0; c \frac{2m + \xi}{2m + \xi \cdot (1 + \mu m)}; 0 \right] \\
 P_2 &= \left[\frac{c \xi}{2m} \frac{(1 + \mu m)(1 + 2m\xi)}{\mu \xi \cdot [\xi + m \cdot (2 + \mu \xi)] - m}; \frac{c \cdot (2m + \xi)(2\mu \xi - 1)}{2\mu \xi [\xi + m \cdot (2 + \mu \xi)] - 2m}; 0 \right] \\
 P_3 &= \left[\frac{c}{\mu} \frac{1 + 2\xi m}{2\xi m}; 0; 0 \right] \\
 P_4 &= \left[\frac{c}{\mu} \frac{1 + 2m\xi}{2m\xi}; 0; \frac{c}{\mu} \frac{2\mu \xi - 1}{2\mu \xi} \right] \\
 P_5 &= \left[0; 0; \frac{c}{\mu} \right]
 \end{aligned} \tag{5.78}$$

where the following constants have been introduced $m = 2a / b$, $\xi = K_n / K_t$.

By referring to the same micro-mechanical model of units connected by interfaces obeying to a Mohr-Coulomb criterion, it is possible to obtain an analytical expression for the yield surface of masonry, *i.e.* which delimits the set

of the admissible macroscopic stress for the material. More precisely by following the approach presented in De Buhan and de Felice (1997), the macroscopic yield domain may be defined in terms of the strength parameters of the joints (c, μ) , on the aspect ratio of the units $m = 2a/b$ and is bounded by a set of planes $F^i(\Sigma)$ intersecting in a non smooth way, Figure 5.5. When $m < 1/\mu$, which is the most relevant case for masonry, the domain comprises $i = 4$ number of planes which can be written in terms of the macroscopic stress components as follows:

$$\begin{aligned}
 F^1 &= m \Sigma_{11} + \mu \Sigma_{22} + (1 + m \mu) \Sigma_{12} - \frac{c}{\mu}(1 - m) \\
 F^2 &= m \Sigma_{11} + \mu \Sigma_{22} - (1 + m \mu) \Sigma_{12} - \frac{c}{\mu}(1 - m) \\
 F^3 &= \Sigma_{22} + \frac{1}{\mu} \Sigma_{12} - \frac{c}{\mu} \\
 F^4 &= \Sigma_{22} - \frac{1}{\mu} \Sigma_{12} - \frac{c}{\mu}
 \end{aligned} \tag{5.79}$$

Conversely, for the case $m \geq 1/\mu$, the yield surface comprises six planes as describe in the cited paper.

Both the elastic limit and the yield domain reproduce the anisotropic behavior of the material deriving from the arrangement of the blocks within the masonry assemblage and result unbounded in the compressive regimes since failure of the unit is not accounted for in the model. The two domains are compared in Figure 5.5 where it is shown that the elastic-limit domain obtained in two limit cases, where we assume $\xi = 0$ and $\xi = \infty$, falls inside the yield domain proposed by De Buhan and de Felice (1997). Since Eqs. (5.78) are monotonic with respect to ξ , the latter finding confirms that the analytical expressions found for the two domains are consistent since the limit elastic surface falls always inside the co-respective domain obtained adopting the yield design homogenization, as it was expected. Moreover, only in some cases the two domains have points in common where the hardening effect does not take place.

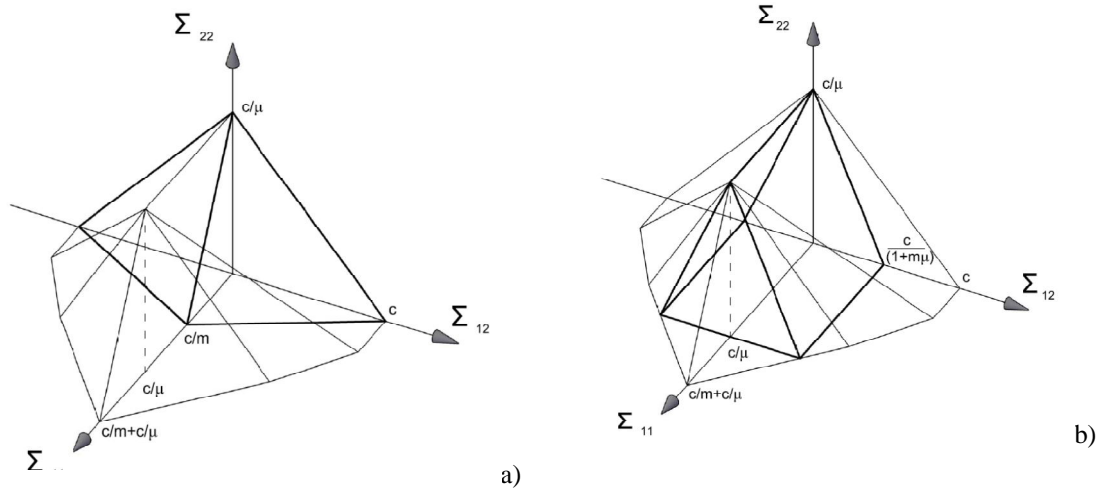


Figure 5.5 Comparison between the yield surface (thin line) by De Buahn and de Felice (1996) and the elastic limit surface (thick line) evaluated for $\xi = 0$ (a) and $\xi = +\infty$ (b).

The surfaces presented delimit in the space of macroscopic stresses the three phases of masonry behaviour. In order to describe the complete response of the material undergoing a prescribed loading history it is possible to follow different strategies. One possible approach consists in assuming that the material behaves elastically in accordance with Eq. (5.70)-(5.73) up to the complete yielding. This approach proves attractive since, by assuming at the macroscopic level an elasto-perfect plastic behaviour with associated flow rule, the classical integration schemes for multi-surface plasticity may be adopted for predicting the response of the homogenized material, see de Felice *et al.* (2010). On the other hand this method neglects the strain hardening deriving from residual stresses and may be applied rigorously only when the joints show an high dilatancy, which represents the exception rather than the norm. In order to overcome these limitations it is possible to follow a different approach by adopting the multi-scale algorithm presented, which allows us to trace the equilibrium path of the material from the initialization of plastic microscopic strains up to complete yielding and to account for the presence of joints with different levels of dilatancy. Some applications of the latter approach are discussed in the subsequent part where numerical tests are performed on the RVE undergoing different macroscopic loading conditions.

Response of the RVE under macroscopic loading conditions

Let us consider a brickwork made with units having height $a = 0.055$ m and length $b = 0.125$ m, which corresponds to an aspect ratio $m = 0.88$. The Lamé's constants of the unit are assumed equal to $\lambda^b = 3.18$ GPa and $\mu^b = 1.29$ GPa. The whole set of joints has normal and tangential stiffness equal to $K_n = 30.6$ GPa/m and $K_t = 12.8$ GPa/m, while the cohesion and the coefficient of friction are assumed equal to $c = 10.0$ KPa and $\mu = 0.6$, respectively. In order to outline the effects of the dilatancy, two values for ψ are adopted, namely 0.0 and 0.6.

Let us refer to a generic material point initially unloaded, which undergoes an increasing applied load expressed as $\lambda \hat{\Sigma}$, where $\hat{\Sigma}$ represents a direction within the space of macroscopic stresses and λ is a scalar representing the load multiplier. The aim is evaluating the response of the material point in terms of $\Sigma - E$ relation along the load direction $\lambda \hat{\Sigma}$. To this purpose the multi scale algorithm has been implemented in Matlab and the problem solved numerically by adopting an arch-length incremental-iterative procedure, Riks (1979).

The first test performed at the microscopic level refers to the case of a material point undergoing an increasing traction applied in the horizontal direction. The macroscopic stress-strain curves obtained by varying the dilatancy are plotted in Figure 5.6 together with the transversal deformation recorded during the loading history.

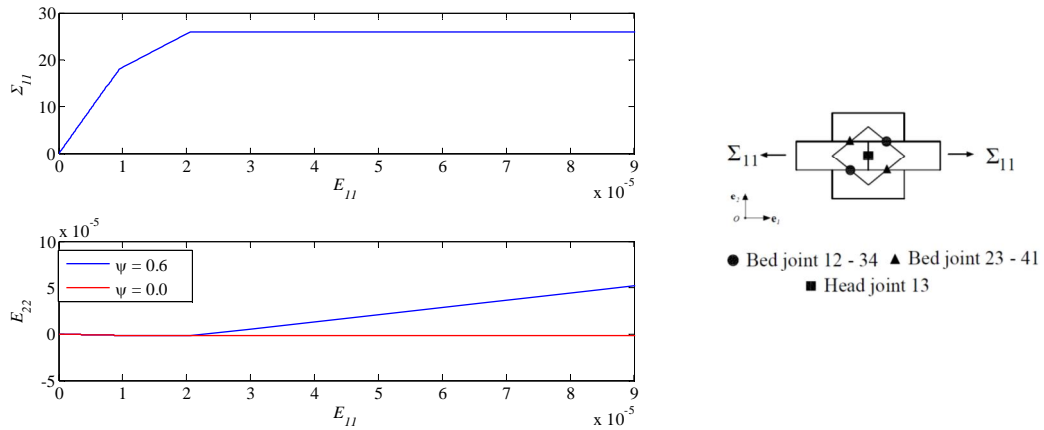


Figure 5.6 Masonry under pure horizontal traction: comparison between the stress-strain relations and the ratios between horizontal and vertical strains obtained for $\psi=0.6$ and $\psi=0.0$.

As it was expected, the dilatancy does not affect locally the strength of the material, which is trivial since the problem is stress-driven and no constraint are imposed on the vertical deformation upon the application of the load. The results would be remarkably different if strain-driven approach is followed. The deformed shapes of the RVE, obtained for the two values of dilatancy considered in the present work, are plotted in Figure 5.7.

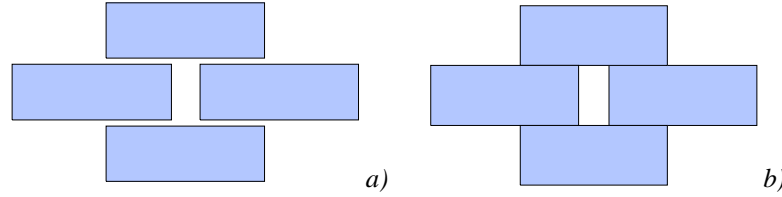


Figure 5.7 Masonry under pure horizontal traction: comparison between the deformed shapes of the RVE obtained for $\psi=0.6$ (a) and $\psi=0.0$ (b).

Three phases of the material response are clearly identified. In the first and second phases there is a transversal deformation related to the Poisson-type contraction of the unit, which behaves elastically, Figure 5.6. In the third phase the vertical deformation keeps constant in absence of dilatancy while remarkably increase in the case where dilatancy is accounted for in the model, as it was expected. Noteworthy, the curves obtained are piece-wise constant since the behaviour of the material is governed by a discrete number of parameters, which derives from the restrictions imposed on the kinematics of the RVE. In order to better outline the interaction between the components under increasing horizontal traction, the forces acting within the unit, bed and head interfaces are plotted together in Figure 5.8.

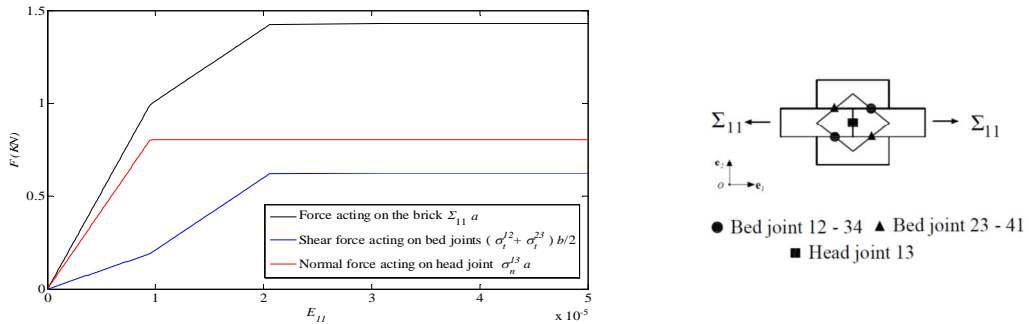


Figure 5.8 Masonry under pure horizontal traction: Comparison between the force acting within the unit and mortar joints, the curves are independent on the dilatancy assumed.

According to Figure 5.8, the elastic phase ends in correspondence to the opening of the vertical joint. Under increasing loads the horizontal joints tend to bear more shear stress since the overall material can not rely anymore on the contribution of the head interface. Finally, the homogenous material reaches the complete yielding when the bed joints reach their respective limit domain.

The second numerical test conducted at the microscopic level, considers a material point undergoing a pure macroscopic shear stress. The responses obtained in case of associated and non-associated plasticity are reported in Figure 5.9. Analogously to the previous test, the strength of the material is unaffected by the level of the dilatancy angle assumed which affects only the deformed shapes, Figure 5.10.

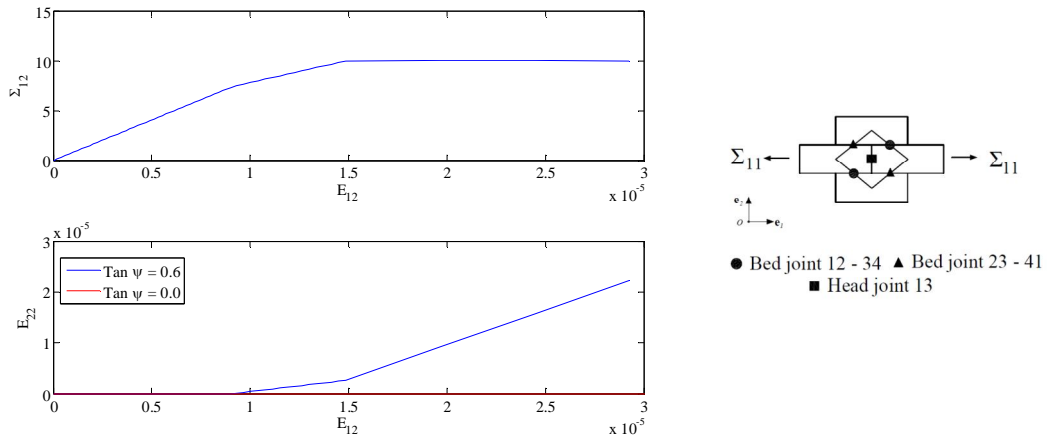


Figure 5.9 Masonry under pure shear: comparison between the stress-strain relations and the ratios between horizontal and vertical strains obtained for $\psi=0.6$ and $\psi=0.0$.

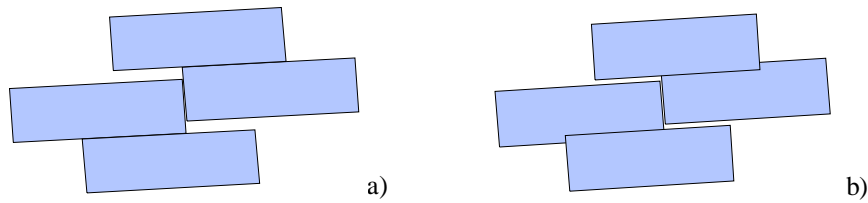


Figure 5.10 Masonry under pure shear: comparison between the deformed shapes of the RVE obtained for $\psi=0.6$ (a) and $\psi=0.0$ (b).

The third numerical test conducted at the microscopic level, refers to a material point undergoing macroscopic shear stress combined with horizontal traction. A proportional load is applied by keeping constant the ratio $\Sigma_{11} / \Sigma_{12} = 1$. The results are plotted in Figure 5.11- Figure 5.12.

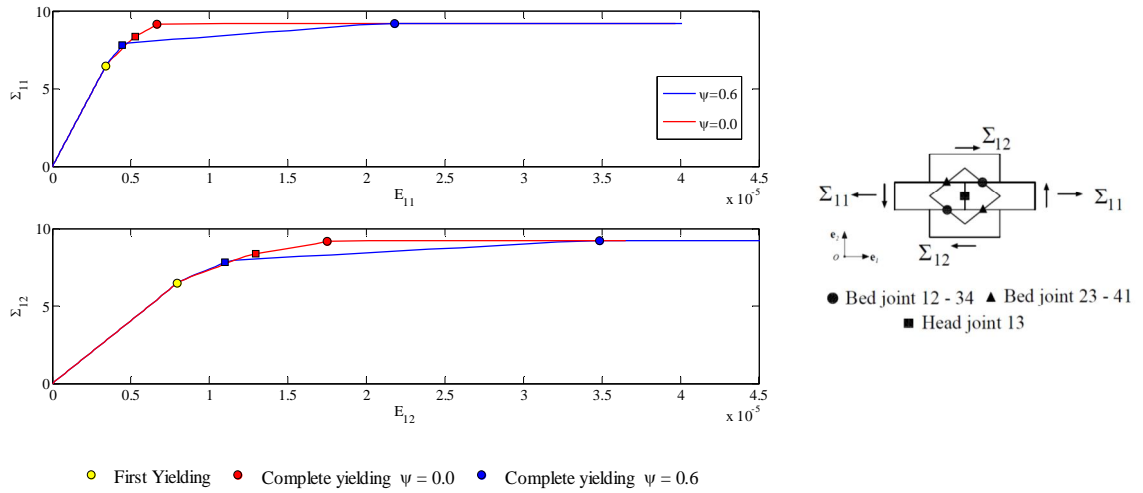


Figure 5.11 Masonry under horizontal traction combined with shear: comparison between the stress strain curves obtained for $\psi=0.6$ and $\psi=0.0$. The markers delimit the phases of masonry behaviour.

With respect to the previous cases presented, masonry stress –strain curve depends on the level of dilatancy adopted for the joints. To better investigate this aspect, the microscopic stress-strain curves recorded in the joints under increasing macroscopic load are reported in Figure 5.13. On the whole it is possible to distinguish three different phases:

Phase 1: The linear elastic phase, ending when the joint (23-41), which undergoes combined tensile stress and shear, reaches the yield domain (●).

Phase 2: At this stage, the capability of the RVE to sustain increasing loads rely upon the head joint. The slip developed by the joint (23-41), which is driven by the macroscopic shear stress, induces a tensile stress on the former interface which cumulates with the tensile stress induced by the horizontal traction applied to the RVE. Moreover, when dilatancy is accounted for in the model, the normal displacement developed by joint (23-41) induces an additional shear stress on the head interface, Figure 5.12. Under the abovementioned state of stress the head joint reaches suddenly the limit conditions and start to develop plastic strain (■-■).

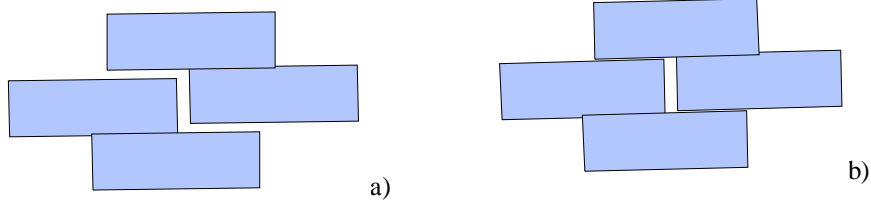


Figure 5.12 Masonry under horizontal traction combined with shear: comparison between the deformed shapes of the RVE obtained for $\psi=0.6$ (a) and $\psi=0.0$ (b).

Phase 3: In this phase, the head interface tends to open completely and to bear lower and lower level of shear. This is clarified in Figure 5.14 where the stress paths experienced by the interfaces are plotted against the Mohr-Coulomb criterion. Accordingly, the head joint in this stage tends towards the apex of the yield criterion. When this condition is achieved the latter joint is not able to bear anymore shear and the system reaches the complete yield condition (●-●). The main differences between the cases analyzed arise here: the development of normal displacements on bed and head interfaces due to the dilatancy results in an overall lower stiffness of the homogeneous material in this phase when compared to the stiffness exhibited in the case where dilatancy is set equal to zero, Figure 5.11. The final strength of the material remains anyway unaffected.

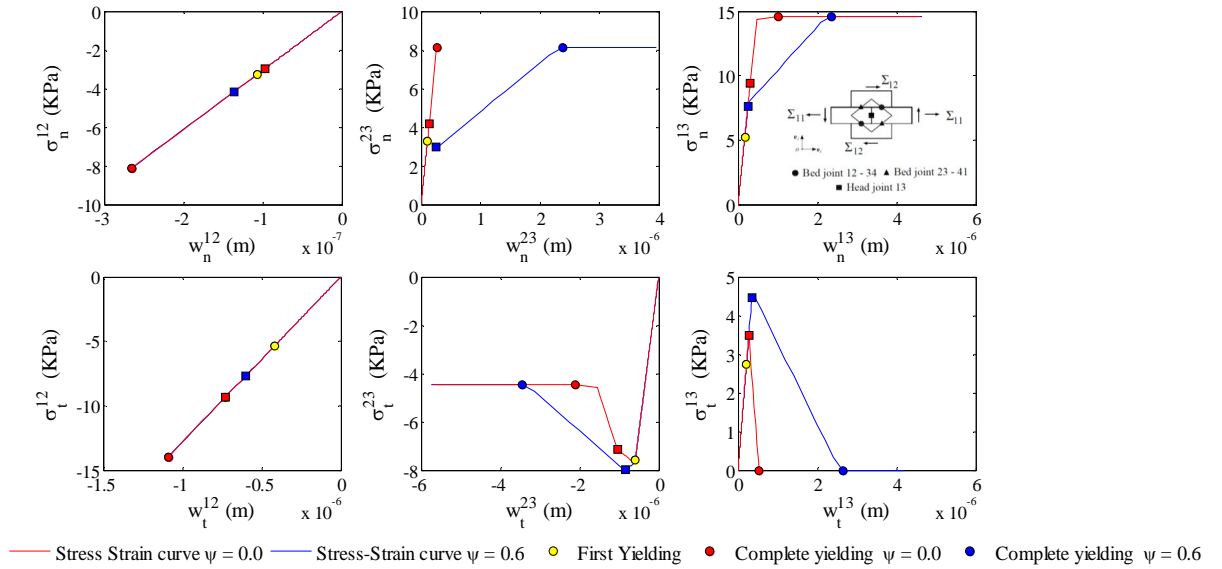


Figure 5.13 Masonry under shear combined with horizontal traction: Comparison between the stress-strain history recorded on the joints for $\psi=0.6$ and $\psi=0.0$.

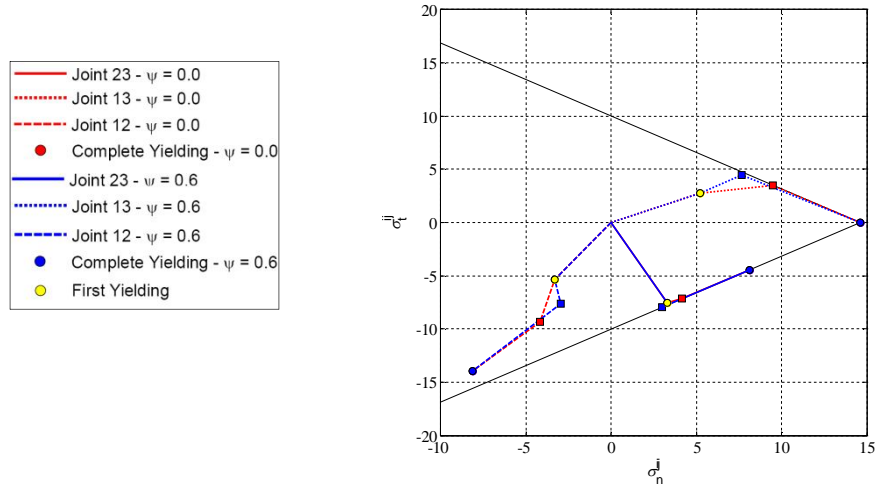


Figure 5.14 Masonry under shear combined with horizontal traction: Comparison between the equilibrium paths followed by the components and plotted in the space of microscopic stress together with the Mohr Coulomb yield surface.

Numerical simulations and applications

The multi-scale algorithm formulated in the previous paragraphs has been implemented as an UMAT subroutine in the general purpose finite element program Abaqus, Simulia (2011). To test the feasibility of the proposed approach, finite element analyses of in-plane loaded walls are presented and the results compared against experimental tests on dry-stack masonry and analytical approaches based on the yield design theory. Eventually the methodology is applied to evaluate the response of masonry arches under non-uniform ground settlement.

Wall under vertical compression and horizontal traction

Let us consider a masonry wall bearing its self weight, a vertical pressure q applied at the top and undergoing a prescribed horizontal displacement u imposed at the later sides, Figure 5.15. The aim is to derive the maximum allowable horizontal traction which the wall can sustain under increasing horizontal displacement.

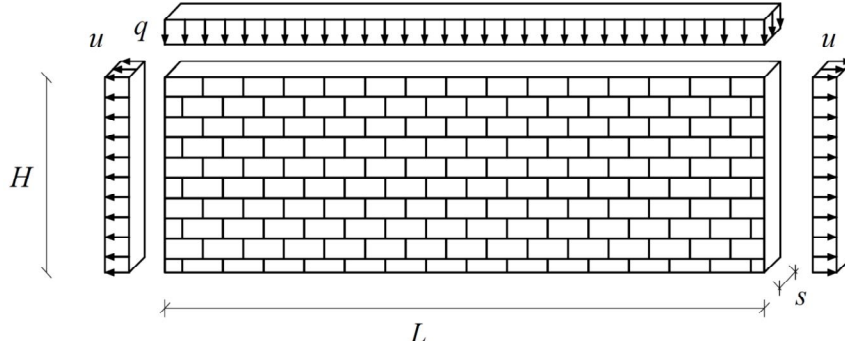


Figure 5.15 Masonry wall subjected to gravity load, vertical pressure q and horizontal displacement u imposed at the later sides.

The problem admits an analytical lower bound solution which expresses the horizontal tensile force corresponding to the complete yielding of the wall. In accordance with the approach followed in de Felice *et al.* 2010, let us assume that each block of the wall experiences the stress state shown in Figure 5.16.

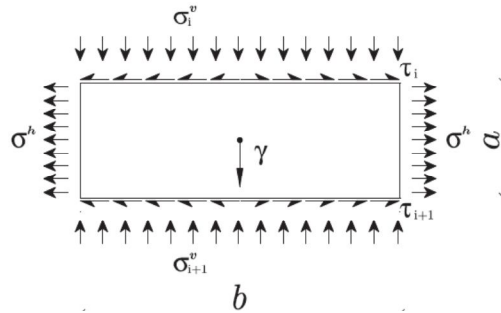


Figure 5.16 Stress state experienced by the unit located in correspondence of the course i of the wall.

The gravity and the vertical load applied induce on the bed joint a vertical compression which varies linearly along the height of the wall. More precisely, according to equilibrium conditions, denoting by i the number of block tiers above the bed joint under consideration, the vertical stress σ_i^v is uniform and reads:

$$\sigma_i^v = q + i\gamma a \quad (5.80)$$

Conversely, the horizontal traction applied at the edge of the wall induces shear stresses on the bed joints τ_i and vertical traction on the head joints σ_i^h .

When the complete yielding of the wall is achieved all the components are supposed to provide their maximum contribution. Therefore, it is reasonable to assume that the stress σ_i^h is uniform along the head joint and that the shear stress τ_i is piece-wise constant with opposite sign in two half sides of each unit. By cumulating the contribution of the whole set of n tiers, the resultant of the traction T , applied at the lateral edge of the wall and which is in equilibrium with the stress state acting on the units, reads:

$$T = H\sigma^h + \frac{b}{2} \sum_{i=1}^n \tau_i \quad (5.81)$$

In order to derive the maximum allowable horizontal traction T_{lim} per unit depth of the wall, let us impose that the stress state acting on the whole set of joint fulfils the Mohr-Coulomb condition:

$$T_{lim} = H \frac{c}{\mu} + \frac{b}{2} \sum_{i=1}^n [c + (q + i\gamma a) \mu] \quad (5.82)$$

where the first two terms account for the cohesive contribution of head and bed joints, respectively, and the second terms account for the frictional contribution of bed joints provided by the self weight and the applied load q . In order to perform a comparison with the results obtained by applying the proposed homogeneous model, let us evaluate the maximum traction acting on the wall in the limit case where the dimensions of the unit tend to be small compared to the dimensions of the wall. By expressing the height and the width of the block as

$$a = \frac{H}{n}, \quad b = \frac{2H}{m n} \quad (5.83)$$

and by substituting into the Eq. (5.82), one would obtain:

$$T_{lim} = H \left[\frac{c}{\mu} + \frac{c}{m} + \frac{\mu}{m} \left(\frac{\gamma H}{n^2} \sum_{i=1}^n i + q \right) \right] \quad (5.84)$$

In the limit condition where $n \rightarrow \infty$ the latter expression reads:

$$\lim_{n \rightarrow \infty} T_{lim} = H \left[\frac{c}{\mu} + \frac{c}{m} + \frac{\gamma H}{2} \frac{\mu}{m} + q \frac{\mu}{m} \right] \quad (5.85)$$

In the above expression, the cohesive contribution of head joint cumulates with the cohesive and frictional contributions of bed joints properly scaled by the internal angle of the brickwork m . The numerical simulation is carried out on

one-half of the specimen by exploiting the symmetry of the problem. Accordingly, the wall is simply supported at the base; one of the lateral edges is free to move in both directions while the opposite one is constrained in the horizontal direction. The finite element mesh adopted consists in 900 four nodes compatible finite elements, as reported in Figure 5.18. The analysis is then carried out in two subsequent step. First the gravity load is applied together with the pressure q located at the top of the wall. Then, an uniform increasing horizontal displacement is imposed on the free lateral side until complete yielding of the system is achieved. The geometrical and mechanical properties adopted for defining the finite element model are reported in the Table 5.1. The response of the wall may be expressed in terms of the resultant of the reactions applied at the constrained edge versus the imposed horizontal displacement. The force-displacement curve per unit depth of the wall is plotted in Figure 5.18 together with the analytical result provided by Eq. (5.85) , $F=25.42$ KN/m.

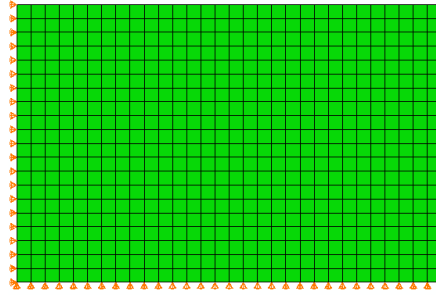


Figure 5.17 Masonry wall under vertical load and horizontal traction: finite element mesh.

Heigh of the wall	H	0.98	m	Normal Stiffness of the interface	K_n	3.06E+07	KPa/m
Length of the wall	L	3.0	m	Tangential Stiffness of the interface	K_t	1.28E+07	KPa/m
Thickness of the wall	s	0.12	m	Cohesion of the joints	c	5	KPa
Heigh of the unit	a	0.04	m	Coefficient of friction	μ	0.6	-
Length of the unit	b	0.09	m	Coefficient of dilatancy	ψ	0.0	-
Density	γ	15	KN/m ³	Yound modulus of the unit	Y_b	3.18E+06	KPa
Applied pressure	q	10	KPa	Poisson coefficient of the unit	ν_b	0.23	-

Table 5.1 Geometrical and mechanical properties of the phases adopted in the numerical simulation.

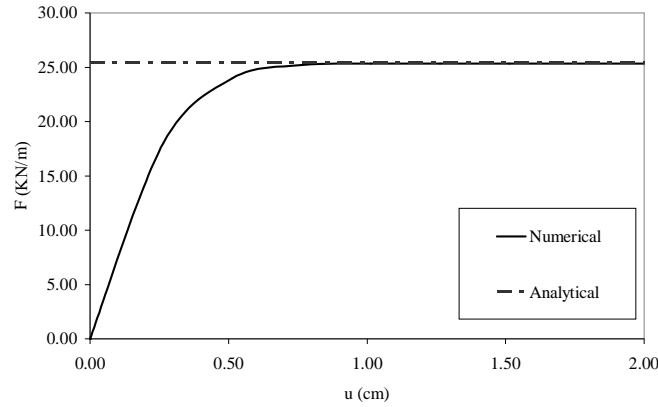


Figure 5.18 Comparison between the force-displacement curve obtained by the proposed approach and the analytical solution obtained by applying the yield design method.

The main feature of the multi-scale approach consists in the chance to derive for each Gauss point of the wall directly information on the opening of the joints induced by the external load. In the case at hand, owing to the symmetry of the problem, the plastic slip developed within the two couple of bed joints coincide and, owing to the compatible kinematics adopted in the present work for the RVE, their sum proves equal to the opening of the head interfaces, see for instance Figure 5.7. Accordingly, it is sufficient to report the plastic jump of displacement developed by the head interfaces.

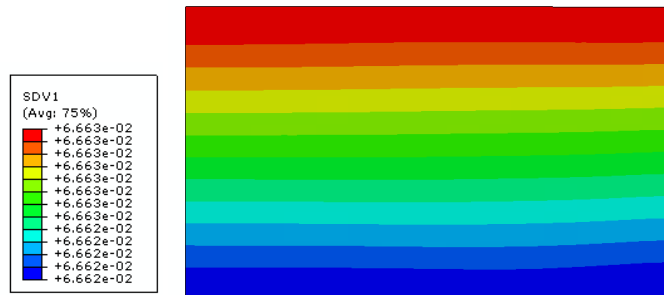


Figure 5.19 Normal plastic jump of displacement of the head interface w_n^{13} (in cm) for a displacement imposed at the lateral edge of the wall equal to 2 cm.

A slight variation of the plastic strain developed by the joints is found over the height of the wall. In fact, when complete yielding is reached the joints located at the top exhibits an higher plastic slip with respect to the joints located at the base of the wall because of the contribution provided by the frictional

terms in Eq. (5.85). Therefore these differences derive from the elastic jump of displacements which are maximum at the bottom and decrease while approaching the top of the wall.

Wall under gravity load and uniform horizontal acceleration

In the present part the proposed methodology is adopted to reproduce the tests by Ceradini (1992), who conducted an experimental campaign for studying the behaviour of dry stack masonry walls under uniform in-plane vertical and horizontal accelerations. The tests aimed at defining the modes of failure and the collapse load multiplier λ_{lim} , *i.e.* the ratio between vertical and horizontal accelerations that triggers the collapse, of a variety of walls which differs in terms of masonry texture and geometrical aspect ratio ($\rho=H/L$). More precisely, the units adopted, which have dimensions $0.04 \times 0.0175 \times 0.08 \text{ m}^3$, have been arranged in two different ways so as to obtain masonry textures characterized by an internal angle m equal to 0.427 and 0.875, respectively, Figure 5.20.



Figure 5.20 Masonry textures investigated by Ceradini (1992).

For each texture considered, walls having ratio $\rho=H/L$ ranging from 0.12 to 2 have been tested, Figure 5.21a. Additionally, the effects of openings and of the presence of tie bars have been investigated as well by the cited authors.

In order to induce the in-plane collapse of the wall, the load has been applied by progressively inclining the laying plane of the specimen, Figure 5.24b, which reduces the component of the gravity in the direction perpendicular to the bed joints while increasing the component in the direction parallel to the bed joints. Finally, the collapse load multiplier was recovered by measuring the inclination of the laying plane at which the wall collapsed.

The problem admits an analytical solution which provides an upper bound estimate for the horizontal load multiplier corresponding to the collapse of the wall, De Buhan and de Felice (1997). More precisely, the yield design theory is applied by assuming a kinematically admissible collapse mechanisms, identified by the discontinuity line OO' depicted in Figure 5.22.

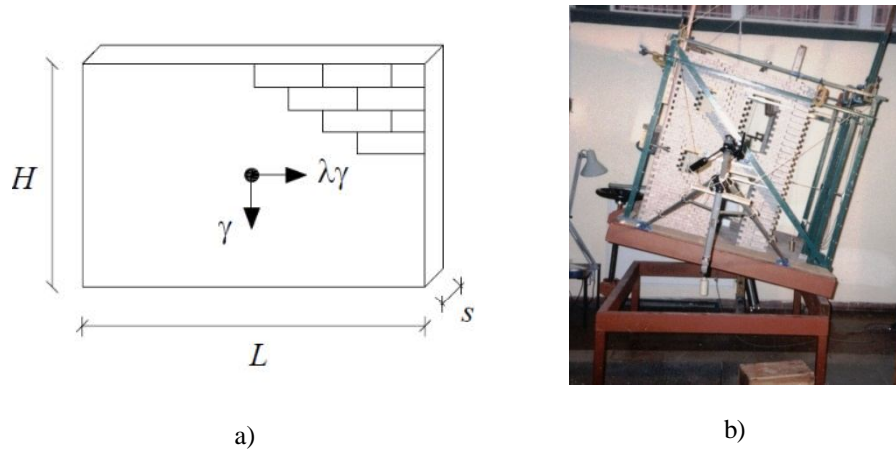


Figure 5.21 Masonry walls under uniform vertical and horizontal accelerations:(a) view of the walls,(b) system of application of the load adopted by Ceradini (1992).

The work of the external forces is computed by assuming a rigid body motion for the portion of the wall above the discontinuity line OO' . Conversely, the maximum resisting work is evaluated by integrating the work spent along the crack OO' by assuming the homogenized failure surface of masonry derived in the same paper by the cited author, Figure 5.5.

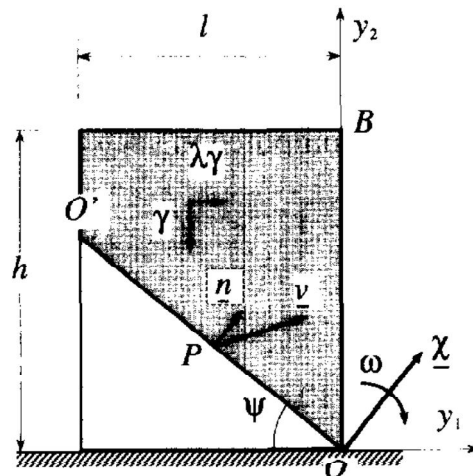


Figure 5.22 Rigid block failure mechanism assumed by De Buhan and de Felice (1997) for the homogenized wall undergoing uniform vertical and horizontal accelerations.

By minimizing the ratio between the maximum resisting work and the external work, an upper bound estimate for the collapse load multiplier is obtained and reads:

$$\lambda_{\lim} = \begin{cases} 1/2(m/\mu)^{1/2} & \text{if } \rho = H/L \leq (m/\mu)^{1/2} \\ \frac{3\rho - 2(m/\mu)^{1/2}}{3\rho^2 - 2(m/\mu)} & \text{otherwise} \end{cases} \quad (5.86)$$

in case a rigid rotation around the centre O is assumed, and reads:

$$\lambda_{\lim} = \mu \quad (5.87)$$

in case a rigid horizontal translation of the wall is assumed.

Finite element analyses are conducted in order to reproduce the behaviour of three types of walls which have the same area, equal to 16 m², and different aspect ratios $\rho = H/L$, equal to 0.5, 1.0 and 2.0. Only one of the two texture investigated by Ceradini (1992) is adopted here. More precisely an aspect ratio for the unit $m = 0.875$ is assumed. The Lamé's constants of the unit are assumed equal to $\lambda^b = 1.1$ GPa and $\mu^b = 1.29$ GPa. The whole set of joints has a normal and tangential stiffness equal to $K_n = 30.6$ GPa/m and $K_t = 12.8$ GPa/m, while the cohesion and the coefficient of friction are assumed equal to $c = 0.0$ KPa and $\mu = 0.6$, respectively. Finally, a small value of dilatancy, $\psi = 0.2$, is assigned to the interfaces between the units.

The three walls are constrained at the base both in the horizontal and vertical directions. The meshes adopted consist in 800 four nodes compatible finite elements. The problem is tackled in plane stress condition and the loads are imposed in two subsequent steps: first the gravity is applied, then an increasing horizontal acceleration is imposed uniformly over the model until the collapse mechanisms is achieved.

The response of the wall having H/L ratio equal to 0.5 is plotted in Figure 5.23 in terms of the horizontal load multiplier λ and the horizontal displacement u measured at a control point located at the top-right corner of the model. The results are compared against the average of the load multiplier evaluated experimentally and the one predicted by the analytical model proposed in De Buhan and de Felice (1997).

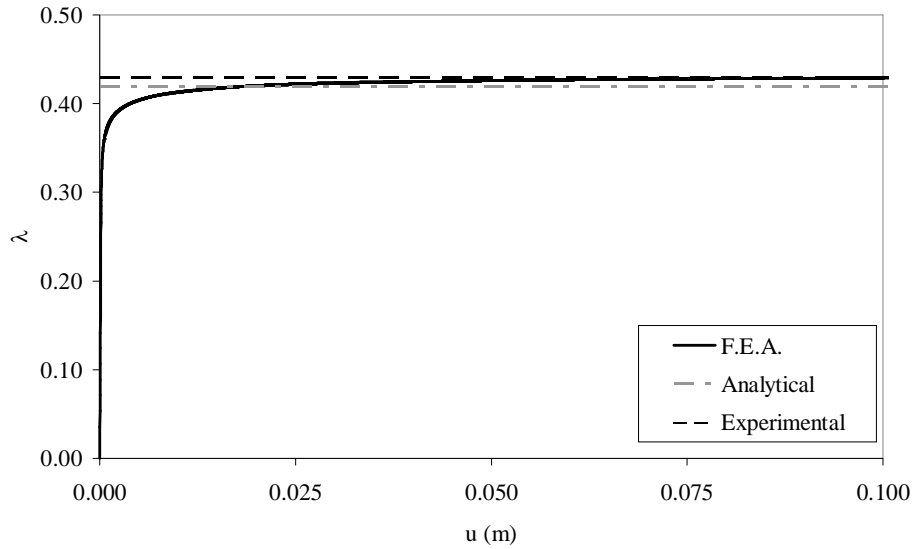


Figure 5.23 Horizontal load multiplier versus the displacement measured at the top of the wall ($H/L=0.5$).

According to experimental evidences, the collapse is triggered by the development of a stair-step crack which propagates from the top edge towards the bottom-right corner of the wall. Noteworthy, only a small portion of the entire specimen is involved by the mechanism while the remaining part of the stonework is unaffected by the external load. A comparison between experimental and numerical outcomes is reported in terms of deformed shape of the wall together with the plastic displacement experienced by the joints, Figure 5.24.

In the finite element analysis conducted by means of the multi-scale approach, the crack observed during the test is reproduced by a band where the plastic strains develop. In this band, the plastic displacement exhibited by the bed joint 12 proves negligible with respect to the displacements which occur in the other joints. In fact, while the former experiences shear and compression stresses upon the imposition of the load, the latter undergo shear combined with traction. Accordingly, since the proposed approach relies on a compatible scheme at the microscopic scale, the slip experienced by the bed joint 23 results equal to the normal strain experienced by the head joint, and therefore is sufficient to describe the plastic deformation exhibited by the material, see for instance Figure 5.12.

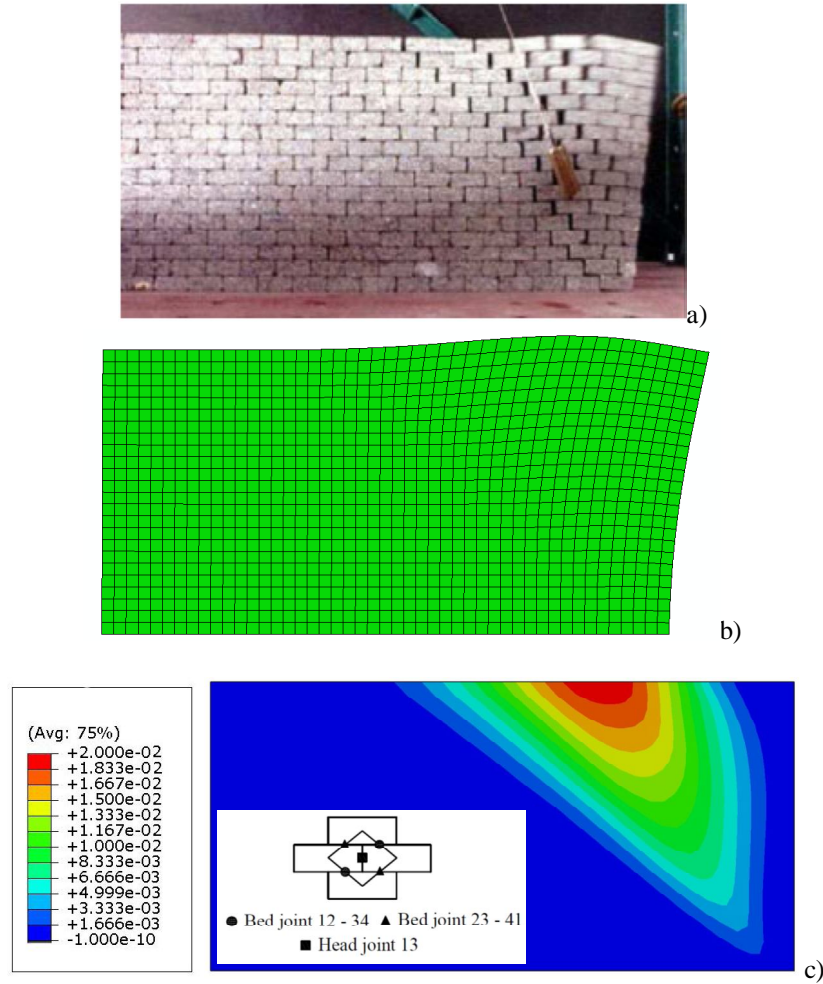


Figure 5.24 Wall having $H/L=0.5$: Comparison between experimental test (a) and numerical outputs in terms of the deformed shape at collapse (b) and plastic slips of bed interfaces w_t^{23} (c), expressed in m .

The result of the analysis conducted on the wall having H/L ratio equal to 1.0 are reported in Figure 5.25. The collapse load multiplier obtained by the experimental tests slightly decrease with respect to the previous case. Conversely the prediction made by the analytical formulation and the numerical analysis proves almost unchanged. A quite satisfactory reproduction of the deformed shape and the failure mode of the wall under increasing level of horizontal acceleration is found, Figure 5.27.

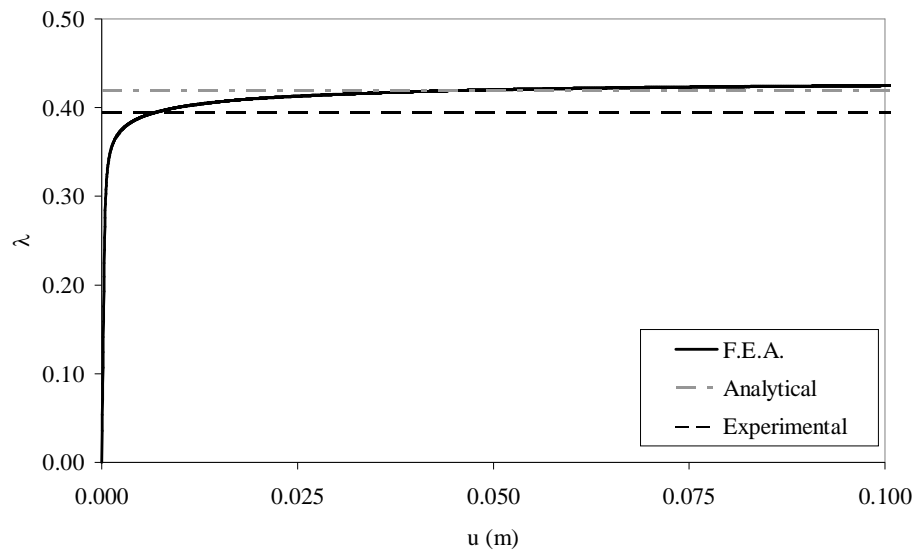


Figure 5.25 Horizontal load multiplier versus the displacement measure at the top of the wall ($H/L=1.0$).

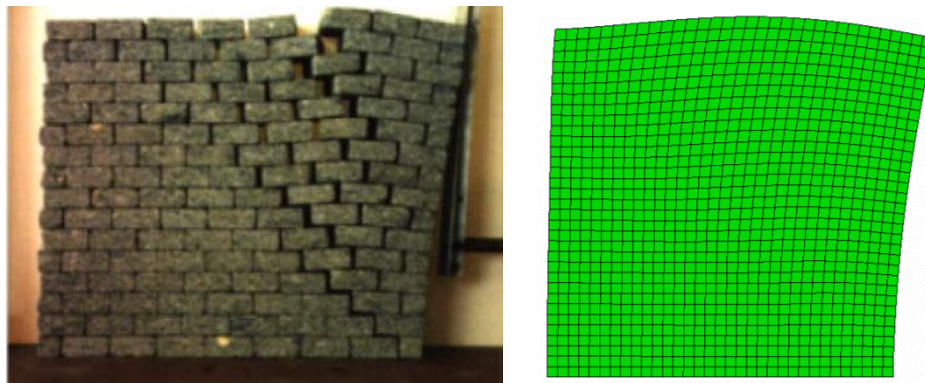


Figure 5.26 Collapse mechanisms of the wall having $H/L=1$ and amplified deformed mesh obtained by applying the multi-scale approach proposed.

The plastic strains develop in a band which is analogous to the one encountered for the wall with $H/L=0.5$, Figure 5.27, which may explain the negligible variation of the collapse load multiplier provided by the two numerical tests.

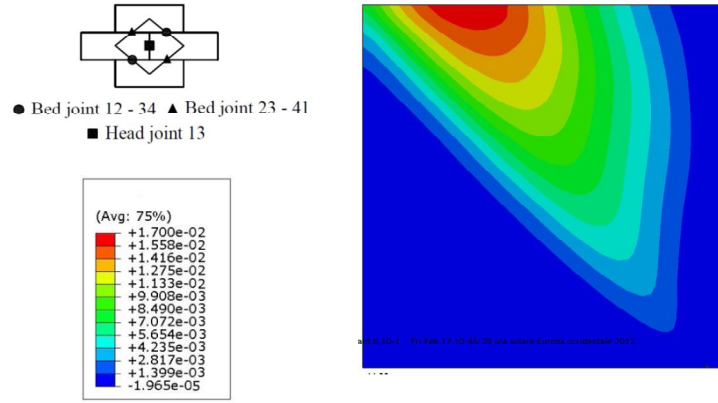


Figure 5.27 Contour plot of (a) the plastic slip w_t^{23} developed within the bed interface, expressed in m ($H/L=1$).

Finally, the last wall considered has an aspect ratio $H/L=2$. In this case an higher discrepancy is encountered between the proposed model and the experimental results, Figure 5.28. The contour plot of the plastic displacement exhibited by the bed joints at collapse is reported together with the deformed shape of the wall in Figure 5.29.

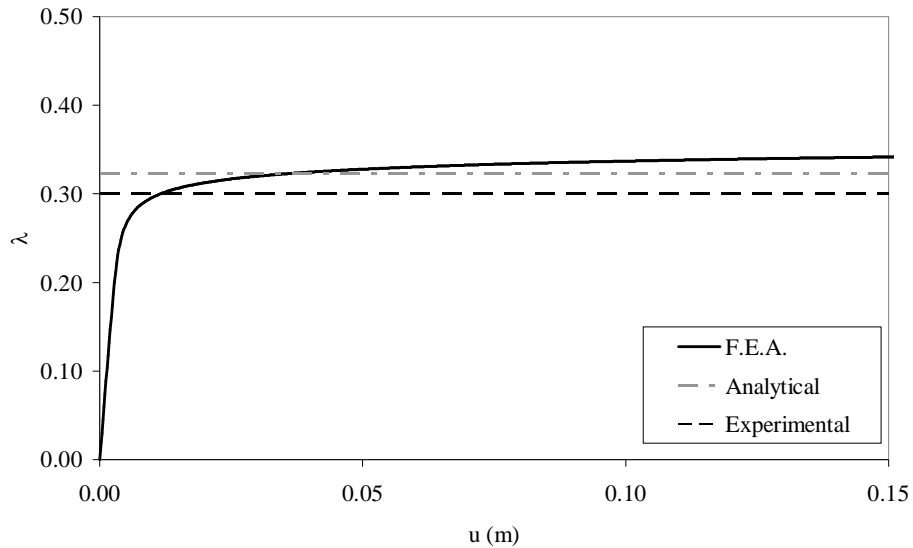


Figure 5.28 Horizontal load multiplier versus the displacement measure at the top of the wall ($H/L=2.0$).

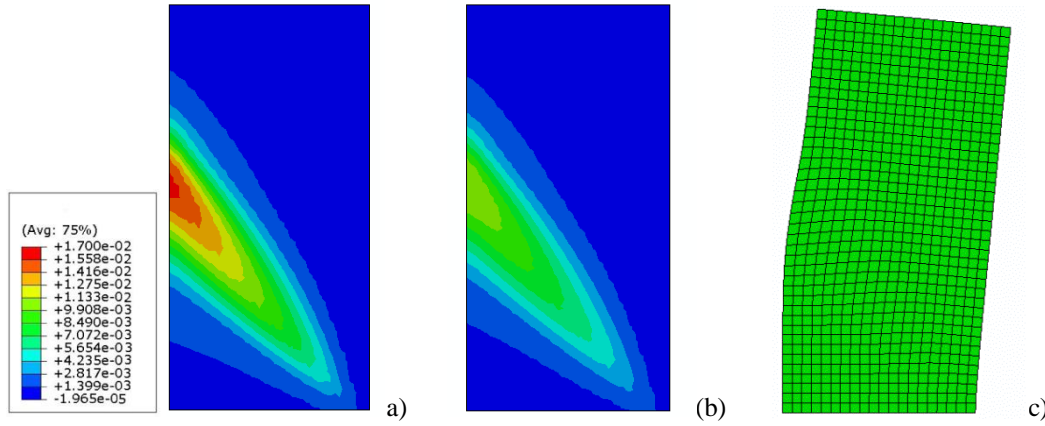


Figure 5.29 Contour plot of (a) the plastic slip w_t^{23} and (b) normal displacement w_n^{23} of bed interfaces, expressed in m , and amplified deformed shape at collapse (c), ($H/L=2$).

The overestimation of the collapse load multiplier reflects the mismatching between the observed collapse mechanism and the one predicted by the proposed model. According to Ceradini (1992), the wall tends to overturn by forming a crack analogous to that observed in the previous cases, which develops on the top of the specimen and isolates a small portion of the wall that overturns. On the contrary in the proposed model the plastic strains develop on the lateral edge of the wall and propagate towards the opposite corner at the base, Figure 5.29. Accordingly, the collapse predicted by the finite element analysis involves a bigger portion of the structure which may explain the higher collapse load multiplier obtained.

The results obtained can be summarized in the following plot where both the analytical and finite element solutions are compared against the whole set of experimental results obtained by Ceradini (1992). A good agreement is found between the analytical and finite element results, which is not surprising since they both originate from an homogenization approach applied to the same micro-mechanical model of block connected by interfaces. Moreover they both represent an upper bound estimate for the exact solution of the problem under consideration.

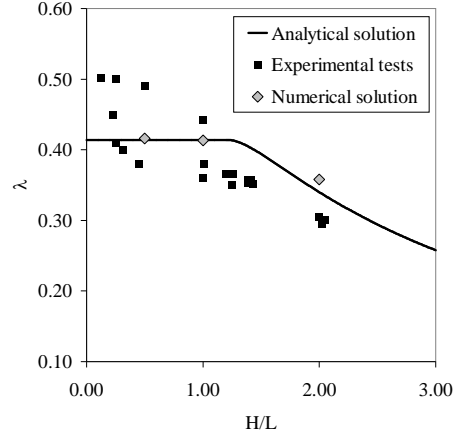


Figure 5.30 Comparison between the horizontal load multiplier evaluated by mean of the analytical solution by De Buhan and de Felice (1997) and by finite element analyses against the experimental tests by Ceradini (1992).

On the contrary some discrepancy may be found with the experimental tests in terms of the load multiplier. The latter discrepancy may be related to second order effects and to a “size” effect deriving from the finite number of bricks involved in the tests. The latter cannot be accounted for in the model since a first order homogenization approach is adopted here which relies on the hypothesis that the dimensions of the units are small when compared to the dimension of the structural element under consideration. In the latter condition, the following convergence result has been obtained (De Buhan 1986):

$$\lim_{n \rightarrow \infty} \lambda_{\lim} = \lambda_{\lim}^{\text{hom}} \quad (5.88)$$

Anyway, it is not possible to state if λ_{\lim} approaches from below or from above the value of $\lambda_{\lim}^{\text{hom}}$ since it may depend on the boundary condition applied to the problem. For instance, following the reasoning by de Felice *et al.* (2010), let us refer to the problem of the wall under vertical load and horizontal traction analyzed in the previous section of the chapter. Under the hypothesis that the wall at the base is able to provide either friction and cohesion, the maximum allowable horizontal traction decreases as the number of courses increases, Eq. (5.84).

Conversely, if the boundary conditions are change by removing the cohesion and friction at the base, the expression of the maximum horizontal traction reads:

$$T_{\lim} = H \left[\frac{c}{\mu} + \frac{c(n-1)}{m} + \frac{\mu}{m} \left(\frac{\gamma H}{n^2} \sum_{i=1}^{n-1} i + \frac{q(n-1)}{n} \right) \right] \quad (5.89)$$

which in the limit $n \rightarrow \infty$ convergences to the same value of the previous case, Eq. (5.85), with an opposite trend since the horizontal traction increases as the number of courses increases, indicating that the boundary conditions may affects the results for a finite number of courses n .

Response of masonry arches under non uniform ground settlements

Verification of existing structures to soil settlement is a topic of great interest in the technical community. Among others, masonry arches prove particularly sensitive to this kind of problems. In this context, the proposed multi-scale approach may be a valuable tool for the assessment of the damage induced by settlement on this type of structure. To this purpose let us analyse the case study of the Felice aqueduct. This structure was built between 1583 and 1585 from the Pope Sisto V and supplied water to two neighbourhoods in Rome, namely Viminale and Quirinale. In the area of Lodi square, the aqueduct was composed by a sequence of semi-circular tuff masonry arches having span of 2.3 m. Around 1930 because of the expansion of the city and of the needs for larger streets, five of the original arches of the aqueduct where demolished and replaced with solid brick masonry arches having span of 5.5m, Figure 5.31.



Figure 5.31 View of the Felice aqueduct in the area of Lodi square. Low span arches are the originals ones built with tuff masonry in XVI century while large span arches were built in 1930 with solid brick masonry, Sebastianelli (2011).

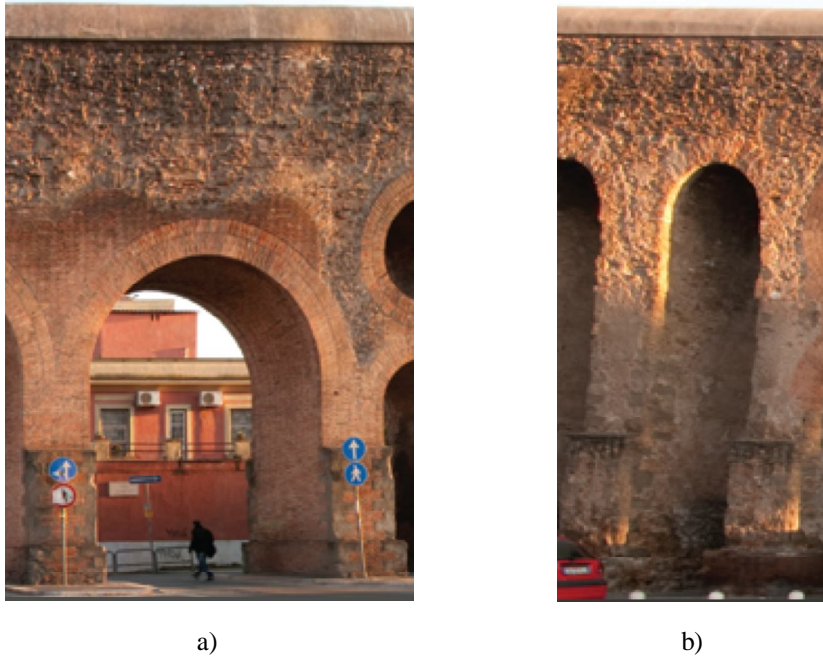


Figure 5.32 Details of brick (a) and tuff (b) masonry arches belonging to the Felice aqueduct, Sebastianelli (2011).

Recently, two galleries have been made at a depth of 20 m from the ground level for the construction of a new tube line. This intervention is thought to produce non uniform ground settlements which may induce cracking on the structure. Therefore, the aqueduct is currently under observation in order to monitor the development and, in case, the evolution of local damage.

In the following, numerical analyses are conducted in order to compare the behaviour of the two types of arcade belonging to the aqueduct. To this purpose let us consider the two portions of the latter structure as depicted in Figure 5.33. The first one reproduces a series of three tuff masonry semicircular arches having a span of 2.3 m; the piers are 8 m high and the height of the spandrel wall measured from the impost of the arches is 2.85 m. The second structure consists in a series of three solid brick masonry semicircular arches having span of 5.5 m; the piers are 5 m high and the height of the spandrel wall is 4.25 m. For the sake of simplicity, the thickness of the whole set of elements is assumed unitary in the out-of-plane direction. The aim is to analyse the response of these structures under a non uniform ground settlement. The finite element models adopted for

reproducing these portions of the structures are reported in Figure 5.33 and consist in a set of four node compatible elements. The models are constrained at the bottom of the piers both in the vertical and horizontal directions while only the horizontal direction is constrained at the lateral sides of the structure aiming at reproducing the interaction with the remaining part of the aqueduct. The ground settlement is reproduced as addressed next: once the gravity load has been applied, an increasing vertical displacement is imposed at the bottom of the central pier.

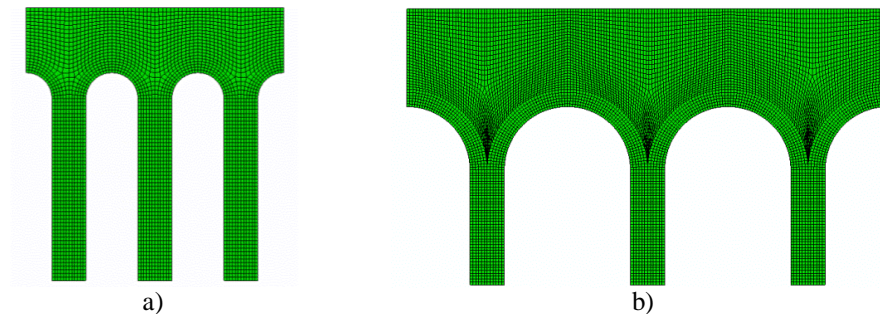


Figure 5.33 Finite element meshes adopted for modelling the arches of the Felice aqueduct: (a) small span arches, (b) large span arches.

The whole set of structural elements is modelled through the proposed multi-scale methodology. For properly modelling the behaviour of the arches, the local axes of the finite elements have been rotated in order to align the bed joints perpendicularly in each point to the direction of the arch. Conversely, the alignment of bed joints in the remaining part of the structure is kept parallel to the horizontal direction. The mechanical properties of the two types of masonry encountered have been adopted referring to the results of in-situ tests performed by G. Morelli from University La Sapienza, Roma, Sebastianelli (2011), which are reported in Table 5.2. As outlined by the plots, shear slips develop in a section of the arches located at the right side of the keystone. This is not surprising, since the settlement is thought to produce a reduction of the thrust in the arches which allows adjacent blocks to slide. Then, plastic bands initiate from the abovementioned sections of the arches and develop, under increasing displacement, towards the top edge of the spandrel wall. These plastic bands isolate one portion of the structure, so that the settlement does not affect considerably the wall and the arches beyond this region, Figure 5.34.

	Solid brick masonry			Tuff Masonry		
Height of the unit	a	0.05	m	a	0.04	m
Length of the unit	b	0.30	m	b	0.25	m
Young modulus of the unit	Y_b	2.00E+06	KPa	Y_b	1.50E+06	KPa
Poisson coefficient of the unit	ν_b	0.23	-	ν_b	0.23	-
Normal Stiffness of the interface	K_n	30.6	KPa/m	K_n	15	KPa/m
Tangential Stiffness of the interface	K_t	12.8	KPa/m	K_t	6.3	KPa/m
Cohesion of the joints	c	0.01	KPa	c	0.01	KPa
Coefficient of friction	μ	0.6	-	μ	0.6	-

Table 5.2 Geometrical and mechanical properties of the masonries belonging to the Felice aqueduct.

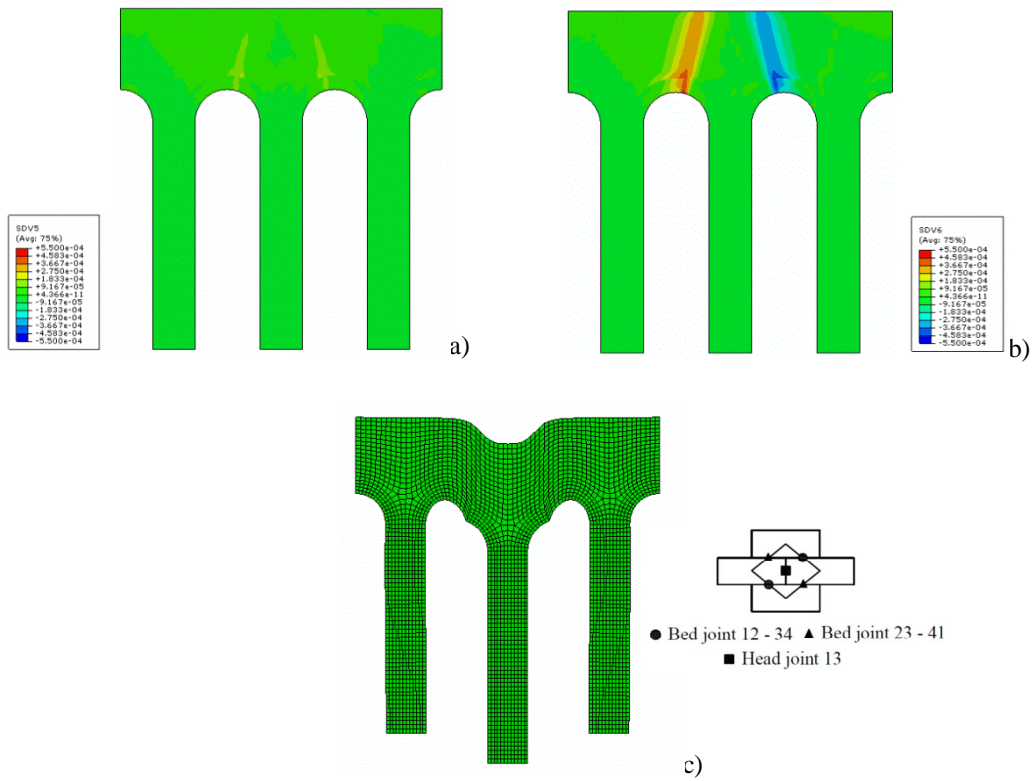


Figure 5.34 Contour plot of (a) the plastic normal displacement w_n^{23} , (b) the plastic slip w_t^{23} developed within the bed interfaces, expressed in m , and (c) the deformed mesh of low span arches. The plastic displacements experienced by bed joint 12 prove specular to the one here reported.

The analysis conducted on brick masonry arches having a larger span shows analogue results, which are reported in Figure 5.35 in terms of plastic displacements experienced by bed joint (23) and the deformed mesh recorded. In the case at hand, plastic bands develop from a section on the left side of the keystone and show an analogous inclination to the previous case discussed.

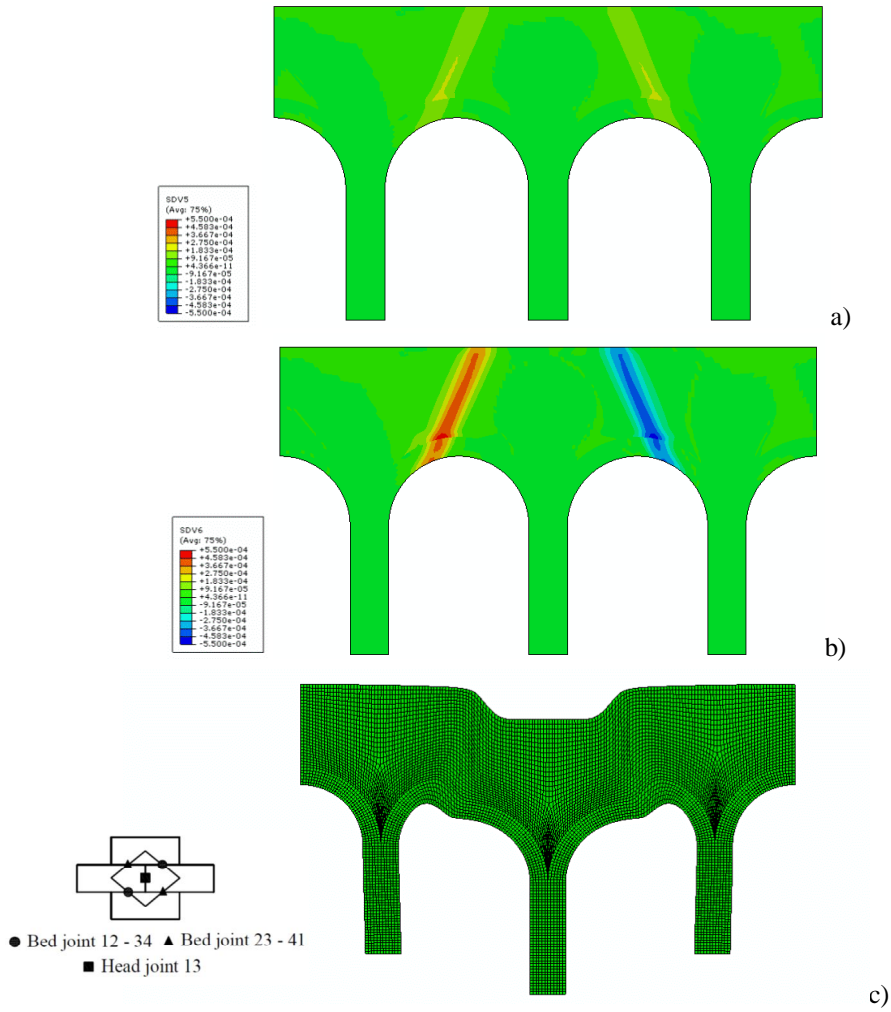


Figure 5.35 Contour plot of (a) the plastic normal displacement w_n^{23} and (b) the plastic slip w_t^{23} developed within the bed interfaces, expressed in m , together with (c) the deformed mesh for large span arches. The plastic displacements experienced by bed joint 12 prove specular to the one here reported.

In order to make a comparison between the responses of the two types of arches analysed, the total maximum jump of displacement $w_{\max} = \sqrt{w_n^2 + w_t^2}$ recorded on the interfaces within each structure is plotted against the ground deflection imposed, *i.e.* the ratio between the settlement imposed at the base of the central pier δ and two times the span of the arches $2L$.

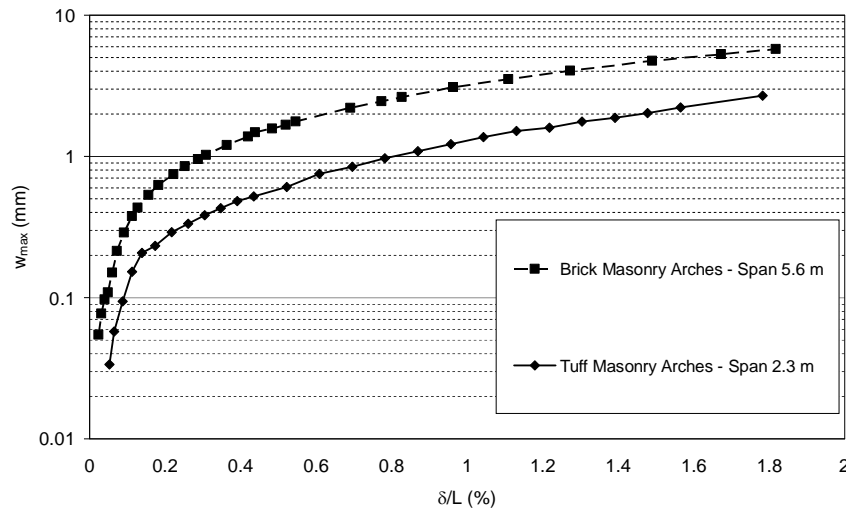


Figure 5.36 Comparison between the maximum jump of displacement recorded in the models versus the imposed settlement deflection, $\delta/2L$.

The comparison shows to what extent arches having a longer span are more sensible to differential settlement with respect to arches having a smaller span and provides information on the level of damage that the structures may exhibit for different level of ground movements. The results collected have not a general validity and are applicable only to the structures analysed in the present work. Nevertheless, the aim is to show to what extent the multi-scale approach presented may be a valuable tool for the analysis of historical masonry structure and may provide direct and useful information for the designer. For instance, for a given design scenario, *i.e.* position and depth of the tube's gallery, it is possible to estimate the expected ground settlement and curvature at the base of the aqueduct by adopting the theory developed by Peck (1969). Then, the expected level of damage which the arches are supposed to undergo may be deduced by using Figure 5.21 and, accordingly, the level of safety of the design scenario may be established.

6. Conclusions

The present thesis deals with the mechanical behaviour of unreinforced masonry structures.

The first part of the work provides a contribution to the study of out-of-plane seismic behaviour of masonry walls by means of both experimental shake-table tests and a reliable modelling approach. An experimental campaign on a natural scale U-shaped assemblage, consisting of a façade and two transverse walls, has been carried out. A set of 34 shake-table tests is presented, in order to analyse the seismic behaviour of the façade, from the beginning of rocking up to overturning. The tests confirm the existence of a significant dynamic reserve of stability, which allows the wall to be set into motion without necessarily collapsing. Such reserve should not be neglected in assessment procedures, whenever it is necessary to limit either costs (large urban districts involved) or interventions (e.g., because the strengthening could imply cultural loss). The above considerations hold provided that the wall behaves monolithically, which is the case under consideration. When poor quality masonry is encountered and disaggregation occurs, the out-of-plane capacity of the wall is expected to strongly reduce.

A modelling approach, based on the Distinct Element Method, is developed for reproducing the non-linear dynamic behaviour of the wall. It takes into account the asymmetry of motion caused by the impact against the transverse walls, a smooth restoring moment–rotation relationship, and the effect of imperfections, such as tilted foundation or gap in existing cracks. A comparison with the presented experiments shows that contact points should be enough to match the push-over curve of a block on an elastic foundation, that the contact stiffness is about $1/5$ of the mortar elastic modulus, and that the damping ratio lies in the range $0.02 \tan \alpha - 0.10 \tan \alpha$, depending on the damage level. The methodology adopted is capable of reproducing the tests, in terms of both entire time history and maximum rotation, even if model parameters are roughly assumed.

Experimental and numerical data, generated through the established model, are used to check the current Italian seismic code assessment procedures. The comparison reveals a rather large scatter in code procedures, which is related to the simplifications in the two approaches. However, this scatter is accounted for by an adequate safety margin. As a matter of fact, the strength-based assessment

proves to be conservative in 99% of cases, while the displacement-based approach is conservative in 82% of cases. Eventually, code procedures may give controversial results when compared one against the other, and fail to capture significant features of the response. Therefore, dynamic models prove valuable both for validating code procedures, and for delivering more accurate physical representation of seismic behaviour of masonry walls.

The second part of the thesis gives a contribution to the development of simplified homogenization procedures for describing the behaviour of masonry structures both in the elastic and non linear range.

Within the elastic range, a novel approach is followed for the constitutive identification of elastic masonry, which applies rigorously the homogenization theory in one step considering three-dimensional effects, the actual thickness and the whole set of mortar joints. A simplified kinematics for the representative volume element of the material (RVE) is adopted: the hypothesis of piece-wise constant strain field makes it possible to handle the problem analytically and to derive the elasticity tensor of masonry as a function of mortar and brick geometrical and mechanical properties. Relevance is then given to the tensors of strain and stress localization which make it possible to derive the microscopic fields for a given macroscopic load.

The formulations found include, as particular limit cases, some of the models previously proposed in literature, *i.e.* in which masonry is regarded as a stratified material or in which joints are treated as interfaces.

The error introduced by the model compared to finite element analysis is particularly low both in terms of elastic modules and microscopic stresses fields, even when large differences between mortar and brick stiffness are considered, or when thick joints are taken into account. Furthermore, good agreement is found with experimental data in predicting the elastic modulus under vertical compression.

The proposed method is then applied to evaluate the limit elastic domain of masonry under in-plane loads. The results are in agreement with the experimental tests available in literature, Page (1985). The anisotropic behaviour induced by the internal microstructure of the material is well represented and direct information is given on the triggering failure mode related to different combinations of in-plane loads.

Within the non linear range a multi-scale methodology is set up for evaluating the response of in-plane loaded masonry. More precisely, a first order homogenization is performed where Cauchy continua are adopted for representing both the equivalent medium at the macroscopic scale and the

components at the microscopic scale. In order to reduce the complexity of the problem, a micromechanical model is adopted, where masonry is treated as an assembly of elastic blocks connected by elasto-plastic interfaces obeying to a Mohr-Coulomb criterion with non-associative flow rule. A simplified kinematics is thus introduced over the representative volume element of the material, which assumes an affine displacement for the block and makes it possible to express the localization problem, *i.e.* the problem that governs the transition from the macroscopic to the microscopic scales, in terms of a reduced number of unknowns. The solution of the latter problem is found efficiently and with low computational effort by resorting to an iterative Newton-Raphson scheme. Accordingly, the proposed algorithm provides for a prescribed macroscopic strain the co-respective macroscopic stress and the elasto-plastic tangent operator taking into account the non linearities that develop at the microscopic scale.

To test the capability of the proposed approach in solving the non linear localization problem, numerical analyses have been carried out on the RVE undergoing monotonically increasing macroscopic loads. The results show that the proposed scheme is able to reproduce the progressive development of plastic strain and the redistribution of internal stresses within the block and the interfaces for different types of load condition.

Finally, the multi-scale algorithm is implemented in the finite element code Abaqus and some applications have been discussed. In particular, the analysis of dry-stack masonry walls under gravity and horizontal accelerations has been presented. The results show a reasonable agreement with experimental tests from literature in terms of collapse load multiplier and mode of failure. The small discrepancy found may be related to size effects which are not accounted for in the model since a first order homogenization is adopted for deriving the response of the material or to second order effects, deriving from large displacements. Eventually, the proposed approach proves consistent with analytical formulations obtained for selected applications within the ambit of the yield design theory.

The results collected demonstrate the feasibility of the proposed multi-scale algorithm and its capability in reproducing the behaviour of dry-stack masonry structures. Being aware that the methodology discussed treats only some aspects of masonry behaviour which are mainly related with the friction that develops within the joints, it may be reasonable extended to the analysis of historical masonry too, provided that regular arrangement of the block, small thickness of the joints and poor quality mortar are encountered.

The proposed methodology is then adopted for evaluating the response under non-uniform ground settlements of masonry arcades which belong to the Felice aqueduct in Rome. The analyses provide a direct relation between the expected damage on the structure, which is measured in terms of opening and sliding of the joints, and the level of ground settlement. The results collected do not have a general validity since only few cases are discussed. Nevertheless, they suggest to what extent the proposed methodology proves a valuable tool for the analysis of historical construction in selected engineering applications.

Conversely, when dealing with modern masonry the proposed approach would manifest its main limits and an improvement would be necessary. Noteworthy, it is possible to include in a straightforward way more sophisticated constitutive relations that reproduce progressive cracking of the joints. Nevertheless, the representation of the joint as zero-thickness interfaces proves to be not satisfactory in reproducing the failure of masonry in compression and a micro model which accounts for the finite thickness of the joint would be necessary.

The future developments of the work are oriented towards these directions: starting from the algorithm here presented the aim is to improve it by including finite thickness of the joint, by referring to the micromechanical model presented in Chapter 4, and more refined constitutive relations for the components so as to obtain a computational tool for the analysis of historic and modern masonry structures which is reliable and low time consuming. In the meanwhile, proper measures to handle convergence difficulties and the well-known problems of mesh-dependency and localization of strain are evaluated among the different solution proposed in the literature, *i.e.* the use of finite element based on a mixed formulation, the use of a Cosserat identification at the macroscopic level, use of non-local integral model among others.

7. References

- ABK (1981). “*Methodology for mitigation of seismic hazards in existing unreinforced masonry buildings: wall testing, out of plane. Topical Report 04*”. Agbabian Associates, El Segundo.
- Addessi D., Sacco E., Paolone A. (2010). “Cosserat model for periodic masonry deduced by nonlinear homogenization”. *European Journal of Mechanics A/Solids*, **29**, pp. 724-737.
- Al Shawa O., Mauro A., de Felice G., Sorrentino L. (2011). “Prove su tavola vibrante su pareti singole e accostate a muri trasversali. Simulazioni numeriche preliminari”. In: *Proceeding of ANIDIS XIV conference, L’ingegneria Sismica in Italia*, Bari. (In Italian).
- Alpa G. and Monetto I. (1994). “Microstructural model for dry block masonry walls with in-plane loading”. *Journal of the Mechanics and Physics of Solids*, **42**, pp. 1159-1175.
- Andreas U. (1996). “Failure criteria for masonry panels under in-plane loading”. *Journal of Structural Engineering*, **112**, pp. 37-46.
- Anthoine A. (1995). “Derivation of the in-plane elastic characteristics of masonry through homogenization theory”, *International Journal of Solids and Structures*, **32**, pp. 137-163.
- Anthoine A., Magonette G., Magenes G. (1995). “Shear-compression testing and analysis of brick masonry walls”. *Proceedings of the eight North American Masonry Conference*, Austin, Texas, pp. 235-246.
- Anthoine A. (1997). “Homogenization of periodic masonry: plane stress, generalized plane strain or 3d modelling?”. *Communications in Numerical Methods in Engineering*, **13**, pp. 319-326.

- Atkinson R.H., Noland J.L., Abrams D.P. (1985). "A deformation failure theory for stack-bond brick masonry prism in compression". In: *Proceedings of the Seventh International Brick Masonry Conference*, Melbourne, Australia, **1**, pp. 577-592.
- Atkinson R.H., Amadei B.P., Saeb S., Sture S. (1989). "Response of masonry bed joint in direct shear". *Journal of Structural Division, ASCE*, **115**, pp. 2276-2296.
- Azevedo J., Sincraian G., Lemos J.V. (2000). "Seismic behaviour of blocky masonry structures". *Earthquake Spectra*, **16**, pp. 337-365.
- Badalà A. and Cuomo M. (1996). "Determinazione delle proprietà meccaniche della muratura come solido composito. Risultati sperimentali su muretti in scala 1:4 di quattro diverse tipologie". In: *Proceedings of La meccanica delle murature tra teoria e progetto*, Bologna, Italy, pp. 85-94.
- Bensoussan, A., Lions, J.L., Papanicolaou, G. (1978). "*Asymptotic Analysis for Periodic Structures*". North-Holland, Amsterdam, Netherlands.
- Berto L., Satta A., Scotta R., Vitaliani R. (2005). "Failure mechanism of masonry prism loaded in compression: computational aspects". *Material and Structures*, **38**, pp. 249-256.
- Binda L., Fontana A., Frigerio G. (1988). "Mechanical behaviour of brick masonries derived from unit and mortar characteristics". In: *Proceedings of the eight International Brick/Block masonry conference* Elsevier Applied Science Publisher LTD, Dublin, Ireland, pp. 205-216.
- Binda L., Fontana A., Anti L. (1991). "Load transfer in multiple leaf masonry walls". In: *Proceedings of the Ninth International Brick/Block Masonry Conference*, Berlin, Germany, pp. 1488-1497.
- Binda L., Tiraboschi C., Mirabella Roberti G., Baronio G., Cardani G. (1996a) "*Measuring masonry material properties: detailed results from an extensive experimental research, Part I: Tests on masonry components*". Report 5.1, Politecnico di Milano, Italy.

-
- Binda L., Tiraboschi C., Mirabella Roberti G., Baronio G., Cardani G. (1996b) “*Measuring masonry material properties: detailed results from an extensive experimental research, Part II: Tests on masonry specimens*”. Report 5.1, Politecnico di Milano, Italy.
- Binda L., Pina-Henriques J., Anzani A., Fontana A., Lourenço P.B. (2006). “A contribution for the understanding of load-transfer mechanisms in multi-leaf masonry walls: Testing and modelling”. *Engineering Structures*, **28**, pp. 1132-1148.
- Blasi C. and Spinelli P. (1986). “Un metodo di calcolo dinamico per sistemi formati da blocchi rigidi sovrapposti”. *Ingegneria sismica*, Anno III, **1**, pp. 12-21 (In Italian).
- Boroschek R. and Iruretagoyena A. (2006). “Controlled overturning of unanchored rigid bodies”. *Earthquake Engineering and Structural Dynamics*, **35**, pp. 695–711.
- Bosiljkov V., Page A.W., Bokan-bosiljkov V., Zarnic R. (2003). “Performance based studies of in-plane loaded unreinforced masonry walls”. *Masonry International*, **16**, pp. 39-50.
- Brasile S., Casciaro R., Formica G. (2007). “Multilevel approach for brick masonry walls – Part I: A numerical strategy for the nonlinear analysis”. *Computer Methods in Applied Mechanics and Engineering*, **196**, pp. 4934-4951.
- Brencich A. and Lagomarsino S. (1998). “A macroelement dynamic model for masonry shear walls”. In: *Computer Methods in Structural Masonry 4*. London, United Kingdom, pp. 67-75.
- Brencich A. and Gambarotta L. (2005). “Mechanical response of solid clay brickwork under eccentric loading. Part I: Unreinforced masonry”. *Materials and Structures*, **38**, pp. 257-266.
- Brencich A., de Felice G. (2009). “Brickwork under eccentric compression: experimental results and macroscopic models”. *Construction and Building Materials*, **23**, pp. 1935-1946.

- Briccoli Bati S., Ranocchiali G., Rovero L. (1999). "A micromechanical model for linear homogenization of brick masonry". *Materials and Structures*, **32**, pp. 22-30.
- Brooks J.J. (1990). "Composite modelling of masonry deformation" *Materials and Structures*, **23**, pp. 241-251.
- Brooks J.J. and Abu Baker B.H. (1998). "The modulus of elasticity of masonry". *Masonry International*, **12**, pp. 58-63.
- Calvi G.M., Kingsley G.R., Magenes G. (1996). "Testing masonry structures for seismic assessment". *Earthquake Spectra*, **12**, pp. 145-162.
- Campanella, G. 1928. "*Trattato generale teorico pratico dell'arte dell'ingegnere civile, industriale ed architetto: ponti in muratura*". Vallardi (Eds.), Milan, Italy, (In Italian).
- Carbone V.I. and Codegone M. (2005). "Homogenization process of stratified masonry". *Mathematical and Computational Modelling*, **42**, pp. 375-380.
- Cavalieri, N. (1845). "*Istruzioni di Architettura, Statica e Idraulica*". Tipografia Cardinali e Frulli, Bologna, Italy, (In Italian).
- Cecchi A., Sab K. (2002a). "A multi-parameter homogenization study for modeling elastic masonry". *European Journal of Mechanics A/Solid*, **21**, pp. 249-268.
- Cecchi A., Sab K. (2002b). "Out-of-plane model for heterogeneous periodic materials: the case of masonry." *European Journal of Mechanics A/Solid*, **21**, pp. 715-746.
- Cecchi A., Sab K. (2004). "A comparison between a 3D discrete model and two homogenised plate models for periodic elastic brickwork." *International Journal of Solids and Structures*, **44**, pp. 6055-6079.
- Cecchi A., Sab K. (2007). "A homogenized Reissner-Mindlin model for orthotropic periodic plates: application to brickwork panels." *International Journal of Solids and Structures*, **41**, pp. 2259-2276.

-
- Cecchi A., Milani G., Tralli A. (2007). "A Reissner-Mindlin limit analysis model for out-of-plane loaded running bond masonry walls". *International Journal of Solids and Structures*, **44**, pp. 1438-1460.
- Cecchi A. and Milani G. (2008). "A kinematic FE limit analysis model for thick English bond masonry walls". *International Journal of Solids and Structures*, **45**, pp. 1302-1331.
- Ceradini V. (1992). "*Modellazione e sperimentazione per lo studio della struttura muraria storica*", PhD thesis, Faculty of Architecture, University "La Sapienza", Rome.
- Chaimoon K. and Attart M. M. (2007). "Modelling of unreinforced masonry walls under shear and compression". *Engineering Structures*, **29**, pp. 2056-2068.
- CSLLP, Consiglio Superiore dei Lavori Pubblici (2009). Circolare 02 febbraio 2009 n. 617 Istruzioni per l'applicazione delle "Nuove norme tecniche per le costruzioni" di cui al DM 14 gennaio 2008. *Gazzetta Ufficiale della Repubblica Italiana n. 47, Supplemento Ordinario n. 27, § C8.A.4*. Roma, (In Italian).
- Curioni, G. (1872). "*L'arte di fabbricare ossia corso completo di istituzioni teorico-pratiche per gl'ingegneri, per gli architetti, pei periti in costruzione e pei periti misuratori*". Negro, A.F (Eds.), Turin, Italy, (In Italian).
- Cundall, P.A. (1971). "Computer model for simulating progressive large scale movements in blocky rock systems". In: *Proc. of the Symposium of International Society of Rock Mechanics*, **1**, Nancy, France, Paper No. II-8.
- De Buhan P. (1986). "Approche fondamentale du calcul a la rupture des ouvrages en sols renforcés". Thèse d'Etat, Université de Paris – VI.
- De Buhan P. and de Felice G. (1997). "A homogenization approach to the ultimate strength of masonry". *Journal of the Mechanics and Physics of Solids*, **45**, pp. 1085-1104.

- de Felice G. (1995). "Metodi di omogeneizzazione per sistemi regolari di corpi rigidi". In: *Proceeding of the XII AIMETA congress*, University of Naples, Italy, pp. 453-479.
- de Felice G. (2001). "Overall elastic properties of brickwork via homogenization". In: *Proceedings of the International. Conference on Structural Engineering, Mechanics and Computation*, **1**, Elsevier, Amsterdam, Netherlands, pp. 411-418.
- de Felice G., Giannini R. (2001). "Out-of-plane seismic resistance of masonry walls". *Journal of Earthquake Engineering*, **5**, pp. 253-271.
- de Felice G., Amorosi A., Malena M. (2010a). "Elasto-plastic analysis of block structures through a homogenization method". *International Journal For Numerical and Analytical Methods in Geomechanics*, **34**, pp. 221-247.
- de Felice G. and De Santis S. (2010b). "Experimental and numerical response of arch bridge historic masonry under eccentric loading". *International Journal of Architectural Heritage*, **4**, pp. 115-137.
- de Felice G. (2011). "Out-of-plane Seismic Capacity of Masonry Depending on Wall Section Morphology". *International Journal of Architectural Heritage*, **5**, pp. 466-482.
- Dhanasekar M., Page A.W., Kleeman P.W.(1982). "The elastic properties of brick masonry", *International Journal of Masonry Construction*, **2**, pp. 155-160.
- Dhanasekar M., Page A.W., Kleeman P.W.(1985). "The failure of brick masonry under biaxial stresses", *Proceedings of the Institution of Civil Engineers, Part 2*, **79**, pp. 295-313.
- Doherty KT, Griffith MC, Lam NTK, Wilson JL (2002). Displacement-based seismic analysis for out-of-plane bending of unreinforced masonry walls. *Earthquake Engineering and Structural Dynamics*, **31**, pp. 833-850.
- Donghi, D. (1935). "*Manuale dell'architetto*". Unione Tipografico-Editrice Torinese (Eds.), Turin, Italy, (In Italian).

-
- Dvorak G.J. (1992). "Transformation field analysis of inelastic composite materials". In: *Proceedings, Mathematical and Physical Sciences*, **437**, pp. 331-327.
- ElGawady M.A., Ma Q., Butterworth J.W., Ingham J. (2011). "Effects of interface material on the performance of free rocking blocks", *Earthquake Engineering and Structural Dynamics*, **40**, pp. 375–392.
- Forth J.P. and Brooks, J.J. (1995). "Influence of mortar type on the long term deformation of single leaf clay brick masonry". In: *Proceedings of the fourth International Masonry Conference*, **7**, British Masonry Society, London, United Kingdom, pp. 157-161.
- Francis A.J., Horman C.B., Jerrems L.E. (1971). "The effect of joint thickness and other factor on the compressive strength of brickwork" In: *Proceedings of the Second International Brick Masonry Conference*, Stoke-on-Trent, United Kingdom, pp. 31-37.
- Gabba, A. and Caveglia C. (1876). "*Corso di costruzioni civili e militari, Vol. 2*". Stamperia dell'unione tipografico-editrice (Eds), Turin, Italy, (In Italian).
- Gambarotta L. and Lagomarsino S. (1997a). "Damage models for the seismic response of brick masonry shear walls. Part I: the mortar joint model and its applications". *Earthquake Engineering and Structural Dynamics*, **26**, pp. 423-439.
- Gambarotta L. Lagomarsino S. (1997b). "Damage models for the seismic response of brick masonry shear walls, Part II: the continuum model and its applications". *Earthquake Engineering and Structural Dynamics*, **26**, pp. 441-462.
- Ganz H.R. and Thürlimann B. (1982). "*Tests on the biaxial strength of masonry*". Report No. 7502-3, Institute of Structural Engineering, ETH Zurich, Switzerland, (in German).
- Ganz H.R. (1989). "Failure criteria for masonry". In: *Proceedings of the fifth Canadian Masonry Symposium*, **1**, University of British Columbia, Vancouver, Canada, pp. 65-77.

- Geers M.G.D., Kouznetsova V.G., Brekelmans W.A.M. (2010). "Multi-scale computational homogenization: Trends and challenges". *Journal of Computational and Applied Mathematics*, **234**, pp. 2175-2182.
- Giordano A., Mele E., De Luca A. (2002). "Modelling of historical masonry structures: comparison of different approaches through a case study". *Engineering Structures*, **24**, pp. 1057-1069.
- Griffith M.C., Lam N.T.K., Wilson J.L., Doherty K. (2004). "Experimental investigation of URM walls in flexure". *Journal of Structural Engineering ASCE*, **130**, pp. 423-432.
- Guggisberg R. and Thürlimann B. (1987). "*Experimental determination of masonry strength parameters*". Report No. 7502-5, Institute of Structural Engineering, ETH Zurich, Switzerland, (in German).
- Gumaste K.S., Nanjunda Rao K.S., Venkatarama Reddy B.V., Jagadish K.S., (2007). "Strength and elasticity of brick masonry prisms and wallets under compression". *Materials and Structures*, **40**, pp. 241-253.
- Haller P., (1958). "Die technische eigenschaften von backstein" (The strength of clay and calcium silicate brick masonry subjected to shear). *Schweizerische bauzeitung*, **78**, pp. 411-419, (dutch translation 1967).
- Harvey R.J. (1996). "*Creep of concrete masonry*", Ph.D. Thesis, University of Wales, Cardiff School of Engineering, United Kingdom.
- Hilsdorf H.K. (1969). "Investigation into the failure mechanism of brick masonry loaded in axial compression". In: Johnson, F.B. (Eds.), *Designing, engineering & construction with masonry products*, Gulf publishing, Houston, Texas, pp. 34-41.
- Housner G.W. (1963). "The behavior of inverted pendulum structures during earthquakes". *Bulletin of the Seismological Society of America*, **53**, pp. 403-417.
- Itasca consulting group Inc. (2003). "*UDEC-Universal distinct element code, version 3.0 – User's manual*". Minneapolis, Minnesota.

-
- Jukes P., Riddington J.R. (1997). "A review of masonry joint shear strength test methods". *Masonry International*, **11**, pp. 37-41.
- Kaushik H.B., Rai D.C., Jain S.K. (2007). "Stress-strain characteristics of clay brick masonry under uniaxial compression", *Journal of Materials in Civil Engineering*, **19**, pp. 728-739.
- Kawa M., Pietruszczak S., Shieh-Beygi B. (2008). "Limit states for brick masonry based on homogenization approach". *International Journal of Solids and Structures*, **45**, pp. 998-1016.
- Khoo C.L. and Hendry A.W. (1973). "Strength tests on brick and mortar under complex stresses for the development of a failure criterion for brickwork in compression". *Proceedings of the British Ceramic Society*, **21**, pp. 51-66.
- Lam N.T.K., Wilson J.L., Hutchinson G.L. (1995). "The Seismic Resistance of Unreinforced Masonry Cantilever Walls in Low Seismicity Areas". *Bulletin of the New Zealand National Society for Earthquake Engineering*, **28**, pp. 179-195.
- Lenczner D. (1978). "The effect of strength and geometry on the elastic and creep properties of masonry members". In: *Proceedings of the first North American Masonry Conference*, Boulder, Colorado, **23**, pp. 1-15.
- Liberatore D., Spera G. (2001). "Response of slender blocks subjected to seismic motion of the base: description of the experimental investigation". In: *Proceedings fifth International Symposium on Computer Methods in Structural Masonry, Rome*, pp. 117-124.
- Litweka A. and Szojda L. (2006). "Damage, plasticity and failure of ceramics and cementitious composite subjected to multi-axial state of stress". *International Journal of Plasticity*, **22**, pp. 2048-2065.
- Lofti H.R., Shing P.B. (1991). "An appraisal of smeared crack models for masonry shear wall analysis". *Computers and Structures*, **41**, pp.413-425.

- Lofti H.R., Shing P.B. (1994). "An interface model applied to fracture of masonry structures". *Journal of Structural Engineering*. (ASCE), **120**, pp. 63-80.
- Lopez J., Oller S., Onate E., Lubliner J. (1999). "A homogeneous constitutive model for masonry". *International Journal for Numerical Methods in Engineering*, **46**, pp. 1651-1671.
- Lourenço P.B., Rots J.G. (1997a). "Multisurface interface model for the analysis of masonry structures". *Journal of Engineering Mechanics*, ASCE, **123**, pp. 660-668.
- Lourenço P.B., Rots J.G. (1997b). "On the use of homogenisation techniques for analysis of masonry structures". *Masonry International*, **11**, pp. 26-32.
- Lourenço P.B., Rots J.G., Blaauwendraad J. (1998). "Continuum model for masonry: parameter estimation and validation". *Journal of Structural Engineering*, **124**, pp. 642-652.
- Lourenço P.B. (2000). "Anisotropic softening model for masonry plates and shells". *Journal of Structural Engineering ASCE*, **129**, pp. 1008-1016.
- Lourenço, P.B. and Pina-Henriques J. (2006). "Validation of analytical and continuum numerical methods for estimating the compressive strength of masonry". *Computer and Structures*, **84**, pp. 1977-1989.
- Luciano R. and Sacco E. (1997). "Homogenization technique and damage model for old masonry material". *International Journal of Solids and Structures*, **34**, pp. 3191-3208.
- Lurati F., Graf, H., Thürlimann B. (1990). "*Experimental determination of the strength parameters of concrete masonry*". Report No. 8401-2, Institute of Structural Engineering, ETH Zurich, Switzerland, (in German).
- Ma G. Hao H., Lu Y. (2001). "Homogenization of masonry using numerical simulations". *Journal of Engineering Mechanics*, **127**, pp. 421-431.

-
- Magenes G. and Calvi G.M. (1997). "In plane seismic response of brick masonry walls". *Earthquake Engineering and Structural Dynamics*, **26**, pp. 1091-1112.
- Magenes G. and Della Fontana A. (1998). "Simplified Non-linear Seismic Analysis of Masonry Buildings". In: *Proceedings of the British Masonry Society*, **8**, pp. 190-195.
- Maier G., Papa E., Nappi A. (1991). "On damage and failure of brick masonry". In: J. Donea, P.M. Jones (Eds.), *Experimental and numerical methods in earthquake engineering*, Paris, pp. 223-245.
- Marfia S. and Sacco E. (2011). "Multiscale damage contact-friction model for periodic masonry walls". *Computer Methods in Applied Mechanics and Engineering*, **205**, pp. 189-203.
- Masiani R., Rizzi R., Trovalusci P. (1995). "Masonry as structured continuum". *Meccanica*, **30**, pp. 673-683.
- Masiani R. and Trovalusci P. (1996). "Cauchy and Cosserat materials as continuum models of brick masonry". *Meccanica*, **31**, pp. 421-432.
- Massart T.J., Peerlings R.H.J., Geers M.G.D. (2004). "Mesoscopic modelling of failure and damage-induced anisotropy in brick masonry". *European Journal of Mechanics A/Solids*, **23**, pp. 719-735.
- Massart T.J., Peerlings R.H.J., Geers M.G.D., Gottcheiner S. (2005). "Mesoscopic modeling of failure in brick masonry accounting for three-dimensional effects", *Engineering Fracture Mechanics*, **72**, pp. 1238-1253.
- Massart, T. J., Peerlings, R. H. J., Geers, M. G. D. (2007). "An enhanced multi-scale approach for masonry wall computations with localization of damage". *International Journal for Numerical Methods in Engineering*, **69**, pp. 1022-1059.
- Mauro A. (2008). "*Long term effects of masonry walls*". Msc thesis, University of Roma Tre, Italy.

- McNary W.S. and Abrams D.P. (1985). "Mechanics of Masonry in Compression". In: *Proceedings of the American Society of Civil Engineers, Journal of Structural Engineering*, **111**, pp. 857-870.
- Meisl C.S., Elwood K.J., Ventura C.E. (2007). "Shake table tests on the out-of-plane response of unreinforced masonry walls. *Canadian Journal of Civil Engineering*, **34**, pp. 1381-1392.
- Mercatoris B.C.N., Bouillard, P., Massart, T. J. (2009). "Multi-scale detection of failure in planar masonry thin shells using computational homogenisation". *Engineering Fracture Mechanics*, **76**, pp. 479–499.
- Mercatoris B.C.N. and Massart, T. J. (2010). "A coupled two-scale computational scheme for the failure of periodic quasi-brittle thin planar shell and its application to masonry". *International Journal for Numerical Methods in Engineering*, DOI 10.1002/nme.3018.
- Milani G., Lourenço P. B., Tralli, A. (2006a). Homogenised limit analysis of masonry walls, Part I: Failure surfaces. *Computers & Structures*, **84**, pp. 166–180.
- Milani G., Lourenço P. B., Tralli, A. (2006b). "Homogenised limit analysis of masonry walls, Part II: Structural examples". *Computers and Structures*, **84**, pp. 181–195.
- Milani G., Lourenço P. B., Tralli, A. (2006c). "Homogenization approach for the limit analysis of out-of-plane loaded masonry walls". *Journal of Structural Engineering, ASCE*, **132**, pp. 1650–1663.
- Milani E., Milani G., Tralli, A. (2008). "Limit analysis of masonry vaults by means of curved shell finite elements and homogenization". *International Journal of Solids and Structures*, **45**, pp. 5258–5288.
- Mistler M., Anthoine A., Butenweg C. (2007). "In plane and out-of-plane homogenization of masonry". *Computer and Structures*, **85**, pp. 1321-1330.

-
- Naraine K. and Sinha S. (1992). "Stress-strain curves for brick masonry in biaxial compression". *Journal of structural engineering*, ASCE, **118**, pp. 1451-1461.
- Oliveira D.V., Lourenço P.B., Roca P. (2006). "Cyclic Behaviour of stone and brick masonry under uniaxial compressive loading". *Materials and Structures*, **39**, pp 247-257.
- Page, A.W. (1978). "Finite element model for masonry". *Journal of the Structural Division, ASCE*, **104** , pp. 1267-1285.
- Page A.W., Samarasinghe W., Hendry A.W. (1982). "The In-Plane Failure of Masory – A Review". *Proceedings of the British Ceramic Society*, **30**, pp. 90-99.
- Page A.W. (1981). "The biaxial compressive strength of brick masonry". In: *Proceeding of Institution of Civil Engineers Part 2*, **71**, pp. 893-906.
- Page A.W. (1983). "The strength of brick masonry under biaxial compression-tension", *International Journal of Masonry Construction*, **3**, pp. 26-31.
- Pande G.N., Liang J.X., Middleton J. (1989). "Equivalent elastic moduli for brick masonry". *Computers and Geotechnics* . **8**, pp. 243-265.
- Papantonopoulos C., Psycharis I.N., Papastamatiou D.Y., Lemos J.V., Mouzakis H.P. (2002). "Numerical prediction of the earthquake response of classical columns using the distinct element method", *Earthquake Engineering and Structural Dynamics*, **31**, pp. 1699-1717.
- Peck R.B. (1969). "Deep excavation and tunnelling in soft ground". In: *Proceedings of the seventh International Conference of Soil Mechanics and Foundation Engineering*, pp. 225-281.
- Peña F., Prieto F., Lourenço P.B., Campos-Costa A., Lemos J.V. (2007). "On the dynamics of rocking motion of single rigid-block structures". *Earthquake Engineering and Structural Dynamics*, **36**, pp. 2383-2399.

- Pietruszczak S. and Niu X. (1992). "A mathematical description of macroscopic behaviour of brick masonry". *International Journal of Solids and Structures*, **29**, pp. 531-546.
- Plowman J.M. (1965). "The modulus of elasticity of brickwork". In: *Proceeding of the British Ceramic Society*, **4**, pp. 37-44.
- Priestley M.J.N. and Elder D.M. (1983). "Stress-strain cruves for unconfined and confined concrete masonry". *ACI Journal*, **80**, pp. 192-201.
- Psycharis I.N., Jennings P.C. (1983). "Rocking response of rigid blocks allowed to uplift". *Earthquake Engineering and Structural Dynamics*, **11**, pp. 57-56.
- RILEM (1994). "*Technical recommendations for the testing and use of construction materials: LUMAI-Compressive strength of masonry units*". Chpman & Hall (Eds), United Kingdom.
- Reyes E., Cosati M.J., Galvez J.C. (2008). "Cohesive crack model for mixed made fracture of brick masonry". *International Journal of Fracture*, **151**, pp. 29-55.
- Riks E. (1979). "An incremental approach to the solution of snapping and buckling problems". *International Journal of Solids and Structures*, **15**, pp- 529-551.
- Rots J.G. (1991). "Numerical simulation of cracking in structural masonry". *HERON*, **36-2**, pp. 49-63.
- Sacco E. (2009). "A nonlinear homogenization procedure for periodic masonry". *European Journal of Mechanics A/Solids*, **28**, pp. 209-222.
- Sahlin S. (1971). "*Structural Masonry*", Prentice-Hall Inc., New Jersey.
- Salerno G. and Uva G. (2002). "A two-scale algorithm for the non-linear analysis of damaged masonry brickwork" In: *Proceeding of the The Fifth World Congress on Computational Mechanics*, Vienna, Austria.

-
- Salerno G. and de Felice G. (2009). "Continuum modelling of periodic brickwork". *International Journal of Solids and Structures*, **46**, pp. 1251-1267.
- Salomon M.D.G. (1968). "Elastic moduli of a stratified rock mass". *International Journal of Rock Mechanics and Mining. Science*, **5**, pp. 519-527.
- Samarasinghe W. and Hendry A.W. (1980). "The strength of brickwork under biaxial tensile and compressive stress". In: *Proceedings of the Seventh International Symposium in Load Bearing Brickwork*, London, United Kingdom, pp 129-139.
- Sanchez-Palencia, E. (1980). "*Non Homogeneous Media and Vibration Theory*". Springer, Berlin, Germany.
- Sayed-Ahmed E.Y. and Shrive N.G. (1996). "Nonlinear finite-element model for Hollow Masonry". *Journal of Structural Engineering, ASCE*, **122**, pp. 683-670.
- Schubert P. (1988). "The influence of mortar on the strength of masonry". in: *Proceedings of the eight International. Brick and Block Masonry Conference*, London, United Kingdom, pp. 162-174.
- Sebastianelli M. (2011). "*Cedimenti indotti da scavi in galleria ed effetti sulle strutture murarie sovrastanti*". Master thesis, University Roma Tre, Rome.
- Shrive N.G. and England G.L. (1981). "Elastic, creep and shrinkage behaviour of masonry". *International Journal of Masonry Constructions*, **1**, pp. 103-109.
- Simsir C.C., Aschheim M.A., Abrams D.P. (2004). "Out-of-Plane Dynamic Response of Unreinforced Masonry Bearing Walls Attached to Flexible Diaphragms", *13th World Conference on Earthquake Engineering*, Vancouver, B.C., Paper No. 2045.
- Simulia (2011). *Abaqus Standar Reference Manuals*, Versioin 6.11.2, Providence, RI, USA.

- Sorrentino L., Masiani R., Decanini L.D. (2006). "Overturning of rocking rigid bodies under transient ground motions". *Structural Engineering and Mechanics*, **22**, pp. 293-310.
- Sorrentino L, Kunnath S, Monti G, Scalora G (2008). Seismically induced one-sided rocking response of unreinforced masonry façades. *Engineering Structures*, **30**, pp. 2140-2153.
- Sorrentino L., Al Shawa O., Decanini L.D. (2012). "The relevance of energy damping in unreinforced masonry rocking mechanisms. Experimental and analytic investigations". Submitted to: *Bulletin of Earthquake Engineering*.
- Suquet P.M. (1987). "Elements of homogenization for inelastic solid mechanics". In: *Homogenization techniques for composite media*, Sanchez-Palencia E., Zaoui A. (Eds.), Springer, Berlin, pp. 193-279.
- Trovalusci P. and Masiani R. (2003). "Non linear micropolar and classical continua for anisotropic discontinuous materials". *International Journal of Solids and Structures*, **40**, pp. 1281-1297.
- UNI 8942-3:1986 (1986). "Clay brick and blocks. Tests methods", Ente nazionale italiano di unificazione, (In Italian).
- Uva G. and Salerno G. (2006). "Towards a multiscale analysis of periodic masonry brickwork: A FEM algorithm with damage and friction". *International Journal of Solids and Structures*, **43**, pp. 3739-3769.
- Valluzzi M.R., Binda L., Modena C. (2002). "Experimental and analytical studies for the choice of repair techniques applied to historic buildings". *Materials and Structures*, **35**, pp. 285-292.
- Van Der Pluijm J. (1992). "Material properties of masonry and its components under tension and shear". In: *Proceedings of the sixth Canadian Masonry Symposium*, Saskatchewan, Canada, pp. 675-686.
- Van Der Pluijm J. (1993). "Shear behaviour of bed joints". In: *Proceedings of the Sixth North American Masonry Conference*, Philadelphia, Pennsylvania, pp. 125-136.

-
- Vasconcelos G. and Lourenço P.B. (2009). "In-Plane experimental behaviour of stone masonry walls under cyclic loading". *Journal of Structural Engineering ASCE*, **135**, pp.1269-1277.
- Weinan E., Bjorn E., Xiantao L., Weiqing R., Vanden-Eijnden E. (2007). "Heterogeneous multiscale methods: A Review". *Communications in Computational Physics*, **2**, pp. 367-450.
- Yurdas I., Nicolas B., Skoczylas F. (2004). "Triaxial mechanical behaviour of mortar: Effect of drying". *Cement and Concrete Research*, **34**, pp. 1131-1143.
- Zucchini A. and Lourenço P.B. (2002) "A micro-mechanical model for the homogenization of masonry". *International Journal of Solids and Structures*, **39**, pp. 3233-3255.
- Zucchini A. and Lourenço P.B. (2004). "A Coupled homogenization-damage model for masonry cracking". *Computers and Structures*, **82**, pp. 917-929.
- Zucchini A. and Lourenço P.B. (2007). "Mechanics of masonry in compression: Results from an homogenization approach". *Computers and Structures*, **85**, pp. 193-204.
- Zucchini A. and Lourenço P.B. (2009). "A micro-mechanical homogenisation model for masonry: Application to shear walls". *International Journal of Solids and Structures*, **46**, pp. 871-886.